Title

Magnesium Gallium Oxide Thin Film Growth, Characterizations and Photoluminescence Studies

Author

Yang, Tianchen

Publication Date

2024

UNIVERSITY OF CALIFORNIA
RIVERSIDE

Magnesium Gallium Oxide Thin Film Growth, Characterizations and Photoluminescence Studies

A Dissertation submitted in partial satisfaction
of the requirements for the degree of

Doctor of Philosophy

in

Electrical Engineering

by

Tianchen Yang

September 2024

Dissertation Committee:
- Dr. Jianlin Liu, Chairperson
- Dr. Ming Liu
- Dr. Peng Wei

The Dissertation of Tianchen Yang is approved:

Committee Chairperson

University of California, Riverside

ACKNOWLEDGEMENTS

I am deeply grateful to my advisor, Prof. Jianlin Liu, for his invaluable guidance and support throughout my research journey. As a distinguished researcher, an encouraging mentor, and a true friend, he has instilled in me a dedication to rigor, diligence, and the pursuit of knowledge that has been essential to my work. This dissertation simply could not have been accomplished without his unwavering support. I would also like to extend my heartfelt thanks to the members of my dissertation defense committee, Prof. Ming Liu and Prof. Peng Wei, for their thoughtful feedback and helpful suggestions.

I am immensely thankful for the lifelong friendships formed with exceptional lab mates: Dr. Yanwei He, Dr. Long Xu, Dr. Caixia Xu, Dr. Hao Tian, Dr. Dong Yan, Dr. Qiyin Lin, Miss. Zhenjun Cui, Mr. Ivan Chiang, Mr. Chengyun Shou, Mr. Jason Tran, Mr. Abdullah Almujtabi, Mr. Quazi Sanjid Mahmud, and Mr. Edward Zhu. Additionally, I count myself extraordinarily fortunate to have the robust support network of my friends: Miss. Lu Jin, Mr. Junze Liu, Mr. Luyang Yu, Mr. Hang Yang, Mr. Runyi Sun, Mr. Hongzheng Tian, Miss. Xuanyu Fan, Miss. Xinping Shi, Dr. Liang Wu and Dr. Kunyao Jiang.

Finally, my deepest gratitude goes to my parents, whose unconditional love and support have been the bedrock of my strength and motivation. I am incredibly fortunate to have the freedom to explore all of life's possibilities with the knowledge that they will always stand behind me. Their embodiment of diligence and perseverance has profoundly influenced me, and I am committed to utilizing these virtues to improve my life and contribute positively to the world.

I dedicate my dissertation work to
my parents (杨正泰 and 戚艳丽)

ABSTRACT OF THE DISSERTATION

Magnesium Gallium Oxide Thin Film Growth, Characterizations and Photoluminescence Studies

by

Tianchen Yang

Doctor of Philosophy, Graduate Program in Electrical Engineering
University of California, Riverside, September 2024
Dr. Jianlin Liu, Chairperson

Ultrawide bandgap (UWBG) semiconductors have been widely used in power electronics and deep ultraviolet (UV) electronics. However, as a viable and very promising candidate, magnesium gallium oxide (MgGaO) thin film and its properties have not been studied systematically yet. In this thesis, we focused on MgGaO film epitaxial growth by molecular beam epitaxy (MBE), phase transition, optical transitions and UV photodetector applications.

In the first project, i.e., Chapter 2, we reported the growth of β-phase MgGaO ternary alloy thin films. Deep-ultraviolet *β*-MgGaO metal-semiconductor-metal photodetectors with interdigital Pt/Au metal contacts were fabricated. By varying the Mg atomic percent, bandgap of films was engineered from 5.03 to 5.22 eV, and transmittance of all films are ~90% in visible spectral range, and the MSM photodetectors show very good responsivity and current-time characteristics.

In the second project, i.e., Chapter 3, we presented a study of MgGaO thin film phase transition from β phase in Ga-rich materials, to β and rocksalt mixture phase in high-Ga

high-Mg alloys, and to pure rocksalt phase in Mg-rich alloys. 20 MgGaO samples with Mg atomic percentages from 0 to 100% were grown resulting in bandgap tuning from 5.03 to 5.89 eV, and all samples have transmittance over ~90% in the visible spectral range. How lattice parameters change with the increase of Mg at.%, and the epitaxy relationship between MgGaO films and c-sapphire substrates were revealed.

In the third project, i.e., Chapter 4, we reported an important inverse spinel structure in MgGaO family, namely $MgGa_2O_4$. Bandgap of $MgGa_2O_4$ spinel films is determined to be around 5.4~5.5 eV, and all samples have the transmittance over 90% in the visible spectral range. X-ray diffraction patterns confirmed that the spinel films were grown highly along <111> oriented. Thickness dependent film growth was performed to confirm the single crystal film achievement. The room temperature, power and temperature dependent photoluminescence (PL) studies were investigated.

In the last project, i.e., Chapter 5, we reported a refined MgGaO thin film phase transition from beta to spinel phase with varying Mg atomic percentages ranging from 0 to 15.26%. Structural analysis via X-ray diffraction confirms these transitions and identifies corresponding changes in lattice parameters. Comprehensive PL studies, encompassing room temperature measurements as well as power and temperature-dependent analyses, have revealed distinct emission spectra and mechanisms intrinsic to β-MgGaO and spinel $MgGa_2O_4$. These investigations have elucidated defect energy levels associated with various entities such as self-trapped holes (STH), deep donors from oxygen vacancies, deep acceptors involving Mg on Ga sites, and acceptor complexes formed with Ga and O, which are pivotal for advancing optoelectronic applications of these materials.

Table of Contents

List of Figures

List of Tables

Previously Published Material Acknowledgment:

1. The results in Chapter 2 were published in:
   Yang, Tianchen, Chengyun Shou, Long Xu, Jason Tran, Yanwei He, Yuan Li, Peng Wei, and Jianlin Liu. "Metal–Semiconductor–Metal Photodetectors Based on β-MgGaO Thin Films." ACS Applied Electronic Materials 5, no. 4 (2023): 2122-2130. https://doi.org/10.1021/acsaelm.3c00035.

2. The results in Chapter 3 were published in:
   Yang, Tianchen, Chengyun Shou, Abdullah Almujtabi, Jason Tran, Qiyin Lin, Yuan Li, Quazi Sanjid Mahmud, Peng Wei, and Jianlin Liu. "Investigation of Phase Transition and Ultrawide Band Gap Engineering in MgGaO Semiconductor Thin Films." ACS Applied Optical Materials 1, no. 10 (2023): 1670-1678. https://doi.org/10.1021/acsaom.3c00237.

3. The results in Chapter 4 were published in:
   Yang, Tianchen, Chengyun Shou, Jason Tran, Abdullah Almujtabi, Quazi Sanjid Mahmud, Edward Zhu, Yuan Li, Peng Wei, and Jianlin Liu. "Photoluminescence study of $MgGa_2O_4$ spinel oxide films grown by molecular beam epitaxy." *Applied Physics Letters* 125, no. 7 (2024). https://doi.org/10.1063/5.0218242.

4. The results in Chapter 5 were published in:
   Yang, Tianchen, Chengyun Shou, Abdullah Almujtabi, Quazi Sanjid Mahmud, Edward Zhu, Yuan Li, and Jianlin Liu. " Beta to spinel phase transition of magnesium gallium oxide thin films and their photoluminescence properties." ACS Applied Electronic Materials (2024). https://doi.org/10.1021/acsaelm.4c01079.

Chapter 1: Introduction

1.1 Beta phase Gallium Oxide (β-Ga_2O_3)

In the mid-20th century, wide bandgap materials such as SiC, GaN, and ZnO significantly advanced electronic and optoelectronic device development,[1,2] particularly notable for nitrides. Recently, substantial research focus has shifted to ultrawide bandgap (UWBG) semiconductors with bandgaps exceeding 4 eV, such as AlN, diamond, and β-Ga_2O_3.[2] Among these, monoclinic beta phase gallium oxide (β-Ga_2O_3) stands out as highly stable under standard temperature and pressure conditions. It is increasingly recognized for its potential across various applications including power electronics, solar-blind UV photodetectors, gas sensors, solar cells, and transparent conductive films for electrodes in diverse optoelectronic devices. This material offers capabilities that surpass current technologies due to its large bandgap and exceptional electrical and optical properties. [3,4]

The crystal structure of β-Ga_2O_3 is monoclinic with a base-centered lattice and belongs to space group C2/m.[3,5,6] The unit cell contains 20 atoms comprising two distinct Ga^{3+} and three distinct O^{2-} ions. In this relatively low symmetry configuration, Ga_I^{3+} is tetrahedrally coordinated, surrounded by one threefold O_I, two threefold O_{II}, and one fourfold O_{III} environments. Ga_{II}^{3+}, on the other hand, exhibits octahedral coordination with two threefold O_I, one threefold O_{II}, and three fourfold O_{III} surroundings. The unit cell is characterized by four lattice parameters: a, b, c, and β (the angle between the a and c axes), with dimensions $a = 12.23 \pm 0.02$ Å, $b = 3.04 \pm 0.01$ Å, $c = 5.80 \pm 0.01$ Å, and $\beta = 103.7 \pm 0.3°$. The electronic band structure of β-Ga_2O_3 reveals distinct characteristics: the conduction band (CB) is primarily shaped by hybridized Ga-s and O-p states, featuring a distinct local minimum at the Γ point and significant dispersion, resulting in a relatively low effective electron mass and high electron mobility.[3,4] Meanwhile, the valence band (VB) consists of three sub-bands. The upper sub-band is predominantly composed of O 2p states, spanning approximately 7.8 eV in width. The middle sub-band primarily derives from Ga 3d states, positioned about 10.5 eV below the valence band maximum (VBM). The lowest sub-band includes contributions from O 2s and Ga 3d states, located approximately 14.8 eV below the VBM.[7] The O 2p states contribute to a flat top of the valence band, resulting in minimal dispersion and consequently a high effective hole mass, limiting hole mobility and rendering practical p-type conductivity impractical.[3,4] The VBM exhibits local maxima at both Γ and M points in the Brillouin zone (BZ). β-Ga_2O_3 is categorized as a direct semiconductor, with a direct bandgap of 4.87 eV at Γ–Γ and a slightly smaller indirect bandgap of 4.83 eV at M–Γ. The weak indirect transitions due to momentum conservation effectively reinforce its characterization as a direct semiconductor.[3,8]

The native point defects in β-Ga_2O_3 include gallium vacancies (V_{Ga}) located at both tetrahedral (Ga_I) and octahedral (Ga_{II}) sites, as well as oxygen vacancies at threefold coordinated sites (O_I and O_{II}) and fourfold coordinated sites (O_{III}). These vacancies can exist in different charge states, such as doubly ionized (V_{Ga}^{2-}) and singly ionized (V_{Ga}^{-}). Gallium vacancies in β-Ga_2O_3 act as deep acceptors and are observable at room temperature.[9] The formation energies of gallium vacancies in β-Ga_2O_3 vary depending on the oxygen availability in the environment, in oxygen-rich conditions, gallium vacancies are more likely to form due to lower formation energies, while in Ga-rich conditions, these vacancies serve as compensating acceptors, effectively reducing conductivity.[10] Oxygen vacancies in β-Ga_2O_3 function as deep donor defects. In oxygen-poor environments, the formation energy of these vacancies is negative, facilitating their creation. Conversely, in oxygen-rich atmospheres, the formation energy becomes positive for neutral oxygen vacancies, making it difficult to generate high concentrations of these defects under such conditions. Essentially, the presence of oxygen vacancies depends significantly on the oxygen partial pressure: they are more prevalent and easier to form in oxygen-deficient environments compared to oxygen-rich ones.[7,8] Apart from the Ga and oxygen vacancies, Ga interstitials (Ga_i) are also considered as shallow donors and could act as an alternative source of n-type conductivity, but the recent calculation suggests that Ga_i is highly mobile and it has a large formation energy (>2.5 eV) at extreme oxygen-poor growth conditions, which make them less likely to be present.[11,12]

Several epitaxial methods have been developed for the epitaxial growth of β-Ga_2O_3 thin films, each with its own advantages and limitations. One of the most prevalent techniques is Metal-Organic Chemical Vapor Deposition (MOCVD), known for producing high-quality layers with controlled purity, uniformity, and composition at practical growth rates. A variant of MOCVD, Mist Chemical Vapor Deposition (Mist-CVD), offers a non-vacuum, solution-based approach that is scalable and cost-effective, operating at lower growth temperatures. However, both MOCVD and Mist-CVD suffer from relatively slow growth rates.[3,4] To achieve higher deposition rates, Hydride Vapor Phase Epitaxy (HVPE) is employed, capable of reaching speeds up to 250 µm/h.[4,13] Despite its rapid growth, HVPE often results in rough surface morphology with a high density of defects and pits, which can be detrimental for device processing.[4] Pulsed Laser Deposition (PLD) represents another versatile method for depositing complex oxide thin films and heterostructures. It allows for precise control over the film's composition, maintaining the integrity of the target's composition for impurity doping or alloying. However, PLD can introduce high-energy ions from the target, potentially creating point defects that affect the film's electrical properties.[11] Molecular Beam Epitaxy (MBE) offers another approach for growing β-Ga_2O_3 thin films, characterized by exceptionally high quality due to its ultra-high vacuum environment (10^{-9} Torr) and precise control over source materials,[4,14] although like MOCVD and Mist-CVD, MBE suffers from a slow deposition rate.

Due to its large direct bandgap (~4.9 eV), exceptional physical and chemical stability, high critical electric field strength (~8 MV/cm), and impressive figure-of-merit (FOM),[4] β-Ga_2O_3 is highly suitable for power electronic and optoelectronic devices, including solar-blind UV photodetectors,[15–17] gas sensors,[18,19] and field-effect transistors.[20–22] However, β-Ga_2O_3 material itself faces several challenges, particularly in achieving high-quality thin film growth via molecular beam epitaxy (MBE) and p-type doping. On one hand, to attain superior thin films with minimal defects and roughness, numerous variables must be meticulously controlled. These include substrate temperature, gallium temperature, and the temperatures of donors and acceptors (e.g., Sn for n-type doping, Mg for p-type doping). Additionally, precise regulation of oxygen partial pressure, growth duration, and annealing atmosphere is essential. On the other hand, p-type doping presents a significant hurdle due to several factors. Firstly, the O 2p states contribute to a nearly flat valence band maximum

(VBM), resulting in minimal dispersion and a high effective hole mass, thereby limiting hole mobility and practical p-type conductivity [3,4] Furthermore, oxygen vacancies act as deep donors that compensate for p-type acceptor impurities like Zn and Mg, further complicating efforts to achieve effective p-type β-Ga_2O_3 conductivity.[7]

To broaden its applications further, bandgap engineering is crucial. The ability to tune the bandgap enables the design and optimization of electronic and optoelectronic devices with greater flexibility and enhanced performance. In addition to modifying the crystalline disorder of Ga_2O_3 itself,[23] researchers have explored other materials for bandgap engineering. For instance, InGaO[11,24–27] (bandgap ~3.88 to ~5.0 eV) and ZnGaO[28–30] (bandgap ~4.7 to ~5.1 eV) have been utilized extensively in applications such as solar-blind photodetectors and thin film transistors, offering lower bandgap alternatives. Conversely, AlGaO (bandgap ~4.85 to ~7.1 eV) [11,31–33] serves as a bandgap-increasing candidate that has been thoroughly investigated. As an alternatively viable bandgap-increasing candidate, MgGaO thin films can be construed as a mixture of Ga_2O_3 and MgO materials, allowing for potential bandgap tuning within the range of approximately 4.9 to 7.8 eV, which are awaiting systematic investigation. In addition, there is a lack of comprehensive photoluminescence (PL) studies of MgGaO thin films, although several room temperature[34–37] and a few temperature-dependent[38] PL studies of Mg-doped β-Ga_2O_3 were conducted, and preliminary room temperature PL studies of $MgGa_2O_4$ were reported.[39,40] Thus, this thesis work systematically investigates MgGaO thin films, focusing on MBE growth, phase transitions, film characterizations, and PL properties.

1.2 Molecular beam epitaxy (MBE)

Figure 1.1(a) illustrates the schematic of the RF oxygen plasma-assisted molecular beam epitaxy (MBE) system employed in this study (SVT Associates, Inc.). This system is equipped with six individual sources: Al, Ga, Sn, Zn, Mg, and oxygen, each of which can be independently controlled using shutters and exchanged with other materials. Oxygen partial pressure is precisely regulated using an MKS mass flow controller. **Figure 1.1(b)** depicts the steps involved in the growth of MgGaO thin films. These films were deposited on two-inch c-plane sapphire substrates. Prior to growth, substrates underwent cleaning with Piranha solution (H_2O_2: H_2SO_4 = 3: 5) at 200 °C for 20 minutes, followed by rinsing with deionized water and drying with nitrogen gas before immediate transfer to the loadlock chamber. High-purity elemental Mg (4N) and Ga shots (6N purity, Alfa Aesar) were utilized for film deposition. An 800 °C pre-growth annealing process lasting 20 minutes was conducted to achieve an atomically clean surface under high vacuum conditions of 10^{-9} torr. Parameters such as sample growth temperature, Ga and Mg effusion cell temperatures, oxygen flux, and growth duration were adjusted as required. Following

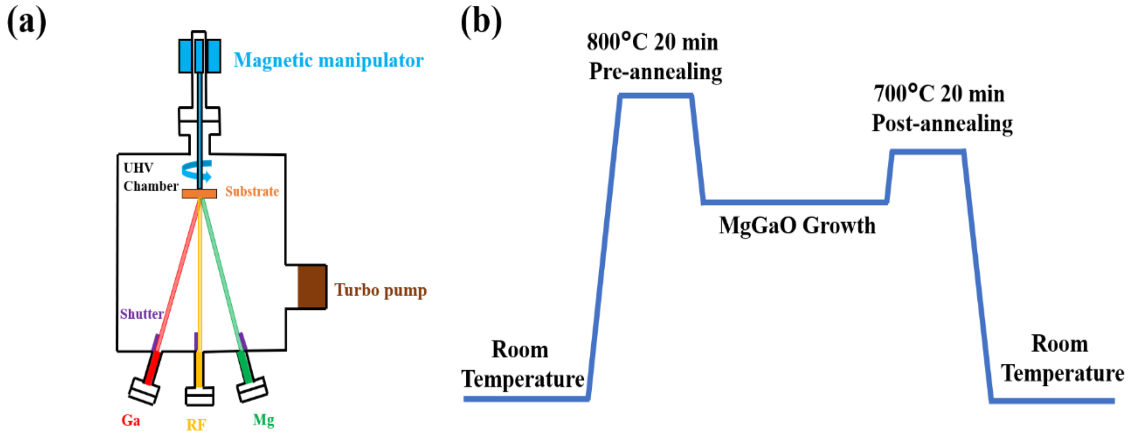

Figure 1.1 (a) Schematic of MBE system. (b) MgGaO thin film growth steps.

the completion of the growth process, a post-growth annealing step at 700 °C for 20 minutes was performed either in the presence or absence of an O_2 atmosphere.

1.3 Chapter's arrangement

In this dissertation, we presented a systematic investigation of MgGaO thin films, emphasizing molecular beam epitaxy (MBE) growth, phase transitions, film characterizations, and photoluminescence (PL) properties.

In Chapter 2, we are aiming to explore the growth conditions of β-MgGaO single crystalline thin films. The study involved the growth of β-MgGaO thin films using MBE focusing on engineering the bandgaps of β-MgGaO films within the range of 5.03 to 5.22 eV by varying the Mg^{2+} atomic percentage. Based on these films, β-MgGaO metal-semiconductor-metal (MSM) photodetectors were fabricated with Pt/Au metal contacts and subsequently characterized. The findings suggest that ultrawide bandgap (UWBG) β-MgGaO semiconductors hold significant promise for applications in deep-UV photodetection.

MgGaO can be construed as a mixture of Ga_2O_3 and MgO materials, thus its bandgap may be tuned between ~4.9 and ~7.8 eV. In Chapter 2, β-MgGaO was successfully synthesized; however, the conditions for phase transition from β phase to mixed phase and ultimately to rocksalt phase in the MgGaO alloy system with increasing Mg content remain unclear. The structural and optical properties of films in different phases have yet to be characterized. Therefore, Chapter 3 focused on growing twenty MgGaO thin film samples via plasma-assisted MBE, spanning a range of Mg/Ga atomic percentages from 0 at.%/100 at.% to 100 at.%/0 at.%. This investigation aimed to elucidate the phase transformations, film quality, lattice parameters, surface morphology, optical bandgap characteristics, and epitaxial relationship between MgGaO films and c-sapphire substrates as a function of Mg atomic percent. These findings highlight the potential for future device applications utilizing high-quality, tunable bandgap MgGaO thin films.

Previous studies on MgGaO phase transitions have not explored spinel magnesium gallate ($MgGa_2O_4$) at the specific composition of 33.33% Mg at.% and 66.67% Ga at.%. In addition, molecular beam epitaxy (MBE), known for its precision in epitaxial growth, has not yet been employed for growing $MgGa_2O_4$. Furthermore, room temperature photoluminescence (PL) studies of native defects within $MgGa_2O_4$ are sparse, hindering a comprehensive understanding of its PL mechanism. Therefore, Chapter 4 of this dissertation focused on the epitaxial growth of $MgGa_2O_4$ films using MBE. The study investigated structural, optical, and surface morphology properties of $MgGa_2O_4$ films. Particularly, it included detailed PL investigations, encompassing power-dependent and temperature-dependent PL analyses, to elucidate the PL mechanisms associated with native defects in $MgGa_2O_4$.

Following the epitaxial growth of spinel $MgGa_2O_4$ films and subsequent photoluminescence (PL) studies, the phase transition conditions from β phase to spinel phase remained poorly understood. Furthermore, the PL study of β-MgGaO was rarely reported but only limited to several room temperature and a few temperature-dependent PL investigations on Mg-doped β-Ga_2O_3. Therefore, Chapter 5 of this dissertation focused on the growth of nine MgGaO thin film samples with Mg atomic percentages ranging from 0 to 15.26% (normalized across Mg, Ga, and O elements in the alloys). The study comprehensively examines structural transformations, film quality, lattice parameters, optical bandgap, and transmittance properties of these MgGaO thin films. Moreover, extensive PL studies, including power-dependent and temperature-dependent measurements, are conducted to elucidate the PL characteristics of these materials.

These chapters collectively represent a systematic investigation into MgGaO thin films. Finally, Chapter 6 will provide a concise summary and conclusion of the dissertation work.

1.4 References

[1] A. A. Burk, M. J. O'Loughlin, R. R. Siergiej, A. K. Agarwal, S. Sriram, R. C. Clarke, M. F. MacMillan, V. Balakrishna, C. D. Brandt, *Solid-State Electronics* **1999**, *43*, 1459.

[2] E. Monroy, F. Omnès, F. Calle, *Semicond. Sci. Technol.* **2003**, *18*, R33.

[3] Z. Galazka, *Semicond. Sci. Technol.* **2018**, *33*, 113001.

[4] S. J. Pearton, J. Yang, P. H. Cary IV, F. Ren, J. Kim, M. J. Tadjer, M. A. Mastro, *Applied Physics Reviews* **2018**, *5*, 011301.

[5] S. Geller, *The Journal of Chemical Physics* **1960**, *33*, 676.

[6] H. Peelaers, C. G. Van de Walle, *physica status solidi (b)* **2015**, *252*, 828.

[7] L. Dong, R. Jia, B. Xin, B. Peng, Y. Zhang, *Sci Rep* **2017**, *7*, 40160.

[8] J. B. Varley, J. R. Weber, A. Janotti, C. G. Van de Walle, *Applied Physics Letters* **2010**, *97*, 142106.

[9] B. E. Kananen, L. E. Halliburton, K. T. Stevens, G. K. Foundos, N. C. Giles, *Applied Physics Letters* **2017**, *110*, 202104.

[10] J. B. Varley, H. Peelaers, A. Janotti, C. G. V. de Walle, *J. Phys.: Condens. Matter* **2011**, *23*, 334212.

[11] J. Zhang, J. Shi, D.-C. Qi, L. Chen, K. H. L. Zhang, *APL Materials* **2020**, *8*, 020906.

[12] M. J. Tadjer, J. L. Lyons, N. Nepal, J. A. Freitas, A. D. Koehler, G. M. Foster, *ECS J. Solid State Sci. Technol.* **2019**, *8*, Q3187.

[13] H. Murakami, K. Nomura, K. Goto, K. Sasaki, K. Kawara, Q. T. Thieu, R. Togashi, Y. Kumagai, M. Higashiwaki, A. Kuramata, S. Yamakoshi, B. Monemar, A. Koukitu, *Appl. Phys. Express* **2014**, *8*, 015503.

[14] K. Sasaki, M. Higashiwaki, A. Kuramata, T. Masui, S. Yamakoshi, *Journal of Crystal Growth* **2014**, *392*, 30.

[15] S. Oh, C.-K. Kim, J. Kim, *ACS Photonics* **2018**, *5*, 1123.

[16] B. Zhao, F. Wang, H. Chen, L. Zheng, L. Su, D. Zhao, X. Fang, *Advanced Functional Materials* **2017**, *27*, 1700264.

[17] Y. Qin, L. Li, X. Zhao, G. S. Tompa, H. Dong, G. Jian, Q. He, P. Tan, X. Hou, Z. Zhang, S. Yu, H. Sun, G. Xu, X. Miao, K. Xue, S. Long, M. Liu, *ACS Photonics* **2020**, *7*, 812.

[18] U. Lampe, M. Fleischer, H. Meixner, *Sensors and Actuators B: Chemical* **1994**, *17*, 187.

[19] Z. Liu, T. Yamazaki, Y. Shen, T. Kikuta, N. Nakatani, Y. Li, *Sensors and Actuators B: Chemical* **2008**, *129*, 666.

[20] S. Sharma, K. Zeng, S. Saha, U. Singisetti, *IEEE Electron Device Letters* **2020**, *41*, 836.

[21] M. Higashiwaki, K. Sasaki, T. Kamimura, M. Hoi Wong, D. Krishnamurthy, A. Kuramata, T. Masui, S. Yamakoshi, *Applied Physics Letters* **2013**, *103*, 123511.

[22] K. Zeng, A. Vaidya, U. Singisetti, *IEEE Electron Device Letters* **2018**, *39*, 1385.

[23] Y. Chen, Y. Lu, X. Yang, S. Li, K. Li, X. Chen, Z. Xu, J. Zang, C. Shan, *Materials Today Physics* **2021**, *18*, 100369.

[24] F. Zhang, K. Saito, T. Tanaka, M. Nishio, Q. Guo, *Solid State Communications* **2014**, *186*, 28.

[25] F. Zhang, K. Saito, T. Tanaka, M. Nishio, Q. Guo, *Journal of Alloys and Compounds* **2014**, *614*, 173.

[26] T. Oshima, S. Fujita, *physica status solidi c* **2008**, *5*, 3113.

[27] I. Hamberg, C. G. Granqvist, K.-F. Berggren, B. E. Sernelius, L. Engström, *Phys. Rev. B* **1984**, *30*, 3240.

[28] D. Wang, K. Ge, D. Meng, Z. Chen, *Materials Letters* **2023**, *330*, 133251.

[29] Y.-S. Shen, W.-K. Wang, R.-H. Horng, *IEEE Journal of the Electron Devices Society* **2017**, *5*, 112.

[30] A. K. Singh, C.-C. Yen, K.-P. Chang, D.-S. Wuu, *Journal of Luminescence* **2023**, *260*, 119836.

[31] A. F. M. A. U. Bhuiyan, Z. Feng, J. M. Johnson, H.-L. Huang, J. Hwang, H. Zhao, *Appl. Phys. Lett.* **2020**, *117*, 142107.

[32] F. Zhang, K. Saito, T. Tanaka, M. Nishio, M. Arita, Q. Guo, *Appl. Phys. Lett.* **2014**, *105*, 162107.

[33] R. Miller, F. Alema, A. Osinsky, *IEEE Transactions on Semiconductor Manufacturing* **2018**, *31*, 467.

[34] T. Onuma, S. Fujioka, T. Yamaguchi, M. Higashiwaki, K. Sasaki, T. Masui, T. Honda, *Applied Physics Letters* **2013**, *103*, 041910.

[35] Y. Wang, P. T. Dickens, J. B. Varley, X. Ni, E. Lotubai, S. Sprawls, F. Liu, V. Lordi, S. Krishnamoorthy, S. Blair, K. G. Lynn, M. Scarpulla, B. Sensale-Rodriguez, *Sci Rep* **2018**, *8*, 18075.

[36] M. M. Islam, D. Rana, A. Hernandez, M. Haseman, F. A. Selim, *Journal of Applied Physics* **2019**, *125*, 055701.

[37] K. Zhang, Z. Xu, S. Zhang, H. Wang, H. Cheng, J. Hao, J. Wu, F. Fang, *Physica B: Condensed Matter* **2021**, *600*, 412624.

[38] K. Zhang, Z. Xu, J. Zhao, H. Wang, J. Hao, S. Zhang, H. Cheng, B. Dong, *Journal of Alloys and Compounds* **2021**, *881*, 160665.

[39] Z. Liu, P. Hu, X. Jing, L. Wang, *J. Electrochem. Soc.* **2008**, *156*, H43.

[40] D. V. Mlotswa, L. L. Noto, S. J. Mofokeng, K. O. Obodo, V. R. Orante-Barrón, B. M. Mothudi, *Optical Materials* **2020**, *109*, 110134.

Chapter 2: Metal-semiconductor-metal photodetectors based on β-MgGaO thin films

2.1 Introduction

Wide bandgap semiconductor materials such as SiC and GaN have contributed to the development of integrated circuits, power electronics, communication and computing designs, and many novel ultraviolet (UV) optoelectronic applications.[1–5] Nowadays, ultrawide bandgap (UWBG) semiconductor materials with a bandgap larger than ~4 eV, such as AlN, diamond, and Ga_2O_3 have been considered as the next generation semiconductors for military and civilian applications.[5] Among these materials, Ga_2O_3 has been studied extensively recently, for example, β-phase Ga_2O_3 Schottky barrier diode,[6–8] and metal oxide semiconductor field effect transistors [9–11] have been demonstrated to have great potential in power electronic applications. Furthermore, β-Ga_2O_3 offers promising chances to be applied in UV light detecting and imaging, ozone hole monitoring, etc.[12–15] However, although the n-type conductivity using crystalline disorder method or Sn, Ge, Si and F dopants have been demonstrated,[6,16–24] robust p-type conductivity is still very difficult to realize by using Be, Li, Mg, Zn, Ca, Sr and N dopants.[25–29] This is because the O 2p states of Ga_2O_3 make the top of valence band very flat. Small dispersion of the valence band maximum results in a high effective hole mass and in turn, a very low hole mobility, which makes a p-type conductivity impractical.[6,30] Moreover, the oxygen vacancies are usually generated in these materials, which act as deep donors and compensate the p-type acceptor impurities such as Zn^{2+} and Mg^{2+}. This dilemma has greatly limited the potential of Ga_2O_3 for both power electronics and optoelectronics applications.

To further enhance the performance of Ga_2O_3 radio frequency (RF) power electronic and optoelectronic devices, Ga_2O_3 heterostructures are essential as well. Candidates such as AlGaO[31–33] and ZnGaO[34,35] alloys have been reported to show great promises in terms of their bandgap tunability and compatibility with Ga_2O_3. In this work, we explore another UWBG semiconductor material, namely, magnesium gallium oxide (MgGaO). Although MgGaO amorphous films have been synthesized and reported,[36,37] β-phase MgGaO single crystalline thin films were rarely reported. MgGaO is promising due to the following reasons: MgGaO can be considered as a mixture of Ga_2O_3 and MgO materials thus its bandgap can be tuned wider than that of Ga_2O_3. Moreover, the substitution of di-valent Mg ions into tri-valent Ga ion sites in the MgGaO can significantly tune its electrical conductivity, which has a potential toward helping achieve p-type conductivity in these UWBG semiconductors.

In this chapter, MgGaO ternary alloy thin films with ultrawide bandgaps up to ~5.22 eV were grown by plasma-assisted molecular beam epitaxy (MBE). Solar blind metal-semiconductor-metal (MSM) photodetectors with good responsivity were fabricated based on the MgGaO thin films with varying Mg compositions. The wavelength, temperature, and power dependent I-V characteristics, photocurrent spectra and dynamics of these photodetectors were studied.

2.2 Experimental Details

2.2.1 Film growth

β-MgGaO thin films were grown on two-inch c-sapphire substrates by using an MBE system equipped with an RF plasma assisted oxygen source (SVT Associates, Inc.). The substrates were firstly cleaned with Isopropyl Alcohol (IPA) solution (IPA: de-ionized water = 1:1) then in Piranha solution (H_2O_2: H_2SO_4 = 3: 5) at 200 °C for 20 minutes and rinsed by deionized water, finally dried by nitrogen gas, and transferred to the MBE loadlock chamber immediately. High-purity elemental Mg and Ga shots (6N) (Alfa Aesar) were placed in effusion cells as the growth sources. A pre-growth annealing process was performed at a high temperature of 800 ˚C for 20 minutes to achieve an atomic level surface within high vacuum chamber on the order of 10^{-9} torr. During the growth of the samples, the temperature of the substrate was kept at 650 ˚C and RF plasma assisted oxygen source with a flux of 2.5 sccm was used at a power of 400 W. The temperature of Ga cell was set to 750 ˚C, and the Mg temperature was set to 380, 385, and 390 ˚C for sample A, B and C, respectively. After 1-h growth, a post-growth annealing process at 700 ˚C under oxygen atmosphere was performed for 20 minutes before cooling to the room temperature. A pure Ga_2O_3 sample was grown under similar growth condition but without Mg incorporation as a reference. The growth details of these samples are listed in **Table S2.1** (Supporting Information).

2.2.2 Film characterization

The film thickness of the samples were measured by an Filmetrics 3D Profilometer. Surface morphologies of films were characterized by a TESCAN Vega3 SBH scanning electron microscope (SEM) and a Dimension 3100 Nanoman atomic force microscope (AFM). The Mg compositions were measured by energy-dispersive X-ray spectroscope (EDS) in the same SEM instrument and a Kratos AXIS Ultra DLD X-ray photoelectron spectroscopy (XPS). X-ray diffraction (XRD) two-theta and omega scans of the films were measured by using a Bruker D8 Advance X-ray diffractometer and Rigaku SmartLab X-ray diffractometer with Cu Kα ($\lambda = 0.15405$ nm) radiation, respectively. The phonon energies of the films were investigated by a confocal Raman microscope equipped with a high-resolution laser with a wavelength of 532 nm and a power of 60 mW (LabRAM HR, HORIBA Scientific). Room temperature ground state absorption and transmittance spectra of the samples were measured using a high-performance UV-Vis-NIR spectrophotometer (Cary 5000, Agilent Inc.).

2.2.3 MSM photodetector device fabrication and characterization

MSM photodetectors with an interdigital Pt/Au (20 nm/100 nm) Schottky contact pattern were fabricated by using standard photolithography, e-beam evaporation and acetone lift off process. Optoelectronic properties of wavelength-dependent, temperature-dependent, and power-dependent I-V characteristics, responsivity, and current-time (I-t) dynamics were measured by using a Signatone H100 series probe station and an Agilent 4155C semiconductor parameter analyzer under the light illumination of 265 nm and 280 nm. Photocurrent spectra were acquired by using a UV enhanced xenon arc lamp with a monochromator set-up (Oriel Cornerstone 260, Newport Corporation).

2.3 Results and Discussion

2.3.1 Characterizations of β-MgGaO single crystal films

Samples A, B and C have a film thickness of ~83.1, 92.9 and 93.2 nm, respectively.

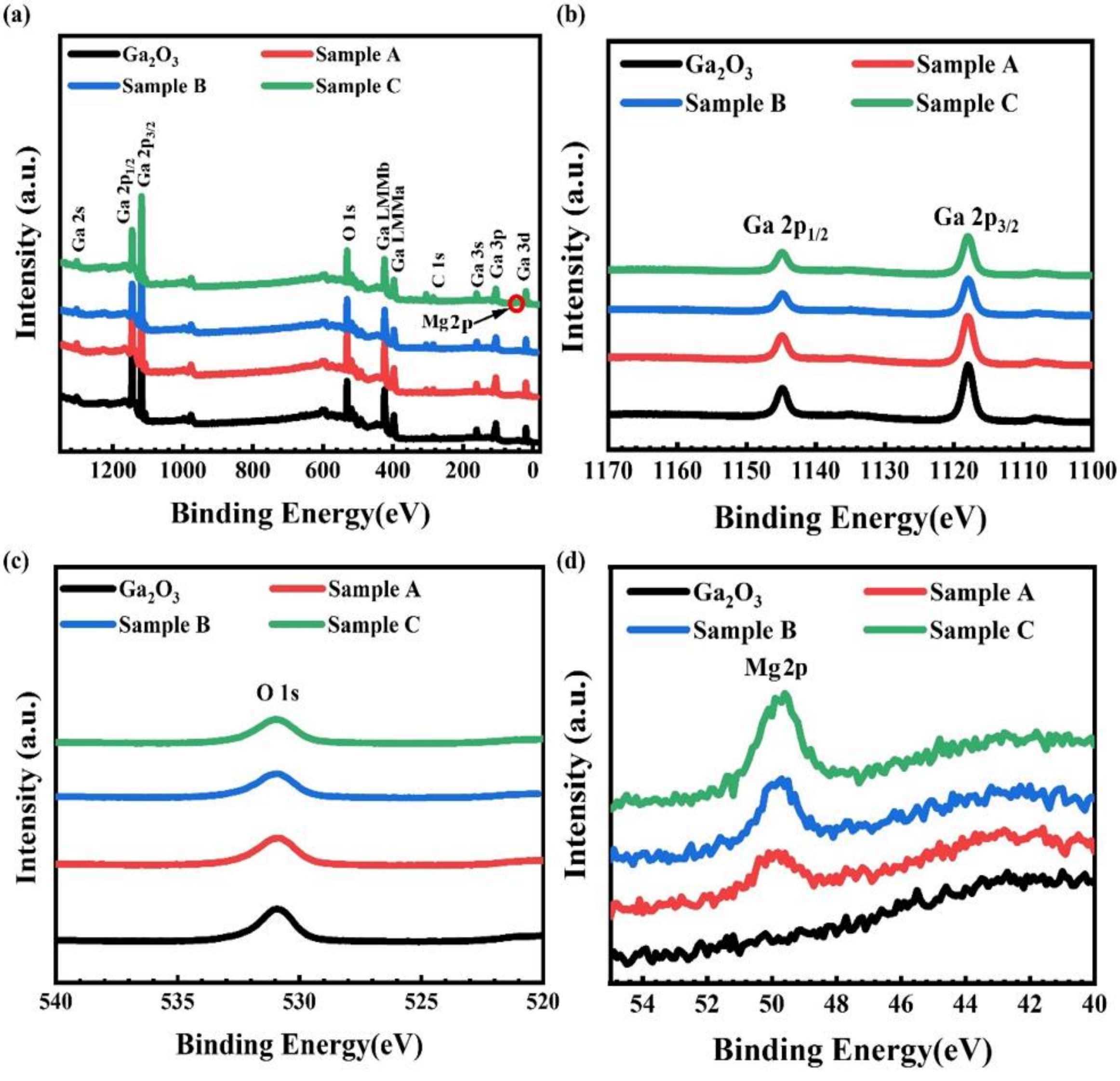

Figure 2.1 XPS analysis of reference Ga_2O_3, and MgGaO samples A, B, and C: (a) survey peaks, (b) Ga 2p spectra, (c) O 1s spectra, (d) Mg 2p spectra.

Figure 2.1(a) shows XPS survey peaks of reference Ga_2O_3, and MgGaO samples A, B, and C. **Figure 2.1(b)-(d)** show XPS Ga 2p, O 1s and Mg 2p spectra, respectively. The Ga $2p_{3/2}$ and Ga $2p_{1/2}$ are located at ~1116.4 eV and ~1143.2 eV, respectively (**Figure 2.1(b)**), O 1s is located at ~543.1 eV (**Figure 2.1(c)**), and Mg 2p is located at ~49.78 eV (**Figure 2.1(d)**). Based on these peaks, the relative atomic composition of Ga_2O_3, and MgGaO samples A, B, and C is estimated and summarized in **Table 2.1**. The Mg atomic percent of samples A, B, and C were recorded as 1.8%, 3.4% and 4.0%, respectively. The EDX characterization of elemental compositions of MgGaO thin films showed reasonably close numbers as the XPS data (Supporting information, **Figure S2.1**).

Table 2.1 Relative atomic composition of Ga_2O_3, MgGaO samples A, B, and C.

Samples	Ga (at. %)	O (at. %)	Mg (at. %)
Ga_2O_3	35.6	64.4	0
A	33.8	64.4	1.8
B	28.9	67.7	3.4
C	31.1	64.9	4.0

Figure 2.2 shows morphological characterization results. As seen from the SEM images in **Figure 2.2(a)-(d)**, all surfaces are relatively smooth, while smoother surface are observed in MgGaO thin films with less incorporated Mg. The AFM 5 μm × 5 μm images are shown in **Figure 2.2(e)-(h)** and root mean square (RMS) roughness is 1.29, 0.45, 0.68, and 0.80 nm for the reference Ga_2O_3 sample and MgGaO samples A, B and C, respectively, which is in agreement with the SEM results.

Figure 2.3(a) shows XRD pattern in θ/2θ scan mode of Ga_2O_3, and MgGaO samples A, B, and C. Three typical diffraction peaks located at around 19.12 °, 38.50 ° and 59.14 ° correspond to the β phases of $(\bar{2}01)$, $(\bar{4}02)$, and $(\bar{6}03)$, respectively, implying a clear monoclinic structure. After Mg atoms are incorporated into Ga_2O_3, all these diffraction angles exhibit an obvious decrease since the ionic radius of Mg^{2+} ions (0.72 Å) are larger than that of Ga^{3+} ions (0.62 Å). According to Bragg's Law, the interplanar distance d will become larger and the angle of 2θ will decrease when Mg^{2+} replace Ga^{3+} ions.[27,38] The XRD two-theta scan data suggest that MgGaO samples A, B and C maintain a good β phase structure. **Figure S2.2** (Supporting Information) shows a schematic of MgGaO monoclinic structure, assuming two Ga atoms are replaced with two Mg atoms in Ga_I site. **Figure 2.3(b)** shows the normalized XRD rocking curves of samples A, B, C and reference Ga_2O_3 sample, respectively. The full width at half maximum (FWHM) of the peak $(\bar{4}02)$ of β-Ga_2O_3, Samples A, B and C were recorded as 0.0756°, 0.0611°, 0.0608° and 0.0565°, respectively. As Mg composition increases, the FWHM reduces slightly but monotonously,

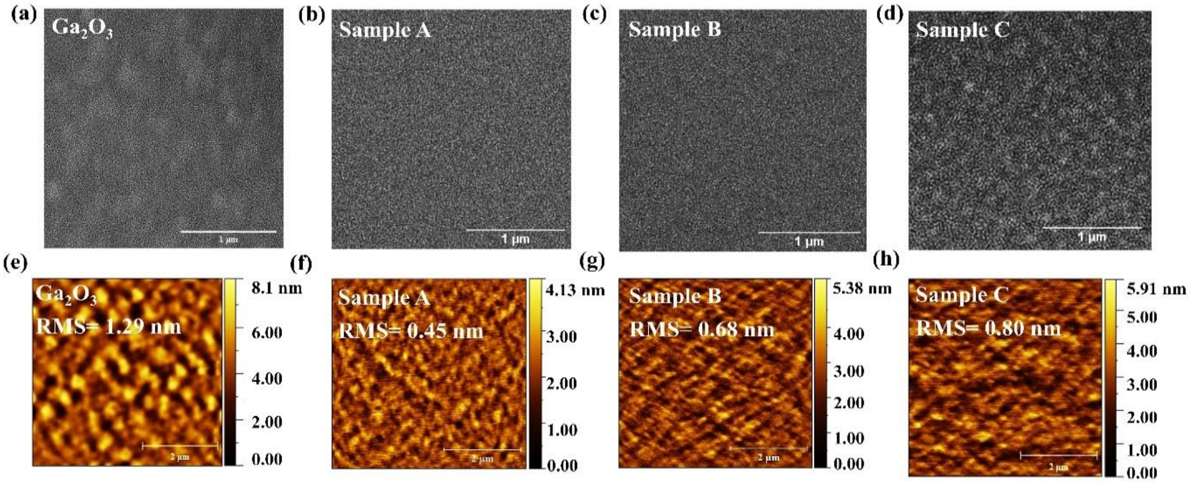

Figure 2.2 (a) – (d) SEM images, (e) – (h) AFM images of reference Ga_2O_3, and MgGaO samples A, B, and C, respectively.

which may be due to less lattice mismatch between the film and substrate as more Mg is incorporated. Compared to the reported 1.494° FWHM of $(\bar{2}01)$ peak of β-Ga_2O_3 thin film,[39] it indicates a higher quality of our films.

Optical phonon modes of Ga_2O_3, sample A, B, and C are shown in **Figure 2.3(c)**, four of five B_g and three of ten A_g optical phonon modes Raman-active peaks, namely, $B_g^{(1)\text{-}(2)}$ and $B_g^{(4)\text{-}(5)}$, $A_g^{(1)}$, $A_g^{(5)}$ and $A_g^{(10)}$ modes are observed in the MgGaO thin films. As a reference, four of five B_g and five of ten A_g optical phonon modes Raman-active peaks, namely, $B_g^{(1)\text{-}(3)}$, $B_g^{(5)}$ and $A_g^{(1)\text{-}(3)}$, $A_g^{(5)}$ and $A_g^{(10)}$ modes, are observed in the Ga_2O_3 sample. The details of peak positions of all samples are summarized in **Table S2.2** (Supporting Information). Compared to Raman peaks of Ga_2O_3, $A_g^{(2)\text{-}(3)}$, $B_g^{(3)}$ modes disappear in all three MgGaO samples. In addition, the peak intensity of $A_g^{(2)\text{-}(3)}$ and $B_g^{(1)\text{-}(2)}$ modes is

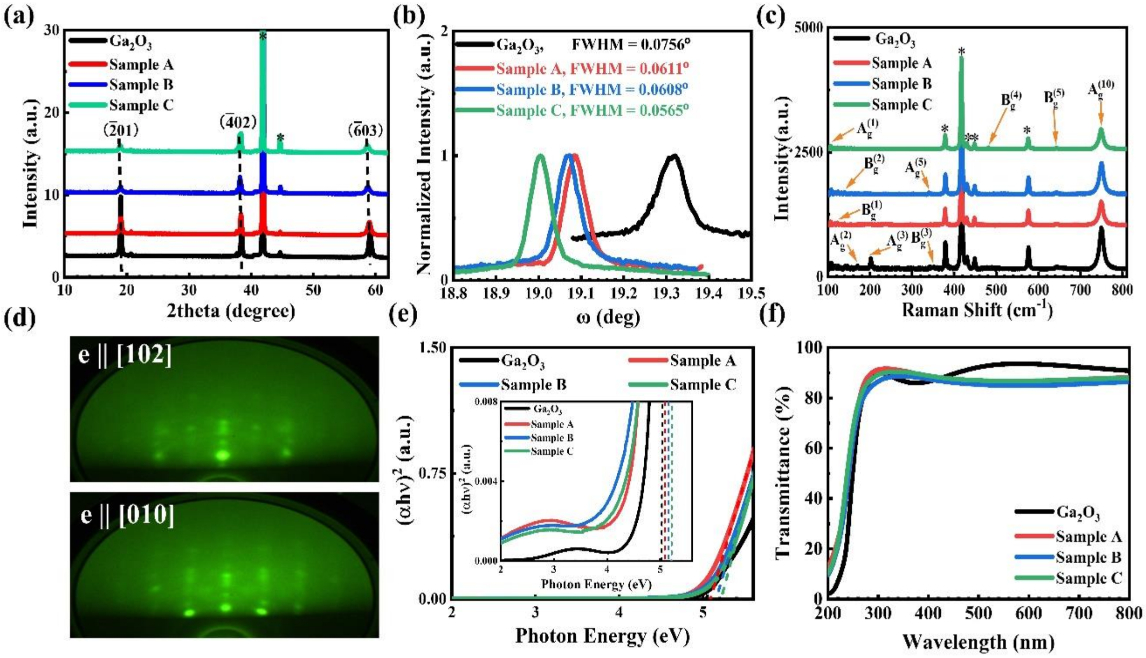

Figure 2.3 (a) XRD pattern in θ/2θ scan mode, (b) XRD rocking curves, (c) Raman spectra, (d) RHEED patterns of MgGaO sample A, (e) Tauc-plot of the absorption spectra. Inset shows absorption peak between 2 and 4 eV, (f)Transmittance spectra of Ga_2O_3, samples A, B, and C.

reduced, which implies the vibration and translation of the Ga_IO_4 tetrahedral chains after Mg^{2+} atoms are incorporated. The change of $A_g^{(5)}$ and $B_g^{(3)\text{-}(4)}$ modes indicates the deformation of the $Ga_{II}O_6$ octahedral chains and the translation of the Ga_IO_4 tetrahedral chains, while the change of $A_g^{(10)}$ mode indicates the stretching and bending of the Ga_IO_4 tetrahedral chains.[40,41] Apart from the change of peak intensity, the MgGaO Raman peaks blue shift with respect to that of Ga_2O_3 because larger bond lengths lead to smaller wavenumber of Raman peaks. The calculated average bond length for Mg-O bonds is 2.03 Å,[42] while average Ga-O bond length for tetrahedral is 1.83 Å and for octahedral is 2.00 Å.[43,44] The Mg-O bond length is larger than that of corresponding Ga-O bonds after Mg^{2+} replace Ga^{3+} sites, which is due to larger Mg^{2+} radius (0.72 Å) than Ga^{2+} radius (0.62 Å).[45] To sum up, the different Raman spectra between the MgGaO samples and the Ga_2O_3 reference sample indicate that lattice structure of MgGaO samples can be treated as the incorporation of Mg atoms in the lattice structure of Ga_2O_3. Nevertheless, further in-depth Raman study with an assistance from other characterizations are necessary to quantify exact locations of these Mg atoms and strain/relaxation of the films.[40,46]

Reflection high energy electron diffraction (RHEED) have been carried out to study the crystallinity of the samples. **Figure 2.3(d)** shows RHEED patterns of sample A $(\bar{2}01)$ plane along [102] and [010] azimuth, which were alternately observed every 30° rotation in the azimuthal direction. The streaky patterns indicate single crystal nature of the film, similar to the RHEED pattern of single crystal β-Ga_2O_3.[47] Based on the RHEED patterns, the in-plane lattice constants were calculated as ~3.06 Å and 5.34 Å, respectively.

Figure 2.3(e) shows Tauc-plot of the absorption spectra of Ga_2O_3, and MgGaO sample

A, B, and C thin films. The ultrawide bandgap absorption spectra reaching UVC region are obtained in all samples. The Tauc equation for semiconductors with direct bandgaps is expressed as[46]:

$$(\alpha h\upsilon)^2 = A(h\upsilon - E_g) \tag{1}$$

where α is the absorption coefficient, hυ is energy, A is a proportionality constant. By extrapolating the linear segment of absorption spectra to intersect the hυ-axis with a fitting straight line, the direct bandgap value of Ga_2O_3 sample is approximately 5.03 eV, which is in good agreement with the reported values.[48,49] It is noted that the experimental bandgaps of β-Ga_2O_3 ranging from 4.4 to 5.0 eV at room temperature were reported when the absorption or transmittance polarization was employed during the characterization.[50] The bandgaps of MgGaO thin film samples A, B and C are 5.09, 5.15, and 5.22 eV, respectively, which increases with the increase of Mg atomic percent. Inset in **Figure 2.3(e)** shows zoomed in absorption spectra of the samples, indicating a small broad absorption peak ~3.4 eV for Ga_2O_3, and ~2.6 eV for samples A, B, and C, which is in agreement with the photoresponse around 480 nm shown in Figure 5. The transmittance of light of these samples were also measured using the same spectrophotometer. Around 90% transmittance of light were observed across the spectrum for Ga_2O_3 and MgGaO samples A, B and C, as shown in **Figure 2.3(f)**.

2.3.2 Characterizations of β-MgGaO MSM photodetectors

The schematic diagram of β-MgGaO MSM photodetector is illustrated as an inset of **Figure 2.4(a)**. The electrodes are composed of 31 digits of the same size on each side with a length of 475.5 μm, a width of 5 μm and a spacing of 3 μm, the effective area of the photodetector is 9.1605 x 10^4 μm^2. **Figure 2.4(a)-(c)** show wavelength dependent I-V characteristics of the MSM devices based on samples A, B and C under dark, 265-nm and 280-nm light illumination with the same power density of 1.808 mW/cm^2, respectively. For all three devices based on samples A, B and C, the dark current is around 15 nA, 50

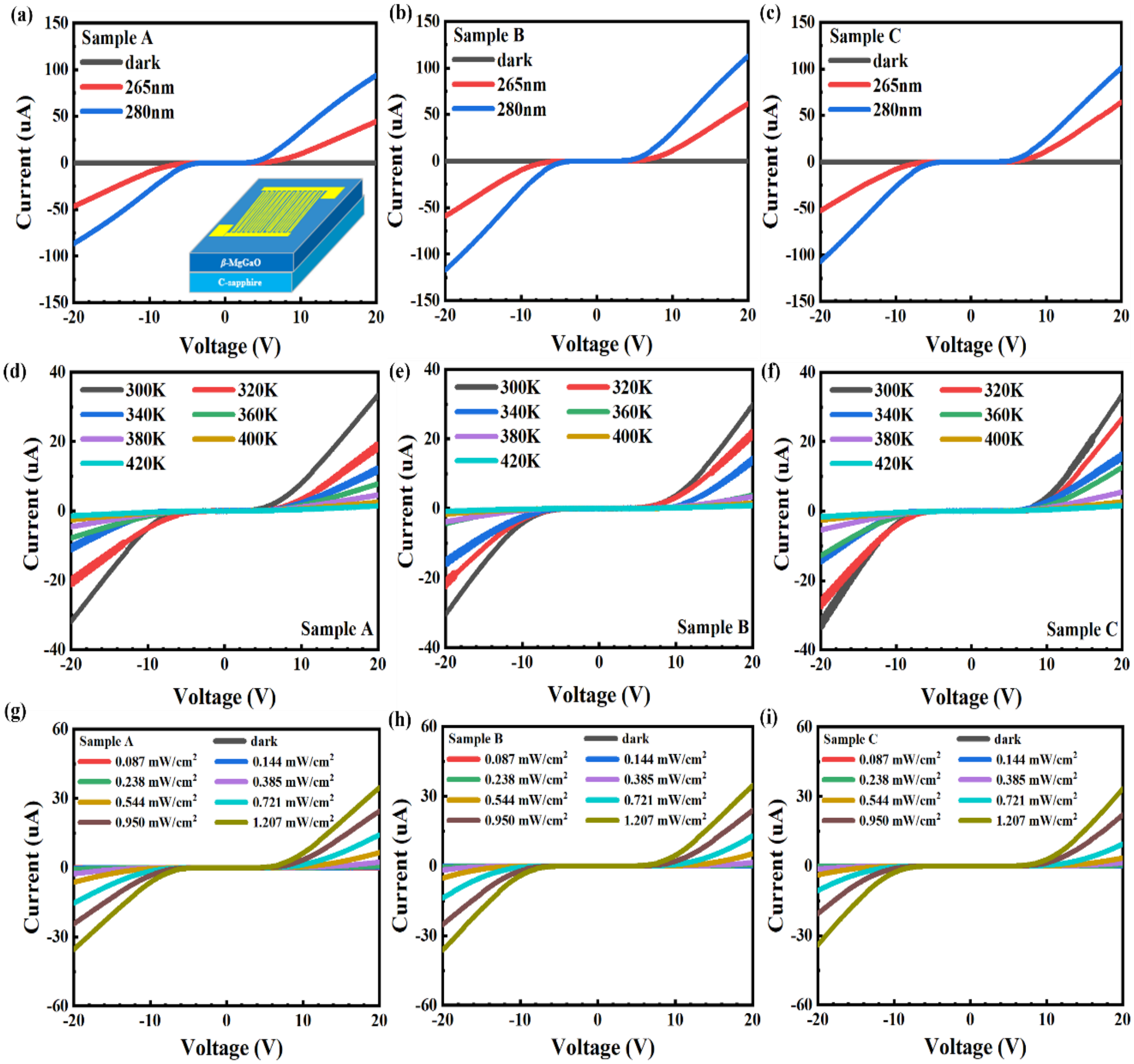

Figure 2.4 (a)-(c) I-V characteristics of Sample A, B and C under dark condition and UV light illumination of 1.808 mW/cm^2. The inset in (a) is a schematic diagram of the interdigital metal contact structure. (d)-(f) Temperature dependent I-V curves of Sample A, B and C under 265-nm illumination. (g)-(i) power dependent I-V curves of Sample A, B and C illuminated by the UV light centered at 265 nm at different light intensity.

μA under 265-nm illumination, and 100 μA under 280-nm illumination at a bias of 20 V, and the photo-to-dark current ratios > 10^3 are obtained for both kinds of illuminations.[51] For the fixed bias, photocurrent at longer wavelength (280 nm) illumination was larger than that at shorter wavelength (265 nm) illumination. This phenomenon can be ascribed to the different number of photogenerated carriers under illumination of different wavelengths but with constant incident power.[52–54] When incident light of shorter wavelength at 265 nm shines onto the films, less photons reach the films, yielding less photo carriers, in turn, smaller photocurrent.

Figure 2.4(d)-(f) show temperature dependent I-V characteristics of samples A, B and C under 265-nm UV illumination. The temperature ranges from 300 to 420 K with a step of 20 K. For all samples at a fixed bias (for example, 20 V), the photocurrent decreases as the increase of the temperature. It can be attributed to the enhancement of the nonradiative recombination mainly in forms of Shockley-Read-Hall (SRH) recombination, which is a compensating process of carrier generation induced by incident photons.[55] On one hand, the incident photons are absorbed to generate the electron-hole pairs contributing to the photocurrent, on the other hand, when the temperature increases, electrons in the conduction band and holes in the valence band move to the defect levels and recombine with each other to release phonons, resulting in the decrease of the photocurrent.

Figure 2.4(g)-(i) show power dependent I-V characteristics of the three samples under 265-nm light source with different power densities ranging from 0.087 mW/cm^2 to 1.207 mW/cm^2. The generated photocurrent increases with the increase of the incident power density since larger numbers of incident photons have been absorbed for the generation of more photocarriers.

Photocurrent spectra were acquired from MSM device samples A, B and C under different voltage ranging from 10 to 20 V at wavelengths ranging from 200 to 600 nm. **Figure 2.5(a)-(c)** show the results of three samples, respectively. The photocurrent increases as the increase of the bias for all three samples, indicating the more efficient collection of the photocarriers at higher bias. In each sample, two photocurrent peaks are

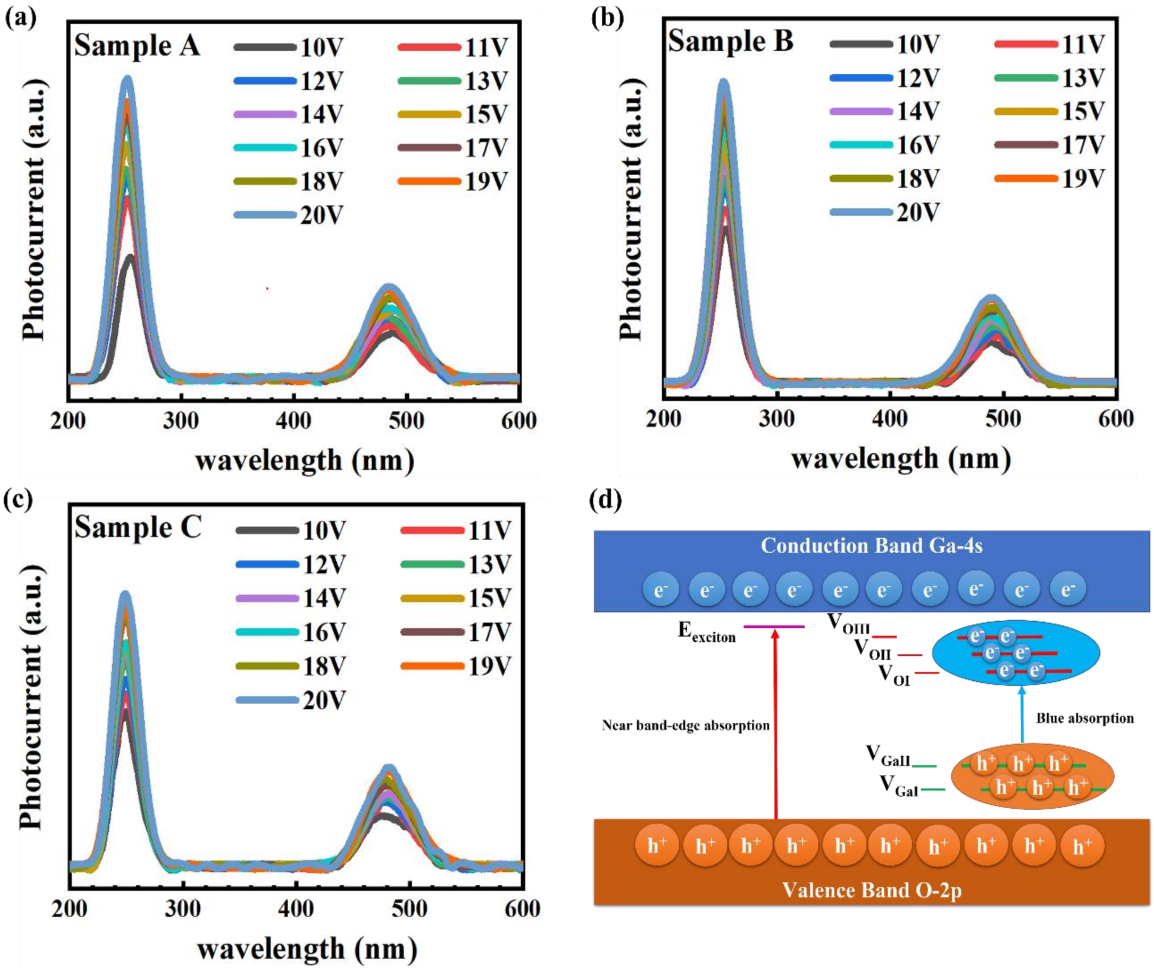

Figure 2.5 Photocurrent spectra of (a) Sample A, (b) Sample B, and (c) Sample C measured under different voltages. (d) A schematic model to illustrate the photocurrent mechanism in MgGaO thin films.

observed. The higher energy photo response is at a wavelength of 254, 253, and 247 nm (corresponding to 4.88, 4.90, and 5.02 eV in energy) for Samples A, B, and C, respectively. Compared with ~200-meV larger optical bandgap energies obtained in absorption experiment in respective samples, these photocurrent peaks may be associated with near-band-edge bound exciton absorption, assuming that the free exciton binding energy in the present MgGaO thin films is similar to 0.12 eV, a value attained for β-Ga_2O_3.[56] It is noted that the photocurrent peaks in the UV region for the three samples exhibit symmetric behavior. Similar symmetric photoresponses were also reported in MSM photodetectors based on β-Ga_2O_3 by other groups.[57–59] This phenomenon further strengthens the assignment of the UV photoresponse to be from near-band-edge absorption between relatively flat valence band and narrow "subbands" near the conduction band edge rather than straight band-to-band transition, which would have been more asymmetric due to the nonlinear density of state function of conduction band. A smaller energy photo response is at a wavelength around 485 nm (corresponding to 2.55 eV in energy) for three samples. The 2.55-eV blue absorption peak may originate from the transition between oxygen vacancy (V_O) energy levels and Ga vacancy (V_{Ga}) energy levels.[60–62] A schematic model

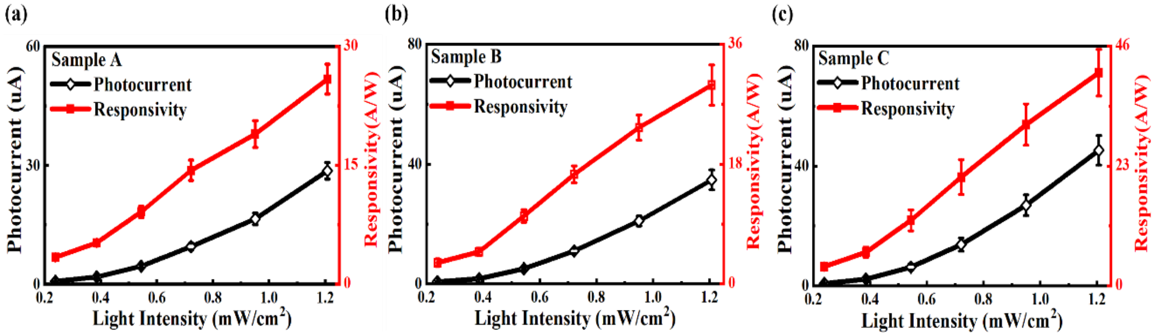

Figure 2.6 (a) - (c) Photocurrent and responsivity versus 265-nm light intensity under 20-V bias for samples A, B and C, respectively.

illustrating absorption processes contributing to photocurrent spectra is shown in **Figure 2.5(d)**.

The responsivity of MSM device samples A, B and C were measured. **Figure 2.6(a)-(c)** show photocurrent and responsivity as a function of 265-nm light intensity for three samples under 20-V bias, respectively. The photocurrent increases as the increase of the light intensity, which is in agreement with **Figure 2.4(g)-(i)**. The responsivity was calculated based on the following equation[63]:

$$R_\lambda = \frac{I_\lambda - I_d}{P_\lambda S} \qquad (2)$$

where I_λ is the photocurrent, I_d is the dark current, P_λ the incident light intensity and S is the effective illumination area. As shown in **Figure 2.6(a)-(c)**, the responsivity increases as the increase of the light intensity. The highest responsivities of samples A, B and C are 25.9, 29.88 and 40.88 A/W, respectively, at an incident power density of 1.207 mW/cm^2. In contrast, responsivities of 6.89, 0.19, and 0.89 A/W were reported for photodetectors based on semiconductors with similar wide bandgaps $ZnGa_2O_4$,[64] AlGaN,[65] and $MgGa_2O_4$, [66] respectively.

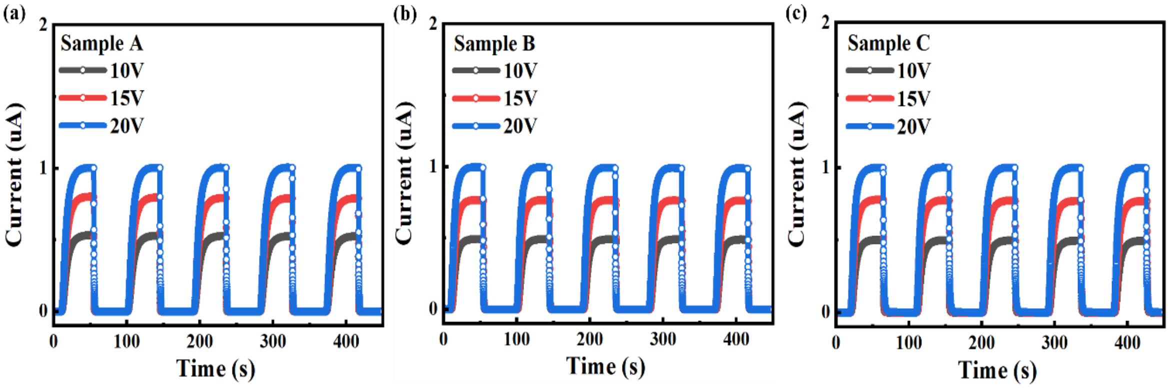

Figure 2.7 (a) - (c) Normalized I–t characteristics under 0.144 mW/cm^2 265-nm illumination at varying voltages of 10, 15, and 20 V, respectively for sample A, B and C.

Figure 2.7(a)-(c) show the normalized current-time (I-t) dynamics of the photocurrent of MSM device samples A, B and C, which were measured at the bias of 10, 15, and 20 V under 265-nm illumination with the light intensity of 0.144 mW/cm^2. The times for photocurrent increasing from 0 to 1-1/e of the steady value and decreasing from steady value to 1/e are defined as the rise and decay times, respectively. The rise and decay times of the dynamic change of the photocurrent at the bias of 20 V for samples A, B and C were statistically calculated as 6.13 s and 0.29 s, 4.85 s and 0.29 s, and 4.87 s and 0.47 s, respectively. It is noted that similar rise time of 13 s and decay time of 0.4 s were demonstrated from β-Ga_2O_3 thin film based photodetector.[67] Slightly larger decay time for device sample C indicates higher quality of the MgGaO film, which is in good agreement with the XRD rocking curves result in **Figure 2.3(b)**.

2.4 Conclusion

UWBG MgGaO thin films were grown by plasma-assisted MBE. The bandgaps of the β-phase MgGaO thin films were engineered from 5.03 to 5.22 eV by incorporating with different Mg^{2+} atomic percentage. The transmittance of all the samples are around 90%. Based on these MgGaO films, MSM photodetectors with Pt/Au metal contacts were fabricated and characterized. It was shown that the photo-to-dark current ratio is larger than 10^3 at a bias of 20 V. The photocurrent spectra reveal near-band-edge bound exciton absorption and Ga vacancy to oxygen vacancy defect level transitions, respectively. The MgGaO MSM detectors also show very good responsivity and current-time characteristics. This study indicates that UWBG MgGaO semiconductors have a promising potential for deep-UV photodetection applications.

2.5 References

[1] N. H. Tran, B. H. Le, S. Zhao, Z. Mi, *Appl. Phys. Lett.* **2017**, *110*, 032102.

[2] M. Kim, J.-H. Seo, U. Singisetti, Z. Ma, *J. Mater. Chem. C* **2017**, *5*, 8338.

[3] C. Xie, X.-T. Lu, X.-W. Tong, Z.-X. Zhang, F.-X. Liang, L. Liang, L.-B. Luo, Y.-C. Wu, *Advanced Functional Materials* **2019**, *29*, 1806006.

[4] J. Y. Tsao, S. Chowdhury, M. A. Hollis, D. Jena, N. M. Johnson, K. A. Jones, R. J. Kaplar, S. Rajan, C. G. Van de Walle, E. Bellotti, C. L. Chua, R. Collazo, M. E. Coltrin, J. A. Cooper, K. R. Evans, S. Graham, T. A. Grotjohn, E. R. Heller, M. Higashiwaki, M. S. Islam, P. W. Juodawlkis, M. A. Khan, A. D. Koehler, J. H. Leach, U. K. Mishra, R. J. Nemanich, R. C. N. Pilawa-Podgurski, J. B. Shealy, Z. Sitar, M. J. Tadjer, A. F. Witulski, M. Wraback, J. A. Simmons, *Advanced Electronic Materials* **2018**, *4*, 1600501.

[5] E. Monroy, F. Omn s, F. Calle, *Semicond. Sci. Technol.* **2003**, *18*, R33.

[6] S. J. Pearton, J. Yang, P. H. Cary, F. Ren, J. Kim, M. J. Tadjer, M. A. Mastro, *Applied Physics Reviews* **2018**, *5*, 011301.

[7] X. Xia, Y. Chen, Q. Feng, H. Liang, P. Tao, M. Xu, G. Du, *Appl. Phys. Lett.* **2016**, *108*, 202103.

[8] S. Rafique, L. Han, H. Zhao, *physica status solidi (a)* **2016**, *213*, 1002.

[9] S. Sharma, K. Zeng, S. Saha, U. Singisetti, *IEEE Electron Device Letters* **2020**, *41*, 836.

[10] K. Zeng, A. Vaidya, U. Singisetti, *IEEE Electron Device Letters* **2018**, *39*, 1385.

[11] J. Yang, S. Ahn, F. Ren, S. J. Pearton, S. Jang, A. Kuramata, *IEEE Electron Device Letters* **2017**, *38*, 906.

[12] B. Zhao, F. Wang, H. Chen, L. Zheng, L. Su, D. Zhao, X. Fang, *Advanced Functional Materials* **2017**, *27*, 1700264.

[13] A. Kumar, A. Bag, *Nanotechnology* **2020**, *31*, 304001.

[14] Y. Qin, L. Li, X. Zhao, G. S. Tompa, H. Dong, G. Jian, Q. He, P. Tan, X. Hou, Z. Zhang, S. Yu, H. Sun, G. Xu, X. Miao, K. Xue, S. Long, M. Liu, *ACS Photonics* **2020**, *7*, 812.

[15] S. Oh, C.-K. Kim, J. Kim, *ACS Photonics* **2018**, *5*, 1123.

[16] M. Baldini, M. Albrecht, A. Fiedler, K. Irmscher, R. Schewski, G. Wagner, *ECS J. Solid State Sci. Technol.* **2017**, *6*, Q3040.

[17] N. K. Kalarickal, Z. Xia, J. McGlone, S. Krishnamoorthy, W. Moore, M. Brenner, A. R. Arehart, S. A. Ringel, S. Rajan, *Appl. Phys. Lett.* **2019**, *115*, 152106.

[18] N. Suzuki, S. Ohira, M. Tanaka, T. Sugawara, K. Nakajima, T. Shishido, *physica status solidi c* **2007**, *4*, 2310.

[19] E. Ahmadi, O. S. Koksaldi, S. W. Kaun, Y. Oshima, D. B. Short, U. K. Mishra, J. S. Speck, *Appl. Phys. Express* **2017**, *10*, 041102.

[20] N. Moser, J. McCandless, A. Crespo, K. Leedy, A. Green, A. Neal, S. Mou, E. Ahmadi, J. Speck, K. Chabak, N. Peixoto, G. Jessen, *IEEE Electron Device Letters* **2017**, *38*, 775.

[21] E. Farzana, A. Mauze, J. B. Varley, T. E. Blue, J. S. Speck, A. R. Arehart, S. A. Ringel, *APL Materials* **2019**, *7*, 121102.

[22] J. Yan, C. Qu, *J. Semicond.* **2016**, *37*, 042002.

[23] Y. Wang, J. Su, H. Yuan, Z. Lin, J. Zhang, Y. Hao, J. Chang, *Semicond. Sci. Technol.* **2021**, *36*, 095026.

[24] Y. Chen, Y. Lu, X. Yang, S. Li, K. Li, X. Chen, Z. Xu, J. Zang, C. Shan, *Materials Today Physics* **2021**, *18*, 100369.

[25] A. Kyrtsos, M. Matsubara, E. Bellotti, *Appl. Phys. Lett.* **2018**, *112*, 032108.

[26] M. H. Wong, C.-H. Lin, A. Kuramata, S. Yamakoshi, H. Murakami, Y. Kumagai, M. Higashiwaki, *Appl. Phys. Lett.* **2018**, *113*, 102103.

[27] Y. P. Qian, D. Y. Guo, X. L. Chu, H. Z. Shi, W. K. Zhu, K. Wang, X. K. Huang, H. Wang, S. L. Wang, P. G. Li, X. H. Zhang, W. H. Tang, *Materials Letters* **2017**, *209*, 558.

[28] F. Alema, B. Hertog, O. Ledyaev, D. Volovik, G. Thoma, R. Miller, A. Osinsky, P. Mukhopadhyay, S. Bakhshi, H. Ali, W. V. Schoenfeld, *physica status solidi (a)* **2017**, *214*, 1600688.

[29] L. Li, F. Liao, X. Hu, *Superlattices and Microstructures* **2020**, *141*, 106502.

[30] Z. Galazka, *Semiconductor Science and Technology* **2018**, *33*, 113001.

[31] R. Miller, F. Alema, A. Osinsky, *IEEE Transactions on Semiconductor Manufacturing* **2018**, *31*, 467.

[32] A. F. M. A. U. Bhuiyan, Z. Feng, J. M. Johnson, H.-L. Huang, J. Hwang, H. Zhao, *Appl. Phys. Lett.* **2020**, *117*, 142107.

[33] W. Hu, S. Li, Y. Hu, L. Wan, S. Jiao, W. Hu, D. N. Talwar, Z. C. Feng, T. Li, J. Xu, L. Wei, W. Guo, *Journal of Alloys and Compounds* **2021**, *864*, 158765.

[34] Y.-S. Shen, W.-K. Wang, R.-H. Horng, *IEEE Journal of the Electron Devices Society* **2017**, *5*, 112.

[35] L. Wang, X. Han, **2019**, 2.

[36] M. Dong, W. Zheng, C. Xu, R. Lin, D. Zhang, Z. Zhang, F. Huang, *Advanced Optical Materials* **2019**, *7*, 1801272.

[37] C. Xu, Z. Du, Y. Huang, M. Dong, R. Lin, Y. Li, B. Wang, W. Zheng, F. Huang, *ACS Appl. Mater. Interfaces* **2019**, *11*, 9641.

[38] X. Bi, Z. Wu, Y. Huang, W. Tang, *AIP Advances* **2018**, *8*, 025008.

[39] S. Rafique, L. Han, H. Zhao, *ECS Trans.* **2017**, *80*, 203.

[40] T. Onuma, S. Fujioka, T. Yamaguchi, Y. Itoh, M. Higashiwaki, K. Sasaki, T. Masui, T. Honda, *Journal of Crystal Growth* **2014**, *401*, 330.

[41] C. Kranert, C. Sturm, R. Schmidt-Grund, M. Grundmann, *Sci Rep* **2016**, *6*, 35964.
[42] T. D. K. Wungu, M. Sakaue, S. M. Aspera, T. L. P. Thuy, M. Alaydrus, H. Kasai, T. Ishihara, *ECS Trans.* **2013**, *57*, 2715.

[43] S. Geller, *J. Chem. Phys.* **1960**, *33*, 676.

[44] Z. Zhang, Z. Ding, X. Guo, Z. Luo, J. Wei, C. Yang, Y. Huang, Z. Li, *Mater. Res. Express* **2019**, *6*, 105920.

[45] X. Ma, Y. Zhang, L. Dong, R. Jia, *Results in Physics* **2017**, *7*, 1582.

[46] K. Zhang, Z. Xu, S. Zhang, H. Wang, H. Cheng, J. Hao, J. Wu, F. Fang, *Physica B: Condensed Matter* **2021**, *600*, 412624.

[47] J. Wei, K. Kim, F. Liu, P. Wang, X. Zheng, Z. Chen, D. Wang, A. Imran, X. Rong, X. Yang, F. Xu, J. Yang, B. Shen, X. Wang, *J. Semicond.* **2019**, *40*, 012802.

[48] Z. Chen, K. Ge, D. Meng, X. Chen, *Materials Letters* **2022**, *320*, 132385.

[49] T. Oshima, T. Okuno, S. Fujita, *Jpn. J. Appl. Phys.* **2007**, *46*, 7217.

[50] T. Onuma, S. Saito, K. Sasaki, T. Masui, T. Yamaguchi, T. Honda, M. Higashiwaki, *Jpn. J. Appl. Phys.* **2015**, *54*, 112601.

[51] A. Singh Pratiyush, S. Krishnamoorthy, S. Vishnu Solanke, Z. Xia, R. Muralidharan, S. Rajan, D. N. Nath, *Appl. Phys. Lett.* **2017**, *110*, 221107.

[52] J. Yao, Z. Deng, Z. Zheng, G. Yang, *ACS Appl. Mater. Interfaces* **2016**, *8*, 20872.

[53] J. D. Yao, J. M. Shao, G. W. Yang, *Sci Rep* **2015**, *5*, 12320.

[54] C. Chang, H.-H. Cheng, G. A. Sevison, J. R. Hendrickson, Z. Li, I. Agha, J. Mathews, R. A. Soref, G. Sun, *Materials* **2022**, *15*, 989.

[55] Y. Ishitani, *Journal of Applied Physics* **1999**, *86*, 6816.

[56] S. Yamaoka, Y. Mikuni, M. Nakayama, *J. Phys. Soc. Jpn.* **2019**, *88*, 113701.

[57] A. S. Pratiyush, S. Krishnamoorthy, S. V. Solanke, Z. Xia, R. Muralidharan, S. Rajan, D. N. Nath, **n.d.**

[58] Review of deep ultraviolet photodetector based on gallium oxide - IOPscience, https://iopscience.iop.org/article/10.1088/1674-1056/28/1/018501/meta, accessed: Feb., 2023.

[59] Q. Feng, L. Huang, G. Han, F. Li, X. Li, L. Fang, X. Xing, J. Zhang, W. Mu, Z. Jia, D. Guo, W. Tang, X. Tao, Y. Hao, *IEEE Transactions on Electron Devices* **2016**, *63*, 3578.

[60] X. Zhu, Y.-W. Zhang, S.-N. Zhang, X.-Q. Huo, X.-H. Zhang, Z.-Q. Li, *Journal of Luminescence* **2022**, *246*, 118801.

[61] W. Mi, C. Luan, Z. Li, C. Zhao, X. Feng, J. Ma, *Optical Materials* **2013**, *35*, 2624.

[62] K. Zhang, Z. Xu, J. Zhao, H. Wang, J. Hao, S. Zhang, H. Cheng, B. Dong, *Journal of Alloys and Compounds* **2021**, *881*, 160665.

[63] Y. Qin, S. Long, H. Dong, Q. He, G. Jian, Y. Zhang, X. Hou, P. Tan, Z. Zhang, H. Lv, Q. Liu, M. Liu, *Chinese Phys. B* **2019**, *28*, 018501.

[64] K. Ling, K. Li, R. Bai, B. Zhao, X. Liu, *Materials Science in Semiconductor Processing* **2022**, *152*, 107096.

[65] F. Xie, F. Xie, F. Xie, Y. Gu, Y. Gu, Z. Hu, B. Yu, G. Yang, G. Yang, *Opt. Express, OE* **2022**, *30*, 23756.

[66] Q. Hou, K. Liu, X. Chen, J. Yang, Q. Ai, Z. Cheng, Y. Zhu, B. Li, L. Liu, D. Shen, *physica status solidi (RRL) – Rapid Research Letters* **2022**, *16*, 2200137.

[67] X. Z. Liu, P. Guo, T. Sheng, L. X. Qian, W. L. Zhang, Y. R. Li, *Optical Materials* **2016**, *51*, 203.

Supporting Information

1. MBE growth conditions and parameters of Ga_2O_3 and MgGaO ternary alloy thin films of sample A, B and C

Table S2.1 Growth conditions and Ga_2O_3 and MgGaO ternary alloy thin films parameters with different Mg compositions.

Sample	Pre-growth annealing conditions	Growth Conditions					Post-growth annealing conditions	Thickness (nm)	Roughness (nm)	XPS Mg atomic percent	Bandgap (eV)
		Substrate (˚C)	Ga (˚C)	Mg (˚C)	O_2 flux (sccm)	Time (h)					
Ga_2O_3	800 ˚C 20 minutes	650	750	-	2.5	2	700 ˚C 20 minutes	205.16	1.29	-	5.03
Sample A		650	750	380	2.5	1		83.08	0.45	1.8%	5.09
Sample B		650	750	385	2.5	1		92.90	0.68	3.4%	5.15
Sample C		650	750	390	2.5	1		93.18	0.80	4.0%	5.22

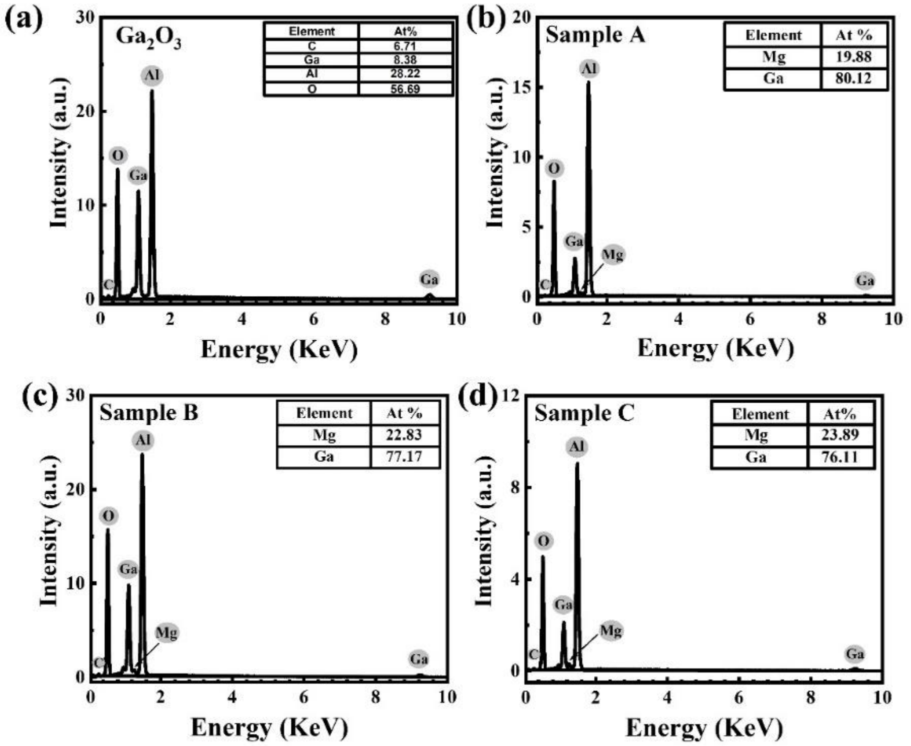

Figure S2.1 (a)–(d) EDS spectra of Ga_2O_3, MgGaO thin film samples A, B, and C, respectively. Mg and Ga compositions shown as illustrations in each figure are only relative percentages among cation Mg and Ga only. After excluding the signals from the substrates and including oxygen signals from the films, Mg compositions are calibrated to be 0, 1.23%, 2.59%, and 3.03%, for Ga_2O_3 and MgGaO samples, respectively. These numbers are in reasonable agreement with the XPS data.

2. Phonon modes of *β*-MgGaO and Ga_2O_3 thin films

Table S2.2 Phonon wave numbers in β-MgGaO and β-Ga_2O_3 thin films obtained by Raman spectroscopy at room temperature. Previously reported experimental and theoretical values are also shown for comparison.

Raman Mode	This work (Unit: cm^{-1})				Experiment (Unit: cm^{-1})			Theory (Unit: cm^{-1})		
	β-Ga_2O_3	β-MgGaO								
		Sample A	Sample B	Sample C	Exp.1[1]	Exp.2[2]	Exp.3[3,4]	T1[1]	T2[2,4]	T3[5]
$A_g^{(1)}$	107.8	106.4	107.4	106.5	110.2	111	112	104	113	104.7
$B_g^{(1)}$	115.8	115.4	115.8	115.4	113.6	114	115	113	114	112.1
$B_g^{(2)}$	146.8	138.9	139.3	138.8	144.7	147	149	149	152	141.3
$A_g^{(2)}$	169.6	-	-	-	169.2	169	173	165	166	163.5
$A_g^{(3)}$	201.5	-	-	-	200.4	199	205	205	195	202.3
$A_g^{(4)}$	-	-	-	-	318.6	318	322	317	308	315.8
$A_g^{(5)}$	342.7	344.2	340.2	-	346.4	346	3350	346	353	339.7
$B_g^{(3)}$	353	-	-	-	-	353	355	356	360	348.3
$A_g^{(6)}$	-	-	-	-	415.7	415	421	418	406	420.2
$A_g^{(7)}$	-	-	-	-	-	475	479	467	468	459.4
$B_g^{(4)}$	-	-	-	481	473.5	475	480	474	474	472.8
$A_g^{(8)}$	-	-	-	-	628.7	628	635	600	628	607.1
$B_g^{(5)}$	645	644.8	644.5	643	652.5	651	659	626	644	627.1
$A_g^{(9)}$	-	-	-	-	-	657	663	637	654	656.1
$A_g^{(10)}$	750	749.2	749.9	749	763.9	763	772	732	760	757.1

3. Schematic of *β*-MgGaO structure

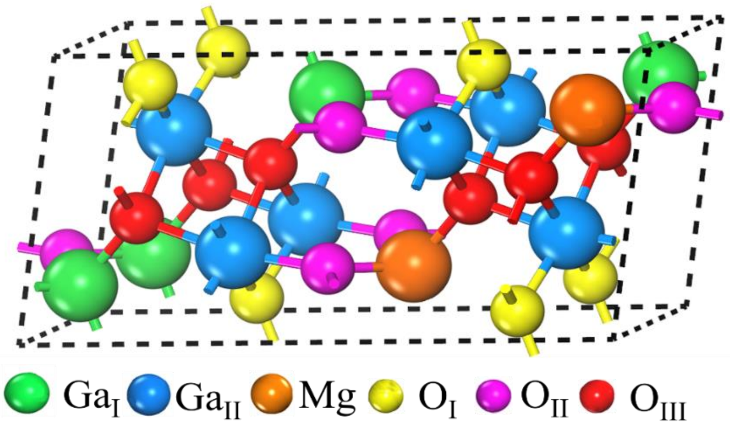

Figure S2.2 Illustration of monoclinic MgGaO structure.

4. References

[1] D. Machon, P. F. McMillan, B. Xu, J. Dong, *Phys. Rev. B* **2006**, *73*, 094125.

[2] D. Dohy, G. Lucazeau, A. Revcolevschi, *J. Solid State Chem.* **1982**, *45*, 180.

[3] T. Onuma, S. Fujioka, T. Yamaguchi, Y. Itoh, M. Higashiwaki, K. Sasaki, T. Masui, T. Honda, *J. Cryst. Growth* **2014**, *401*, 330.

[4] C. Kranert, C. Sturm, R. Schmidt-Grund, M. Grundmann, *Sci. Rep.* **2016**, *6*, 35964.

[5] B. Liu, M. Gu, X. Liu, *Appl. Phys. Lett.* **2007**, *91*, 172102.

Chapter 3: Investigation of phase transition and ultra-wide bandgap engineering in MgGaO semiconductor thin films

3.1 Introduction

Nowadays, wide bandgap semiconductor materials such as gallium nitride (GaN) and silicon carbide (SiC) have been applied in many military and civilian fields, such as power electronics and deep ultraviolet (UV) optoelectronics.[1–5] To further enhance the performance in these areas, ultra-wide bandgap (UWBG) semiconductors with the bandgap energies larger than those of GaN and SiC are desirable. As a promising candidate of UWBG semiconductors, β-Ga_2O_3 with large direct bandgap of ~4.9 eV has been extensively studied due to its high physical and chemical stability, high critical electric field strength of ~8 MV/cm, and high figure-of-merit (FOM).[6] Therefore, it has been widely used in power electronic and optoelectronic devices such as solar-blind UV photodetectors,[7–10] gas sensors,[11,12] and field effect transistors.[13–15] For broader and more extensive application of β-Ga_2O_3, bandgap engineering is highly desired. The tunable bandgap paves the way for designing and optimizing electronic and optoelectronic devices in more flexibility and higher performance. Besides bandgap tuning by modulating crystalline disorder of Ga_2O_3 itself,[16] bandgap-lowering candidates such as InGaO[17–21] with bandgap ranging from ~3.88 to ~5.0 eV and ZnGaO[22–24] with bandgap ranging from ~4.7 to ~5.1 eV have been widely used for solar-blind photodetector[25,26] and thin film transistor[27,28] already. On the other hand, as one of the bandgap-increasing candidates, AlGaO[21,29–31] with bandgap ranging from 4.85 to 7.1 eV has been extensively studied as well. As an alternatively viable bandgap-increasing candidate, β-MgGaO single crystalline thin films with bandgap tuning up to ~5.22 eV were grown recently and properties of their metal-semiconductor-metal (MSM) photodetectors were investigated.[32] MgGaO can be construed as a mixture of Ga_2O_3 and MgO materials, thus its bandgap may be tuned between ~4.9 and ~7.8 eV.[32,33] However, the phase transition conditions to transform the crystal structure from β phase to mixed phase and finally to rocksalt phase for MgGaO alloy system with increasingly incorporated Mg is still not clear. The structural and optical properties of the films in different phases remain unknown. Thus, revealing phase transition condition with bandgap tuning of MgGaO thin films is of great significance for next-generation Ga_2O_3 based electronics and optoelectronics.

In this chapter, twenty MgGaO thin film samples with relative Mg/Ga atomic percent ranging from 0 at.%/100 at.% to 100 at.%/ 0 at.% were grown by plasma-assisted molecular beam epitaxy (MBE). Structure transformation, film quality, lattice parameters, surface morphology, optical bandgap properties, and epitaxy relationship between MgGaO films and c-sapphire substrate evolving with the Mg atomic percent were revealed, which provides a promising potential for devices applications by using high-quality bandgap tunable MgGaO thin films in the future.

3.2 Experimental Details

3.2.1 Film growth

MgGaO thin films were grown on two-inch c-sapphire substrates by using an RF oxygen plasma assisted molecular beam epitaxy (MBE) system (SVT Associates, Inc.). The substrates were cleaned with Piranha solution (H_2O_2: H_2SO_4 = 3: 5) at 200 °C for 20 minutes and rinsed by deionized water, after dried by nitrogen gas, they were transferred to the loadlock chamber immediately. High-purity elemental Mg (4N) and Ga shots (6N) (Alfa Aesar) were used for sample growth. An 800 ˚C pre-growth annealing process was performed for 20 minutes to achieve an atomic level surface at a high vacuum of 10^{-9} torr. The sample growth temperature was kept at 650 ˚C for 2h with a 2.5 sccm flux of oxygen under a 400 W RF plasma. The Ga temperature was fixed at 750 ˚C, by changing the Mg temperature from 390 ˚C to 460 ˚C, 20 MgGaO thin film samples at various Mg atomic percent were grown, followed by a post-growth annealing process at 700 ˚C under oxygen atmosphere for 20 minutes.

3.2.2 Film characterization

Film thickness of the samples was measured by a Filmetrics 3D Profilometer. Surface morphologies of films were characterized by a Dimension 5000 Nanoman atomic force microscope. Mg and Ga relative atomic percent for all samples were measured by EDX in a TESCAN Vega3 SBH scanning electron microscope instrument, and Mg, Ga, and O relative atomic percent of several selected samples in different phases were measured by a Kratos AXIS Ultra DLD X-ray photoelectron spectroscope. RHEED characterizations were done in ultra-high vacuum using an electron beam with 15 keV energy. XRD theta-2theta, rocking curve, φ-scans and RSM measurements were used to characterize the sample structure, film quality, epitaxial relationship and lattice parameters by using a Bruker D8 Advance X-ray diffractometer and a Rigaku SmartLab X-ray diffractometer with Cu Kα (λ = 0.15405 nm) radiation at room temperature. The phonon spectra of the films were investigated by a confocal Raman microscope equipped with a high-resolution laser with a wavelength of 532 nm and a power of 60 mW (LabRAM HR, HORIBA

Scientific). Room temperature absorption and transmittance spectra of the samples were measured using a high-performance UV-Vis-NIR spectrophotometer (Cary 5000, Agilent Inc.).

3.3 Results and Discussion

3.3.1 Sample growth and film element composition characterizations

Table 3.1 Characterized parameters of 20 MgGaO thin films with Mg at.% from 0% to 100%.

Sample index	Film thickness (nm)	Relative atomic percent (EDX)		Relative atomic percent (XPS)			Phase identification	Chemical formula	Surface roughness (nm)	Bandgap (eV)
		Mg%	Ga%	Mg%	Ga%	O%				
#01	117.54	0	100	0	35.6	64.4	β-phase	Ga_2O_3	1.544	5.03
#02	122.17	3.86	96.14	-	-	-		$(Mg_xGa_{1-x})_2O_3$	2.058	5.04
#03	130.71	7.09	92.91	1.5	27.8	70.7			0.140	5.06
#04	131.47	10.11	89.89	-	-	-			0.260	5.08
#05	169.76	19.44	80.56	5.1	26.1	68.8			18.93	5.10
#06	188.67	19.81	80.19	-	-	-			21.14	5.14
#07	295.41	30.23	69.77	-	-	-			9.731	5.36
#08	347.54	37.35	62.65	-	-		Mixed phase	$Mg_xGa_yO_z$	6.786	5.53
#09	354.29	40.8	59.2	-	-				7.335	5.58
#10	363.96	42.89	57.11	10.6	15.1	74.3			6.526	5.61
#11	365.71	45.62	54.38	-	-	-			9.223	5.63
#12	393.20	48.39	51.61	-	-	-			6.731	5.65
#13	399.65	51.09	48.91	-	-	-			5.684	5.67
#14	406.32	54.71	45.29	-	-	-			9.460	5.69
#15	426.48	56.87	43.13	-	-	-			7.304	5.73
#16	494.03	61.97	38.03	-	-	-			9.916	5.76
#17	520.15	63.88	36.12	20.7	12.5	66.8			9.339	5.78
#18	566.19	72.84	27.16	31.4	4.5	64.1	Rocksalt	$Mg_xGa_{1-x}O$	32.75	5.81
#19	750.69	78.69	21.31	-	-	-			6.261	5.89
#20	189.19	100	0	42.5	0	57.4		MgO	1.013	-

Sample growth procedures and characterization methodologies are given in detail in the experimental section. **Table 3.1** lists the characterized parameters of MgGaO samples with Mg atomic percentage ranging from 0% to 100%. The film thickness for β-Ga_2O_3 is 117.54

nm, for rocksalt MgO is 189.19 nm, and the thickness of MgGaO films increases from 122.17 to 750.69 nm monotonically as the Mg composition increases. **Figure 3.1(a)** shows energy-dispersive X-ray spectra (EDX) of all samples. O kα, Ga Lα, Mg Kα, and Al Kα are located around 0.525, 1.098, 1.253, and 1.486 KeV, respectively. Al signal is from the substrate. With more Mg incorporated in, the relative peak intensity for Ga to Mg decreases, the Al peak intensity gradually becomes smaller due to the increasing film thickness. The relative atomic percent of Mg and Ga is listed in **Table 3.1**. X-ray photoelectron spectroscopy (XPS) analysis was also carried out to calibrate the elemental compositions of a few selected samples, including sample #01, #03, and #05 in β phase, #10 and #17 in mixed phase, #18 and #20 in rocksalt phase. **Figure 3.1(b)** shows XPS survey peaks of Ga 2p, Mg 2s, 2p and O 1s spectra, respectively. The spectra were and calibrated with the C 1s level of 284.8 eV. Because of limited penetration depth of x-rays

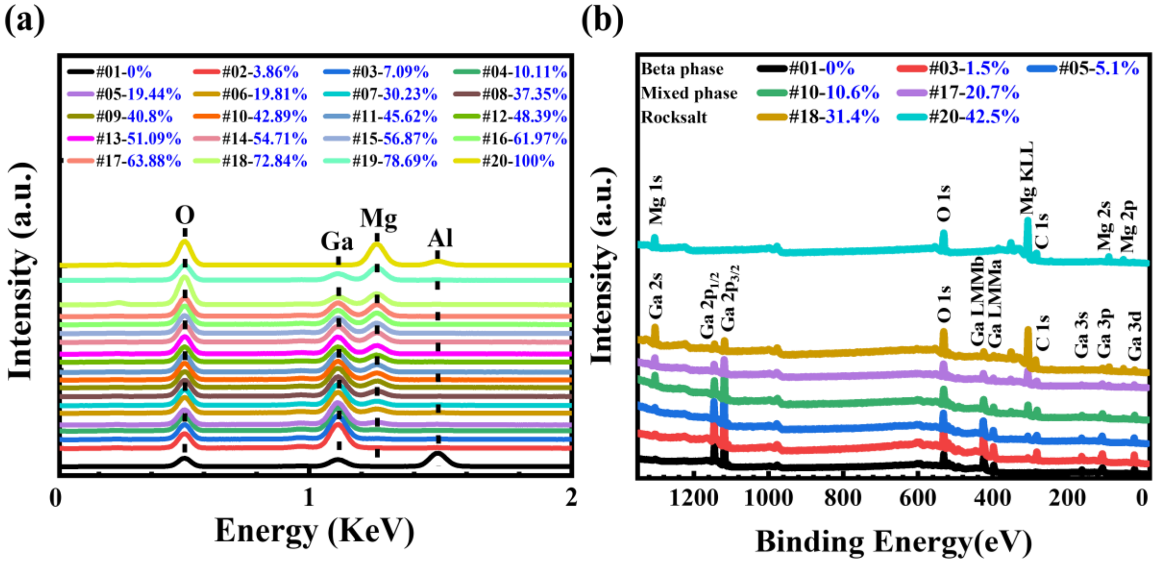

Figure 3.1 (a) EDX spectra of MgGaO ternary alloy thin films with Mg atomic percent ranging from 0 % to 100 %. (b) XPS survey spectra of sample #01, #03, #05, #10, #17, #18, and #20.

negligible photoelectrons exited from the substrate, no Al and oxygen signals from the substrate are detected in the spectra. Characteristic XPS peaks are zoomed-in and provided in Supporting Information, as seen from **Figure S3.1**, Ga $2p_{3/2}$ and Ga $2p_{1/2}$ are located at ~1116.4 and ~1143.2 eV, respectively (**Figure S3.1(a)**), Mg 2s, 2p are located at ~88.7 and ~49.78 eV, respectively (**Figure S3.1(b)**), and O 1s is located at ~531 eV (**Figure S3.1(c)**). Based on these peaks, the relative atomic percent of Mg, Ga and O of these selected samples is estimated and summarized in **Table 3.1**. The Mg at.% of these 7 samples are 0 at.%, 1.5 at.%, 5.1 at.%, 10.6 at.%, 20.7 at.%, 31.4 at.% and 42.5 at.%, respectively. As seen in **Table 3.1**, these values are different with those obtained from EDX because XPS provides survey of all three elements Mg, Ga, and O of the thin films while oxygen signals were excluded in the estimation of relative content of Mg and Ga in EDX experiment due to inevitable oxygen contribution from the substrate. **Figure 3.2(a)-(g)** show O 1s core level spectra of these samples, in which Shirley background was added.[34] O 1s core level spectra of these samples were de-convoluted into several fitting peaks located at ~530.0, ~530.84, ~531.80 and ~532.5 eV, which correspond to the binding energies of Mg-O bond,[35] Ga-O bond,[35] carbonate groups (CO_3^{2-}) due to absorbed carbon dioxide from atmosphere,[36,37] and surface hydroxide (OH^-),[38–40] respectively. **Figure 3.2(h)** shows Mg-O/Ga-O bond peak area ratio as a function of the Mg atomic percent. Mg-O/Ga-O bond ratio increases monotonically with Mg atomic percent, indicating that more Mg-O rather than Ga-O bonds are formed in the samples with more incorporated Mg. Besides EDX and XPS, Raman spectroscopy was also carried out as a supplementary method to confirm the Mg incorporation. **Figure S3.2** in Supporting Information shows Raman spectra of the samples.

Compared to Ga_2O_3 (sample #01), optical phonon modes $A_g^{(2)-(3)}$, $A_g^{(5)}$ and $B_g^{(4)-(5)}$ of MgGaO samples change. Reduced $A_g^{(2)-(3)}$ peak intensity implies the vibration and translation of the Ga_IO_4 tetrahedral chains, reduced $A_g^{(5)}$ and enhanced $B_g^{(4)}$ modes indicate the deformation of the $Ga_{II}O_6$ octahedral chains and the translation of the Ga_IO_4 tetrahedral chains, and smaller wavenumber of $B_g^{(5)}$ mode means the stretching and bending of Ga_IO_4 tetrahedral chains.[32,41]

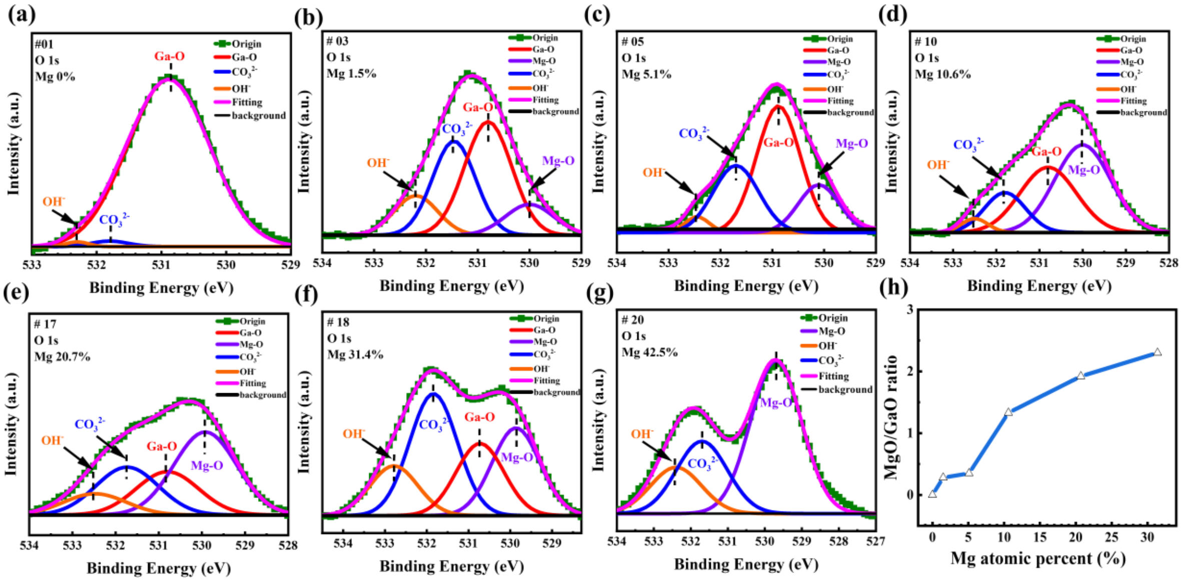

Figure 3.2 XPS spectra of O1s core level spectra of MgGaO films with various Mg atomic percent (a) 0%, (b) 1.5%, (c) 5.1%, (d) 10.6%, (e) 20.7%, (f) 31.4%, and (g) 42.5%. (h) Mg-O to Ga-O bond ratio versus Mg atomic percent.

3.3.2 Film structure characterizations

Figure 3.3(a) illustrates a schematic of MgGaO film in both β and rocksalt phases grown on c-sapphire. The vertical growth orientation is $<\bar{2}01>_{\beta\text{-phase}} \parallel <0001>_{\text{C-sapphire}}$ and $<111>_{\text{rocksalt}} \parallel <0001>_{\text{C-sapphire}}$, respectively. **Figure 3.3(b)** shows XRD pattern in θ/2θ scan mode of all MgGaO samples. For Mg at.% ranging from 0% to 30.23%, MgGaO samples are in β phase, four typical diffraction peaks located at ~19.12 °, 38.50 °, 59.14 °

and 82.37° correspond to the β phases of $(\bar{2}01)$, $(\bar{4}02)$, $(\bar{6}03)$, and $(\bar{8}04)$, respectively, implying a clear monoclinic structure. In these β-phase MgGaO samples, di-valent Mg substitute tri-valent Ga sites,[32] thus the chemical formula can be written as $(Mg_xGa_{1-x})_2O_3$ (**Table 3.1**). For example, the chemical formula of sample #02 is $(Mg_{0.0386}Ga_{0.9614})_2O_3$, or roughly $(Mg_{0.04}Ga_{0.96})_2O_3$. With more Mg incorporated in MgGaO samples, the diffraction angles exhibit an obvious decrease due to larger Mg ionic radius (0.72 Å) than Ga (0.62 Å). For Mg at.% ranging from 72.84% to 100%, MgGaO samples are in pure rocksalt phase, two typical diffraction peaks located at ~ 36.9° and 78.5° correspond to rocksalt phase of (111) and (222), respectively.[42] In these rocksalt MgGaO samples, Ga atom is assumed to substitute Mg atom site in the lattice, thus the chemical formula may be written as $Mg_xGa_{1-x}O$. Taking sample #18 for example, the chemical formula is $Mg_{0.7284}Ga_{0.2716}O$, or roughly $Mg_{0.73}Ga_{0.27}O$. For Mg at.% ranging from 37.35% to 63.88%, MgGaO samples are in mixed phase since $(\bar{4}02)$ of β phase, and (111) and (222) of rocksalt phase coexist in the XRD pattern. Due to the mixed phase nature of the film in this region, the preferred way to write the chemical formula is in a form of $Mg_xGa_yO_z$, where x, y, z are the relative atomic percent among Mg, Ga, and O elements. Taking sample #10 as an example, the chemical formula is $Mg_{0.314}Ga_{0.045}O_{0.641}$, or roughly $Mg_{0.31}Ga_{0.05}O_{0.64}$. Based on the θ/2θ scan results, β-MgGaO and rocksalt MgGaO grown on c-sapphire {0001} plane is highly $\{\bar{2}01\}$ and {111} oriented, respectively. In addition, no MgGaO thin films in the β and rocksalt mixed phase regime exhibit spinel phase as existed in $MgGa_2O_4$, $MgAl_2O_4$, and other spinel oxides, which shall originate from the present growth on c-plane sapphire.

The growth of spinel MgGaO may be achieved on r-plane sapphire, which needs further studies. **Figure 3.3(c)** shows normalized XRD rocking curves of selected 12 samples among three phase regions. The full width at half maximum (FWHM) of sample #01-#07 in β phase are 0.0831˚, 0.0792˚, 0.0789˚, 0.0716˚, 0.0919˚, 0.0796˚ and 0.0793˚, sample #09-#10, #16 in mixed phase are 0.0933˚, 0.1000˚, 0.0960˚, and sample #18, #20 in rocksalt phase is 0.0988˚ and 0.5014˚, respectively. These very small FWHM values suggest that our β phase films are of very high quality.[43]

To reveal how the lattice parameters of MgGaO thin films change with Mg atomic percent, besides θ/2θ scan, in-plane reciprocal space mapping (RSM) was measured for films in both β phase and rocksalt phase. As for monoclinic structure of Ga_2O_3, the

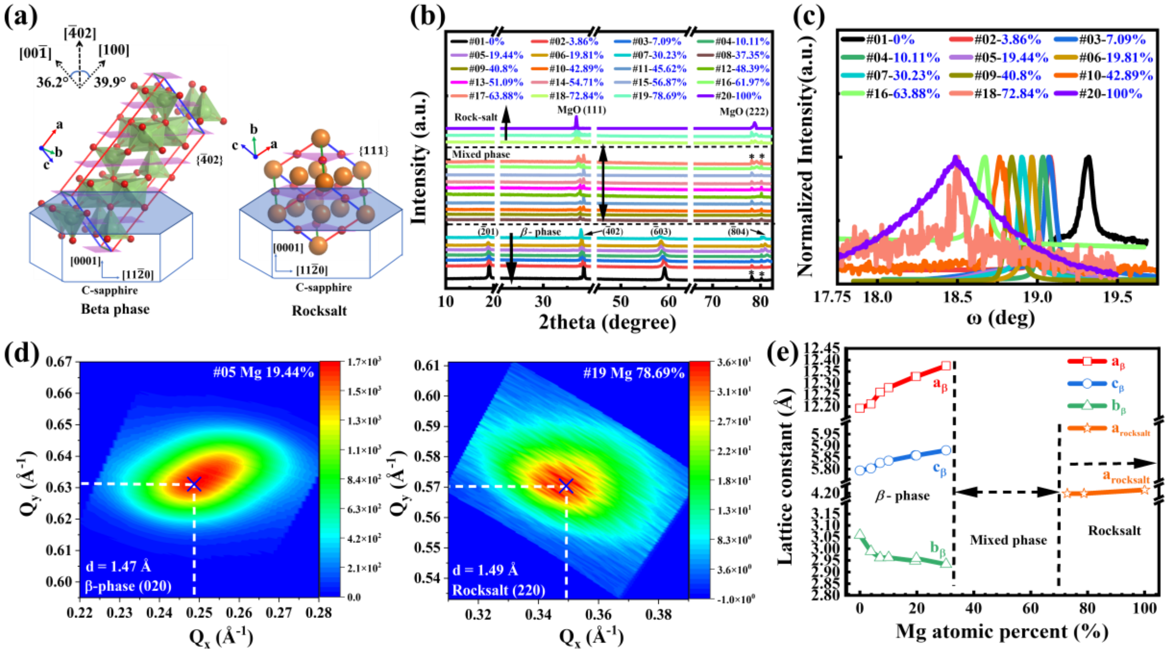

Figure 3.3 (a) Schematic of MgGaO film in both β and rocksalt phases grown on c-sapphire, (b) XRD pattern of MgGaO films with various Mg atomic percent in *θ*/2*θ* scan mode, (c) XRD rocking curves of selected MgGaO thin films, (d) in-plane reciprocal space mappings for sample #05 of β phase of (020) and sample #19 of rocksalt phase of (220), (e) β phase lattice constant a_β, b_β, c_β and rocksalt phase lattice constant $a_{rocksalt}$ versus Mg atomic percent.

reference lattice constant a_β, b_β, c_β, β angle between a and c axis, and $d_{(\bar{4}02)}$ is ~12.020 Å, ~3.04 Å, ~5.799 Å, 103.7°, and 2.34 Å, respectively. Assuming the monoclinic structure is stable after Mg is incorporated, as shown in **Figure 3.3(a)**, the angle between orientation $[\bar{4}02]$ and $[00\bar{1}]$, and between orientation $[\bar{4}02]$ and [100], can be calculated as ~36.2° and ~39.9°, respectively. Therefore, the lattice constant a_β and c_β can be calculated as follows:

$$a_\beta = 4 * \frac{d_{(\bar{4}02)}}{\cos{(39.9^\circ)}} \tag{1}$$

$$c_\beta = 2 * \frac{d_{(\bar{4}02)}}{\cos{(36.2^\circ)}} \tag{2}$$

According to Bragg's law, the β-phase $(\bar{4}02)$ interplanar distance $d_{(\bar{4}02)}$ can be estimated from θ/2θ scans. Based on the above equations, lattice constant a_β and c_β were calculated and listed in **Table S3.1** of Supporting Information. For pure rocksalt samples, interplanar distance $d_{(111)}$ can be estimated from θ/2θ scans and the lattice constant $a_{rocksalt}$ can be calculated as $\sqrt{3}d_{(111)}$, which is also listed in **Table S3.1** of Supporting Information, for example, it is ~4.2 Å for sample #20. As an alternative method to the θ/2θ scan for the estimation of the out-of-plane d-spacing, the out-of-plane RSM was measured (**Figure S3.3(a)-(g)**, Supporting Information). It shows that the calculated lattice constant values by two methods are almost the same (**Figure S3.3(h)**, Supporting Information). **Figure 3.3(d)** shows an example of in-plane reciprocal space mappings for (020) plane of β phase sample #05 and (220) plane of rocksalt phase sample #19, respectively. **Figure S3.4** in Supporting Information shows RSM for other samples. According to β-Ga_2O_3 PDF 01-087-1901, the reference d-spacing value of (020) plane is ~1.52 Å, the β phase lattice constant b_β is twice of $d_{(020)}$, which is ~3.04 Å. According to MgO PDF 00-004-0829, the reference d-spacing value of (220) plane in is ~1.48 Å, the rocksalt phase lattice constant $a_{rocksalt}$ is $2\sqrt{2}d_{(220)}$, which is ~4.2 Å. Based on these mathematical relationships, the lattice constants b_β and $a_{rocksalt}$ of respective MgGaO samples are calculated from the in-plane RSM data and listed in Table **S1** of Supporting Information. For rocksalt samples, the lattice constant values calculated from both θ/2θ and in-plane RSM scans are the same, indicating the cubic structure. **Figure 3.3(e)** shows the lattice constants as a function of Mg atomic percent. In β-phase MgGaO samples, the parameters a_β and c_β increase, while b_β decreases with the increase of Mg at.% compared to that of the reference sample β-Ga_2O_3. In rocksalt phase MgGaO samples, the lattice constant $a_{rocksalt}$ changes only slightly as Mg increases compared to that of the reference sample MgO.

To understand epitaxial relationship between MgGaO films and c-sapphire substrate, the reflection high energy electron diffraction (RHEED) was measured. **Figure 3.4(a)-(f)** show RHEED patterns of MgGaO thin films with Mg at.% of 0%, 7.09%, 10.11% in β phase, 42.89% in mixed phase, and 78.69%, and 100% in rocksalt phase, respectively. The

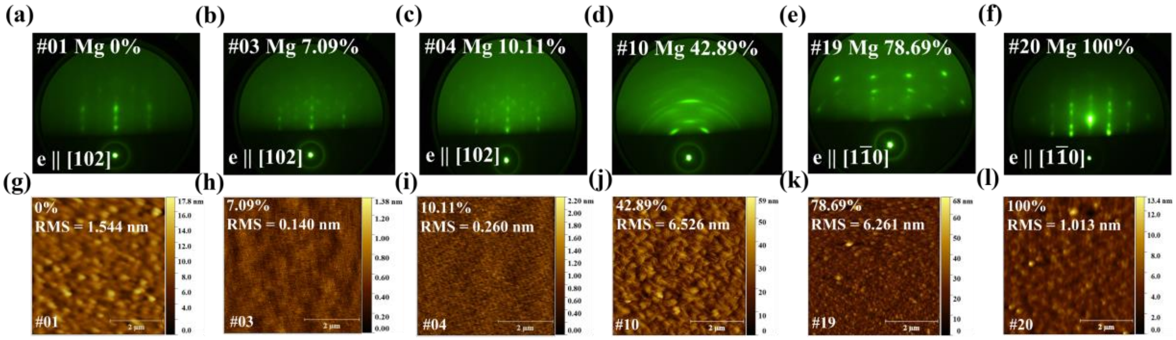

Figure 3.4 (a)-(f) RHEED patterns and (g)-(l) AFM images of MgGaO ternary alloy thin films at different Mg atomic percent 0%, 7.09%, 10.11%, 42.89%, 42.89%, and 100%, respectively.

streaky-like patterns of β-phase $\{\bar{2}01\}$ plane along [102] azimuth (**Figure 3.4(a)-(c)**) and along [010] azimuth (**Figure S3.5(a)-(c)**, Supporting Information) indicate high crystallinity of the films, which are similar to those RHEED patterns obtained from β-Ga_2O_3[44,45]. Based on the RHEED patterns, in-plane lattice constants $a_{||[102]}$ and $a_{||[010]}$, which are the distance between (010) planes and between (102) planes as illustrated in a schematic of the atom arrangement of $(\bar{2}01)$ surface (**Figure S3.6(a)** in the Supporting Information), were calculated as ~2.98 Å and 5.06 Å for sample #01, ~2.88 Å and 5.11 Å for sample #03, ~2.84 Å and 5.17 Å for sample #04, respectively. These numbers are analogous to ~3.04 Å and 4.96 Å of reported in-plane lattice constants of β-Ga_2O_3.[46] These surface lattice parameters can be used to estimate the lattice constants of the unit cell a_β, b_β, and c_β of these β-phase samples. First, b_β is equal to $a_{||[102]}$. Then, a schematic showing the side-view of the unit cell in **Figure S3.6(b)** of Supporting Information is used to calculate a_β and c_β. Since β-phase samples have a surface plane of $(\bar{2}01)$, the lateral length along [102] direction within the unit cell is generally expressed as K* $a_{||[010]}$, where K is a multiple and can only take integer or half-integer as can be inferred from surface atom arrangement on $(\bar{2}01)$ plane along [102] direction (designated as $(\bar{2}01)$[102]) in **Figure S3.6(a)** in Supporting Information. The projections of $a_\beta/2$ and c_β onto $<\bar{2}01>$ are equal while $K{*}a_{||[010]}$ equals the sum of projections of $a_\beta/2$ and c_β onto $(\bar{2}01)$[102]. These relationships can be written as follows:

$$\frac{a_\beta}{2} * cos(39.9^\circ) = c_\beta * \cos(36.2^\circ) \qquad (3)$$

$$\frac{a_\beta}{2} * sin(39.9^\circ) + c_\beta * sin(36.2^\circ) = K * a_{||[010]} \qquad (4)$$

According to equation (3), $c_{\beta} = a_{\beta} / 2.104$, which is compatible with the result of equation (1) / equation (2). After replacing c_{β} with a_{β} in equation (4), $a_{\beta} = 1.663 * K * a_{||[010]}$. Taking sample #01 as an example, $a_{||[010]}$ = 5.06 Å, only when K equals ~1.5, a_{β} and c_{β} can be calculated as 12.62 Å and 6 Å, which would be close to Ga_2O_3 reference lattice constant. With this method, the lattice constant values of these samples are calculated and listed in **Table S3.2** of Supporting Information, which are in good agreement with that obtained by XRD characterizations. These numbers indicate that film $\{\bar{2}01\}$ plane is compressed along [010] orientation and stretched along [102] orientation with the increase of Mg at.%, which is compatible with the decrease of b_{β}, and the increase of a_{β} and c_{β} in **Figure 3.3(e)**. As seen in **Figure 3.4(d)**, the RHEED pattern of sample #10 in mixed phase exhibits the Debye ring, which indicates the polycrystal nature.[47] **Figure 3.4(e)-(f)** shows RHEED patterns of the rocksalt phase {111} plane along [1$\bar{1}$0] azimuth of samples #19 and #20, respectively. The in-plane lattice constant $a_{||[1\bar{1}0]}$, namely the distance between (11$\bar{2}$) planes was calculated as ~5.20 Å and ~5.12 Å for sample #19 and #20, respectively. Based on the rocksalt structure (**Figure 3.3(a)**), the lattice constant $a_{rocksalt}$ of MgGaO unit cell for sample #19 and #20 was calculated as $a_{||[1\bar{1}0]}$ / ($\sqrt{3/2}$), which is 4.25 Å and 4.18 Å, respectively (**Table S3.2**, Supporting Information). These are also in good agreement with the results obtained by XRD. It is noted that most RHEED patterns are not exactly streaky lines but contain spots, indicating the possible formation of islands in real space.[48] The atomic force microscope (AFM) 5 μm × 5 μm images of corresponding samples are shown in **Figure 3.4(g)-(l)**, and surface morphology of other samples were characterized by AFM as well (**Figure S3.7**, Supporting Information). The root mean square (RMS) roughness of all samples, which is also listed in **Table 3.1**, agrees with the RHEED results.

3.3.3 Film and substrate epitaxial relationship

To further study the in-plane epitaxial relationship of MgGaO thin films in both β and rocksalt phases on c-sapphire substrate, XRD φ-scans were measured. **Figure 3.5(a)** shows φ-scan patterns of β-MgGaO {010} of sample #03 at a position of the detector 2theta_chi = 60.961° and c-sapphire $\{10\bar{1}0\}$ (2theta_chi =68.212°) (PDF 00-046-1212). The φ-scan patterns of other β-phase samples #01 and #04 are shown in **Figure S3.8(a)-(b)** in Supporting Information. Similar to β-Ga_2O_3 on c-sapphire substrate,[44,46,49] six peaks are observed and separated by 60° for both φ-scan patterns of the substrate and film indicating the six-fold rotational symmetry for films growing on the c-sapphire {0001} plane in [0001] orientation. Compared with 1.8° rotation between $<102>_{f}$ and $<10\bar{1}0>_{s}$,[46] where the subscripts 'f' and 's' mean film and c-sapphire substrate, respectively, there is a 4° rotation between $<010>_{f}$ and $<10\bar{1}0>_{s}$. Besides, $\{\bar{2}01\}_{\beta\text{-phase}}<010>_{f} \perp \{\bar{2}01\}_{\beta\text{-phase}}<102>_{f}$, and $\{0001\}_{s}<10\bar{1}0>_{s} \perp \{0001\}_{s}<12\bar{3}0>_{s}$, therefore, the epitaxy relationship between the film and substrate in β phase is $\{\bar{2}01\}_{\beta\text{-phase}}<010>_{f} \parallel \{0001\}_{s}<10\bar{1}0>_{s}$, $\{\bar{2}01\}_{\beta\text{-phase}} <102>_{f} \parallel \{0001\}_{s}<12\bar{3}0>_{s}$ with a 4° rotation, which is illustrated in **Figure 3.5(b)**. **Figure 3.5(c)** shows φ-scan patterns of rocksalt MgGaO {110} of sample #19 at 2theta_chi =62.304° and c-sapphire $\{10\bar{1}0\}$ (2theta_chi =68.212°). φ-scan patterns of similar rocksalt samples #18 and #20 are shown in **Figure S3.8(c)-(d)** in Supporting Information. Six diffraction peaks with 60° separation show up similar to β-MgGaO, however, there is a 2° rotation between $<110>_{f}$ and $<10\bar{1}0>_{s}$. Besides, $\{111\}_{\text{rocksalt}}[1\bar{1}0]_{f} \perp \{111\}_{\text{rocksalt}}[11\bar{2}]_{f.}$ Thus, the epitaxy relationship between the film and substrate is $\{111\}_{\mathrm{rocksalt}}\langle 110\rangle_{f} \parallel \{0001\}_{s}\langle 10\bar{1}0\rangle_{s}$, and $\{111\}_{\mathrm{rocksalt}}\ \langle 11\bar{2}\rangle_{f} \parallel \{0001\}_{s}\langle 12\bar{3}0\rangle_{s}$ with a 2° rotation, which is illustrated in **Figure 3.5(d)**. The arrangement of oxygen atom in red circles in rocksalt {111} plane forms the hexagonal shape. Due to $\langle 110\rangle_{f} \parallel \langle 10\bar{1}0\rangle_{s}$ with a 2° rotation, the angle between $\langle 11\bar{2}\rangle_{f}$ and $\langle 21\bar{3}0\rangle_{s}$ is around 58°. In other words, the {111} plane of films rotates almost 60° matching {0001} plane of substrate.

Although β and rocksalt phases belong to the monoclinic system and cubic system, respectively, the arrangement of the oxygen atoms in the β phase $\{\bar{2}01\}$ plane and rocksalt

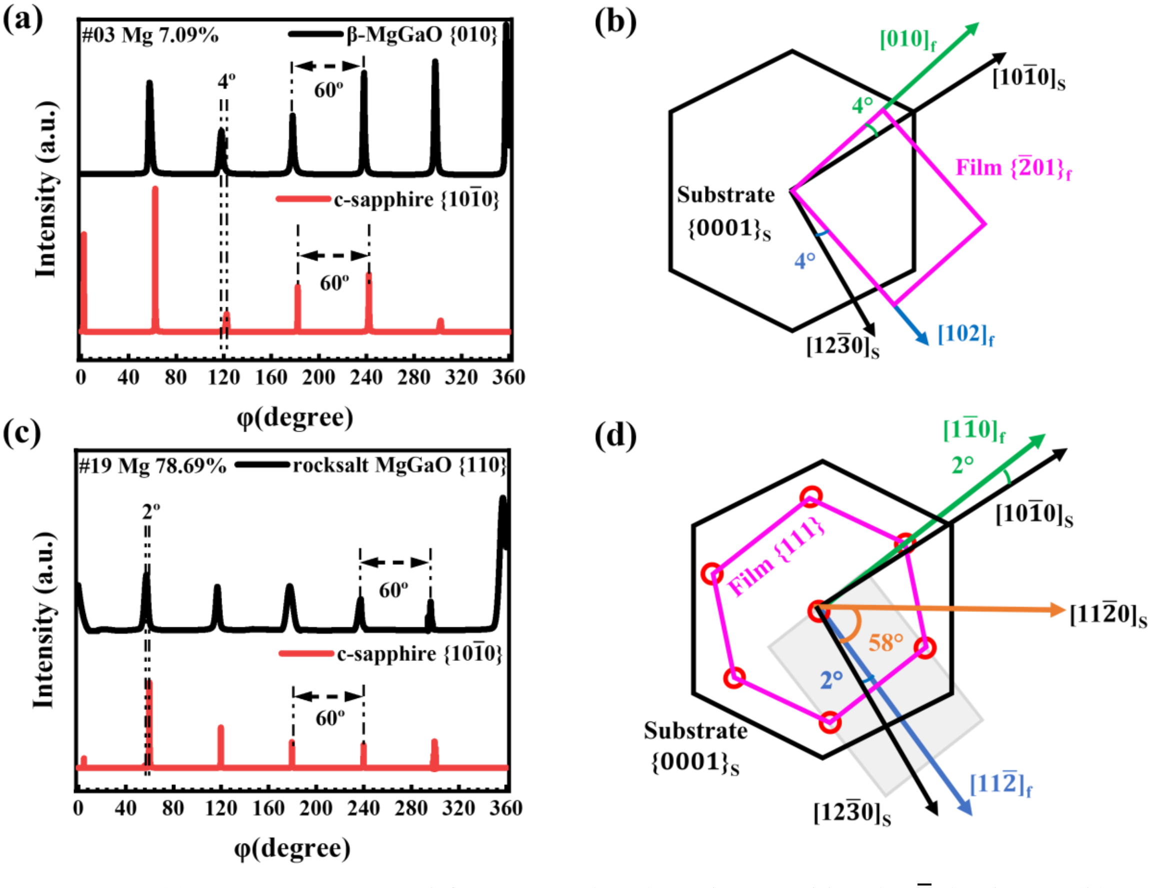

Figure 3.5 (a) φ-scan patterns of *β*-MgGaO {010} and c-sapphire $\{10\bar{1}0\}$ planes, (b) schematic diagram of epitaxial relationship for *β*-MgGaO and on c-sapphire substrate, (c) φ-scan patterns of rocksalt MgGaO {110} and c-sapphire $\{10\bar{1}0\}$ planes, and (d) schematic of epitaxial relationship of rocksalt MgGaO on c-sapphire substrate.

{111} plane is hexagonal, which is similar to the arrangement of oxygen atoms in the c-sapphire {0001} plane. Referring to the three PDF cards mentioned above, the atom arrangement of c-sapphire {0001} plane, β phase $\{\bar{2}01\}$ plane and rocksalt {111} plane is illustrated (**Figure S3.9**, Supporting Information). The o-o atom bond length along $\{0001\}_s[01\bar{1}0]$ orientation is ~2.725 Å, $\{\bar{2}01\}_{\beta\text{-phase}}[010]$ orientation is ~2.782 Å, and $\{111\}_{\text{rocksalt}}$ [110] orientation ~2.97 Å. It should be mentioned that o-o bond length along $\{111\}_{\text{rocksalt}}$ [110] orientation is equal to $\sqrt{2}$*Mg-O bond length. Because of similar hexagonal oxygen atom arrangement with similar bond lengths, both β phase and rocksalt phase MgGaO can be readily epitaxial on c-sapphire substrate.[49]

3.3.4 Film optical properties characterizations

Bandgaps of MgGaO samples were studied by absorption spectroscopy. **Figure 3.6(a)** shows Tauc-plot of the absorption spectra of all samples. Since direct bandgaps of ~5.0 eV for β-Ga_2O_3[50–52] and ~7.8 eV for MgO[53–55] were reported, their mixture MgGaO ternary alloys are assumed to possess the direct bandgap property. Tauc equation for semiconductors with direct bandgaps is expressed as:

$$(\alpha h\upsilon)^2 = A(h\upsilon - E_g) \tag{5}$$

where α is the absorption coefficient, hυ is energy, A is a proportionality constant. By extrapolating the linear segment of absorption spectra to intersect the hυ-axis with a fitting straight line, the bandgap was extracted and listed in **Table 3.1**. The maximum value of tuned bandgap is ~5.89 eV for sample #19, which has an Mg and Ga composition of ~79% and 21%, respectively. However, bandgap of sample #20 MgO cannot be measured due to the wavelength limitations (200-nm minimum) of UV-Vis-NIR spectrophotometer, although it is presumably equal to 7.8 eV. The transmittance of these samples was also measured using the same spectrophotometer, as shown in **Figure 3.6(b)**. ~90% transmittance of light at visible region were observed across the spectrum for all samples. **Figure 3.6(c)** shows bandgap as a function of Mg composition in the MgGaO films. The bandgap increases monotonically with the increase of Mg at.%.

To deduce the relationship between the bandgap and Mg composition, polynomial model was used to fit bandgap versus Mg at.%,[56] which is illustrated as the solid line in Figure 6(c). Due to the mixed phase crystal structure, and the limited data points in rocksalt regions, fitting was done only for beta phase, which can be written as: $E_g(x) = E_g(0) + A * x + B * x^2$, where $E_g(0)$ is the bandgap of Ga_2O_3, A and B are constant, x is the Mg atomic percent. The fitting yields the following formula:

$$E_g(x) = 5.03 + 0.21 * x + 2.94 * x^2 \tag{6}$$

Taking sample #07 as an example, where Mg at.% is 30.23%, therefore, $E_g(x) = 5.03 + 0.21 * 30.23\% + 2.94 * (30.23\%)^2 = 5.36$ eV, which is equal to the experimental value of 5.36 eV.

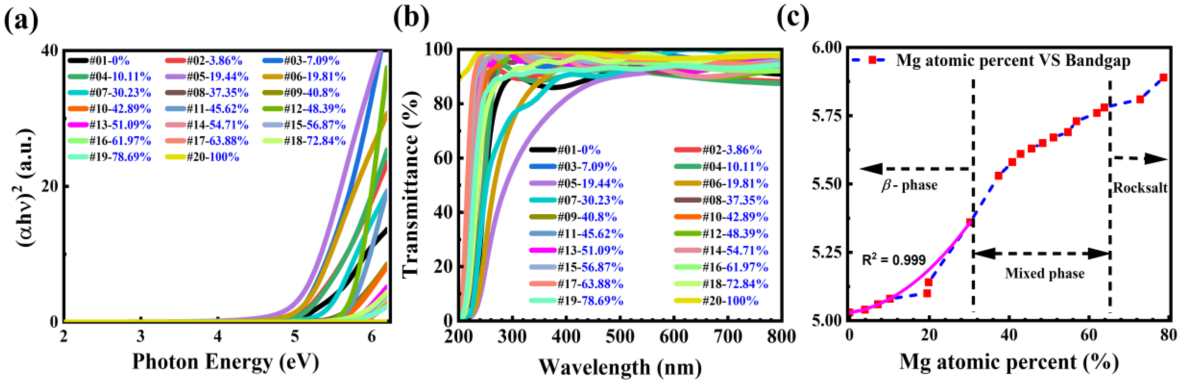

Figure 3.6 (a) Tauc plot of the absorption spectra, and (b) transmittance spectra of MgGaO thin films with Mg atomic percent ranging from 0 to 100%, (c) bandgap versus Mg atomic percent of MgGaO samples.

3.4 Conclusion

We systematically investigated the phase transition and bandgap engineering in UWBG MgGaO thin films. 20 samples with Mg at.% ranging from 0% to 100% were grown by MBE. Phase transformation from β phase to mixed phase, and finally to rocksalt phase was benchmarked. When Mg at.% is between 0 and 30.23%, MaGaO is pure β phase; when Mg at.% is between 37.35% and 63.88%, MgGaO is a mixture of β and rocksalt phases; when Mg at.% is larger than 72.84%, MaGaO films are pure rocksalt phase. Meanwhile, lattice parameter and bandgaps of MgGaO thin films were quantified and the epitaxial relationship between film in both β phase and rocksalt phase and substrate was determined. This work shows that MgGaO ternary alloy is an alternatively viable candidate for bandgap-increasing bandgap engineering of Ga_2O_3, therefore, it is promising for UWBG Ga_2O_3-based devices applications.

3.5 References

[1] J. B. Casady, R. W. Johnson, *Solid-State Electronics* **1996**, *39*, 1409.

[2] M. Kim, J.-H. Seo, U. Singisetti, Z. Ma, *J. Mater. Chem. C* **2017**, *5*, 8338.

[3] E. Monroy, F. Omn s, F. Calle, *Semicond. Sci. Technol.* **2003**, *18*, R33.

[4] J. Y. Tsao, S. Chowdhury, M. A. Hollis, D. Jena, N. M. Johnson, K. A. Jones, R. J. Kaplar, S. Rajan, C. G. Van de Walle, E. Bellotti, C. L. Chua, R. Collazo, M. E. Coltrin, J. A. Cooper, K. R. Evans, S. Graham, T. A. Grotjohn, E. R. Heller, M. Higashiwaki, M. S. Islam, P. W. Juodawlkis, M. A. Khan, A. D. Koehler, J. H. Leach, U. K. Mishra, R. J. Nemanich, R. C. N. Pilawa-Podgurski, J. B. Shealy, Z. Sitar, M. J. Tadjer, A. F. Witulski, M. Wraback, J. A. Simmons, *Advanced Electronic Materials* **2018**, *4*, 1600501.

[5] C. Xie, X.-T. Lu, X.-W. Tong, Z.-X. Zhang, F.-X. Liang, L. Liang, L.-B. Luo, Y.-C. Wu, *Advanced Functional Materials* **2019**, *29*, 1806006.

[6] S. J. Pearton, J. Yang, P. H. Cary, F. Ren, J. Kim, M. J. Tadjer, M. A. Mastro, *Applied Physics Reviews* **2018**, *5*, 011301.

[7] S. Oh, C.-K. Kim, J. Kim, *ACS Photonics* **2018**, *5*, 1123.

[8] Y. Qin, L. Li, X. Zhao, G. S. Tompa, H. Dong, G. Jian, Q. He, P. Tan, X. Hou, Z. Zhang, S. Yu, H. Sun, G. Xu, X. Miao, K. Xue, S. Long, M. Liu, *ACS Photonics* **2020**, *7*, 812.

[9] X. Chen, F. Ren, S. Gu, J. Ye, *Photon. Res.* **2019**, *7*, 381.

[10] B. Zhao, F. Wang, H. Chen, L. Zheng, L. Su, D. Zhao, X. Fang, *Advanced Functional Materials* **2017**, *27*, 1700264.

[11] Z. Liu, T. Yamazaki, Y. Shen, T. Kikuta, N. Nakatani, Y. Li, *Sensors and Actuators B: Chemical* **2008**, *129*, 666.

[12] U. Lampe, M. Fleischer, H. Meixner, *Sensors and Actuators B: Chemical* **1994**, *17*, 187.

[13] S. Sharma, K. Zeng, S. Saha, U. Singisetti, *IEEE Electron Device Letters* **2020**, *41*, 836.

[14] M. Higashiwaki, K. Sasaki, T. Kamimura, M. Hoi Wong, D. Krishnamurthy, A. Kuramata, T. Masui, S. Yamakoshi, *Applied Physics Letters* **2013**, *103*, 123511.

[15] K. Zeng, A. Vaidya, U. Singisetti, *IEEE Electron Device Letters* **2018**, *39*, 1385.

[16] Y. Chen, Y. Lu, X. Yang, S. Li, K. Li, X. Chen, Z. Xu, J. Zang, C. Shan, *Materials Today Physics* **2021**, *18*, 100369.

[17] F. Zhang, K. Saito, T. Tanaka, M. Nishio, Q. Guo, *Solid State Communications* **2014**, *186*, 28.

[18] F. Zhang, K. Saito, T. Tanaka, M. Nishio, Q. Guo, *Journal of Alloys and Compounds* **2014**, *614*, 173.

[19] T. Oshima, S. Fujita, *physica status solidi c* **2008**, *5*, 3113.

[20] I. Hamberg, C. G. Granqvist, K.-F. Berggren, B. E. Sernelius, L. Engström, *Phys. Rev. B* **1984**, *30*, 3240.

[21] J. Zhang, J. Shi, D.-C. Qi, L. Chen, K. H. L. Zhang, *APL Materials* **2020**, *8*, 020906.

[22] D. Wang, K. Ge, D. Meng, Z. Chen, *Materials Letters* **2023**, *330*, 133251.

[23] Y.-S. Shen, W.-K. Wang, R.-H. Horng, *IEEE Journal of the Electron Devices Society* **2017**, *5*, 112.

[24] A. K. Singh, C.-C. Yen, K.-P. Chang, D.-S. Wuu, *Journal of Luminescence* **2023**, *260*, 119836.

[25] F. Alema, B. Hertog, O. Ledyaev, D. Volovik, G. Thoma, R. Miller, A. Osinsky, P. Mukhopadhyay, S. Bakhshi, H. Ali, W. V. Schoenfeld, *physica status solidi (a)* **2017**, *214*, 1600688.

[26] I. Hatipoglu, P. Mukhopadhyay, F. Alema, T. S. Sakthivel, S. Seal, A. Osinsky, W. V. Schoenfeld, *J. Phys. D: Appl. Phys.* **2020**, *53*, 454001.

[27] Y.-C. Cheng, S.-P. Chang, C.-P. Yang, S.-J. Chang, *Applied Physics Letters* **2019**, *114*, 192102.

[28] Y.-S. Shen, W.-K. Wang, R.-H. Horng, *IEEE Journal of the Electron Devices Society* **2017**, *5*, 112.

[29] A. F. M. A. U. Bhuiyan, Z. Feng, J. M. Johnson, H.-L. Huang, J. Hwang, H. Zhao, *Appl. Phys. Lett.* **2020**, *117*, 142107.

[30] F. Zhang, K. Saito, T. Tanaka, M. Nishio, M. Arita, Q. Guo, *Appl. Phys. Lett.* **2014**, *105*, 162107.

[31] R. Miller, F. Alema, A. Osinsky, *IEEE Transactions on Semiconductor Manufacturing* **2018**, *31*, 467.

[32] T. Yang, C. Shou, L. Xu, J. Tran, Y. He, Y. Li, P. Wei, J. Liu, *ACS Appl. Electron. Mater.* **2023**, *5*, 2122.

[33] C. Shou, T. Yang, A. Almujtabi, T. Yang, Y. Li, Q. S. Mahmud, M. Xu, J.-G. Zheng, J. Liu, *Applied Physics Letters* **2023**, *122*, 212101.

[34] N. Zhang, H. Liu, Q. Sai, C. Shao, C. Xia, L. Wan, Z. C. Feng, H. F. Mohamed, *J Mater Sci* **2021**, *56*, 13178.

[35] S.-Y. Chu, T.-H. Yeh, C.-T. Lee, H.-Y. Lee, *Materials Science in Semiconductor Processing* **2022**, *142*, 106471.

[36] P. Gao, X. Tian, C. Yang, Z. Zhou, Y. Li, Y. Wang, S. Komarneni, *Environ. Sci.: Nano* **2016**, *3*, 1416.

[37] L. Sharma, R. Kakkar, *ACS Appl. Mater. Interfaces* **2017**, *9*, 38629.

[38] P. Casey, G. Hughes, E. O'Connor, R. D. Long, P. K. Hurley, *J. Phys.: Conf. Ser.* **2008**, *100*, 042046.

[39] I. López, A. D. Utrilla, E. Nogales, B. Méndez, J. Piqueras, A. Peche, J. Ramírez-Castellanos, J. M. González-Calbet, *J. Phys. Chem. C* **2012**, *116*, 3935.

[40] A. Mahmoodinezhad, C. Janowitz, F. Naumann, P. Plate, H. Gargouri, K. Henkel, D. Schmeißer, J. I. Flege, *Journal of Vacuum Science & Technology A* **2020**, *38*, 022404.

[41] T. Onuma, S. Fujioka, T. Yamaguchi, Y. Itoh, M. Higashiwaki, K. Sasaki, T. Masui, T. Honda, *Journal of Crystal Growth* **2014**, *401*, 330.

[42] D. Wu, Y. Bai, W. Wang, H. Xia, F. Tan, S. Zhang, B. Su, X. Wang, X. Qiao, P. K. Wong, *Journal of Hazardous Materials* **2019**, *374*, 319.

[43] S. Rafique, L. Han, H. Zhao, *ECS Trans.* **2017**, *80*, 203.

[44] B. Feng, Z. Li, F. Cheng, L. Xu, T. Liu, Z. Huang, F. Li, J. Feng, X. Chen, Y. Wu, G. He, S. Ding, *physica status solidi (a)* **2021**, *218*, 2000457.

[45] J. Wei, K. Kim, F. Liu, P. Wang, X. Zheng, Z. Chen, D. Wang, A. Imran, X. Rong, X. Yang, F. Xu, J. Yang, B. Shen, X. Wang, *J. Semicond.* **2019**, *40*, 012802.

[46] W. Seiler, M. Selmane, K. Abdelouhadi, J. Perrière, *Thin Solid Films* **2015**, *589*, 556.

[47] D. Toliopoulos, A. Fedorov, S. Bietti, M. Bollani, E. Bonera, A. Ballabio, G. Isella, M. Bouabdellaoui, M. Abbarchi, S. Tsukamoto, S. Sanguinetti, *Nanomaterials* **2020**, *10*, 2542.

[48] G. Liang, L. Cheng, J. Zha, H. Cao, J. Zhang, Q. Liu, M. Bao, J. Liu, X. Zhai, *Nano Res.* **2022**, *15*, 1654.

[49] R. Chen, D. Wang, J. Liu, B. Feng, H. Zhu, X. Han, C. Luan, J. Ma, H. Xiao, *Crystal Growth & Design* **2022**, *22*, 5285.

[50] Z. Chen, K. Ge, D. Meng, X. Chen, *Materials Letters* **2022**, *320*, 132385.

[51] Z. Galazka, *Semicond. Sci. Technol.* **2018**, *33*, 113001.

[52] T. Onuma, S. Fujioka, T. Yamaguchi, M. Higashiwaki, K. Sasaki, T. Masui, T. Honda, *Applied Physics Letters* **2013**, *103*, 041910.

[53] V. E. Nefedova, S. Fröhlich, F. Navarrete, N. Tancogne-Dejean, D. Franz, A. Hamdou, S. Kaassamani, D. Gauthier, R. Nicolas, G. Jargot, M. Hanna, P. Georges, M. F. Ciappina, U. Thumm, W. Boutu, H. Merdji, *Appl. Phys. Lett.* **2021**, *118*, 201103.

[54] S. Bhakta, P. K. Sahoo, *Appl. Phys. A* **2022**, *128*, 990.

[55] D. M. Roessler, W. C. Walker, *Phys. Rev.* **1967**, *159*, 733.

[56] D. Bensaid, M. Ameri, N. Benseddik, A. Mir, N. E. Bouzouira, F. Benzoudji, *International Journal of Metals* **2014**, *2014*, e286393.

Supporting Information

1.XPS details of Ga 2s, Mg 2s, 2p and O 1s spectra

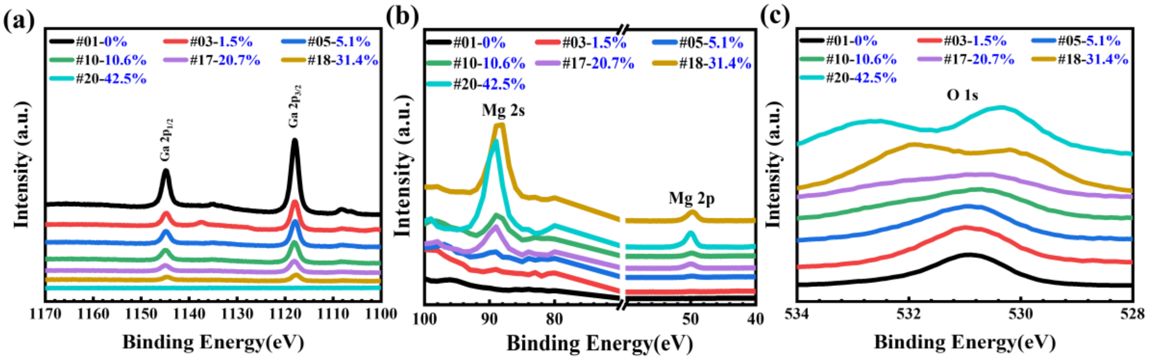

Figure S3.1 XPS analysis of sample #01, #03, #05, #10, #17, #18, and #20: (a) Ga 2p spectra, (b) Mg 2s, 2p spectra, (c) O 1s spectra.

2. Raman spectra

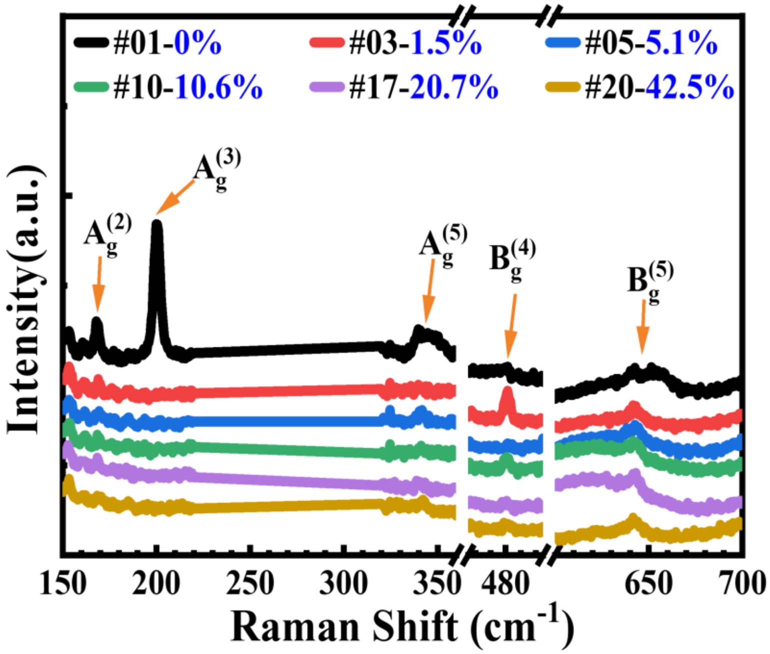

Figure S3.2 Raman spectra of sample #01, #03, #05, #10, #17, #18, and #20.

3. Out-of-plane reciprocal space mappings

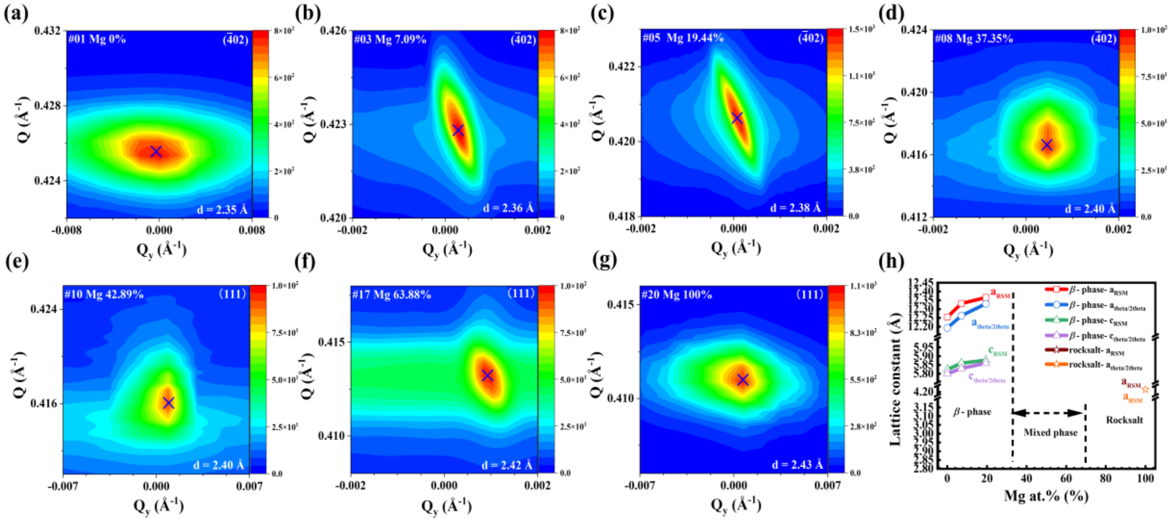

Figure S3.3 Out-of-plane reciprocal space mappings for beta phase MgGaO ($\bar{4}02$) plane with Mg atomic percent at (a) 0%, (b) 7.09%, (c)19.44% and (d) 37.35%, respectively. RSM for rocksalt MgGaO (111) plane with Mg atomic percent at (e) 42.89%, (f) 63.88%, and (g)100%, respectively. (h) lattice parameter comparison in RSM and theta-2theta methods.

4. In-plane reciprocal space mappings

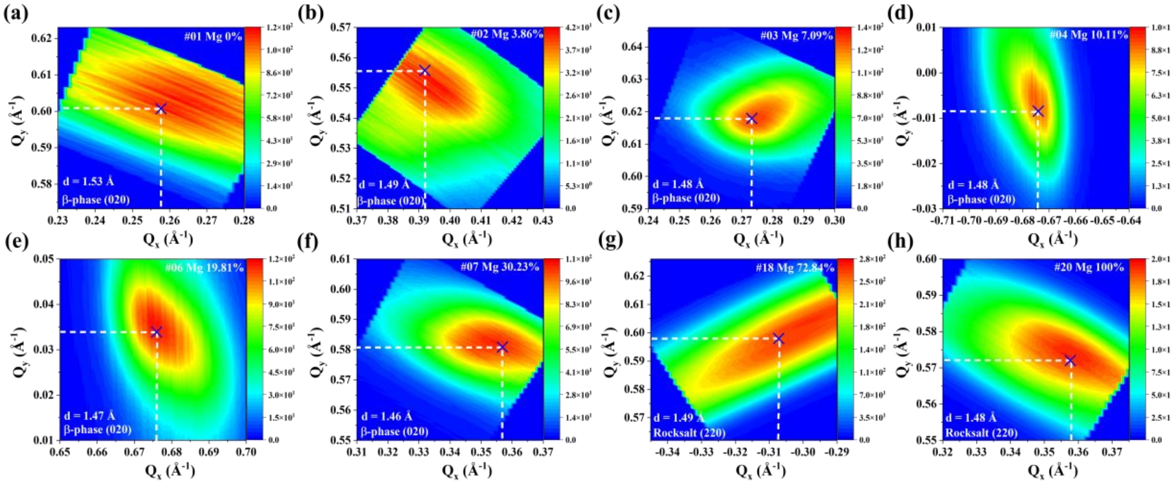

Figure S3.4 In-plane reciprocal space mappings of MgGaO with various Mg atomic percent for beta phase (020) plane: (a) 0%, (b) 3.86%, (c) 7.09%, (d) 10.11%, (e) 19.81%, (f) 30.23%, respectively, and for rocksalt (220) plane: (g) 72.84%, (h) 100%, respectively.

5. RHEED images

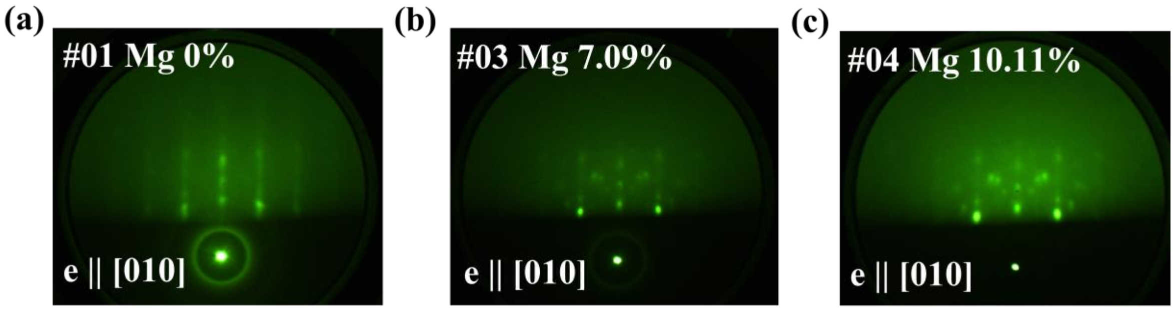

Figure S3.5 RHEED images of MgGaO samples with (a) Mg 0%, (b) Mg 7.09%, and (c) Mg 10.11% along [010] azimuth.

6. Schematic of calculation for a_β and c_β based on RHEED

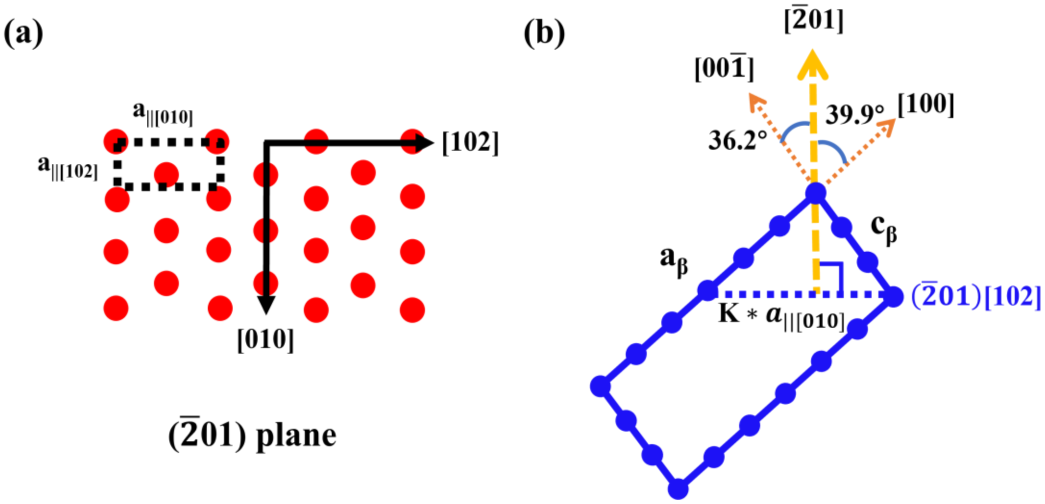

Figure S3.6 (a) Atom arrangement of $(\bar{2}01)$ plane, (b) Side-view of unit cell for calculation of lattice constants a_β and c_β from in-plane lattice constant obtained from RHEED.

7. AFM images

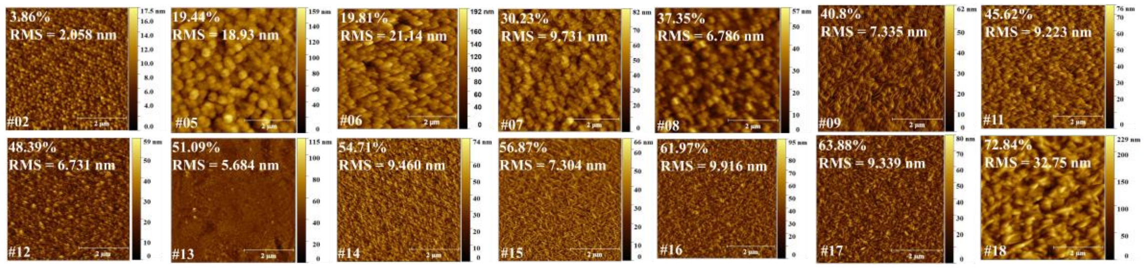

Figure S3.7 AFM images of additional MgGaO ternary alloy thin films with various Mg atomic percent.

8. XRD φ-scans spectra

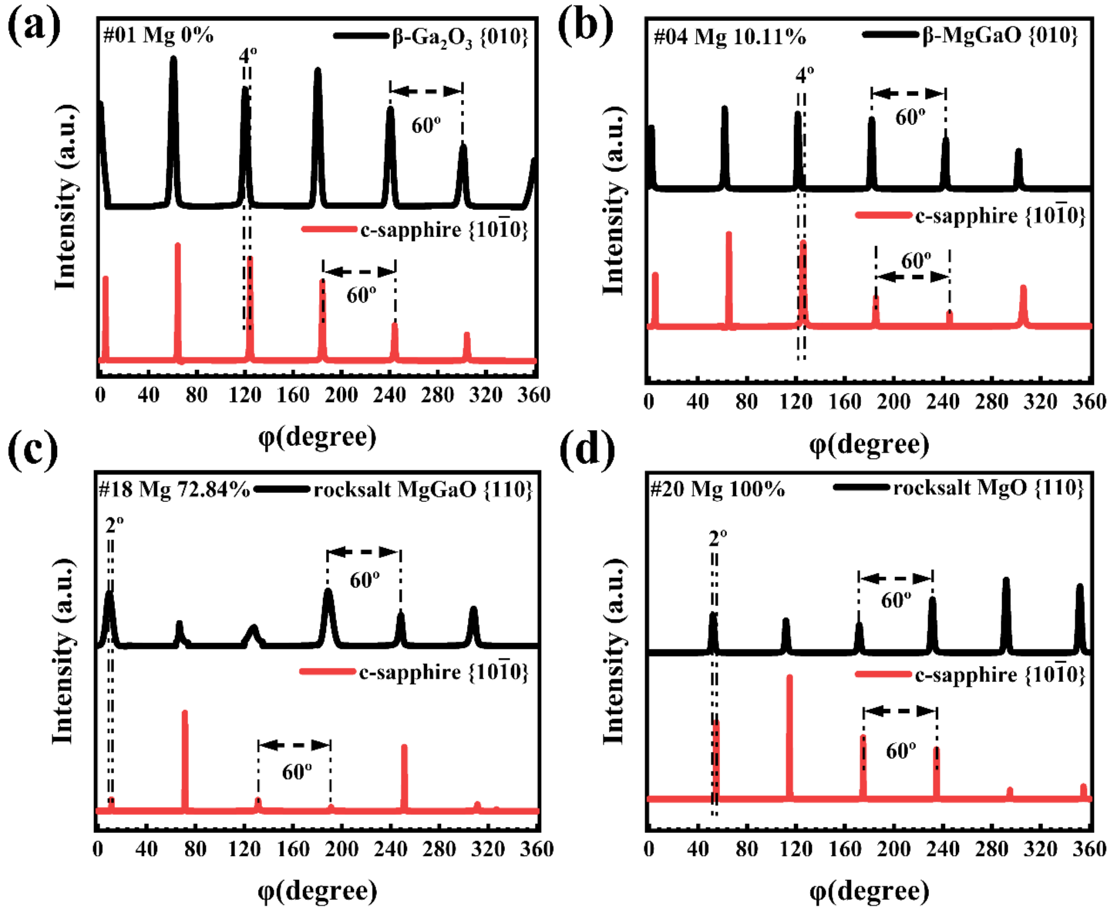

Figure S3.8 (a)-(b) XRD φ-scans of β-MgGaO {010} and c-sapphire {10$\bar{1}$0} planes, (c)-(d) XRD φ-scans of rocksalt MgGaO {110} and c-sapphire {10$\bar{1}$0} planes.

9. Atom arrangement of c-sapphire {0001}, β-Ga_2O_3 $\{\bar{2}01\}$, and MgO {111} plane

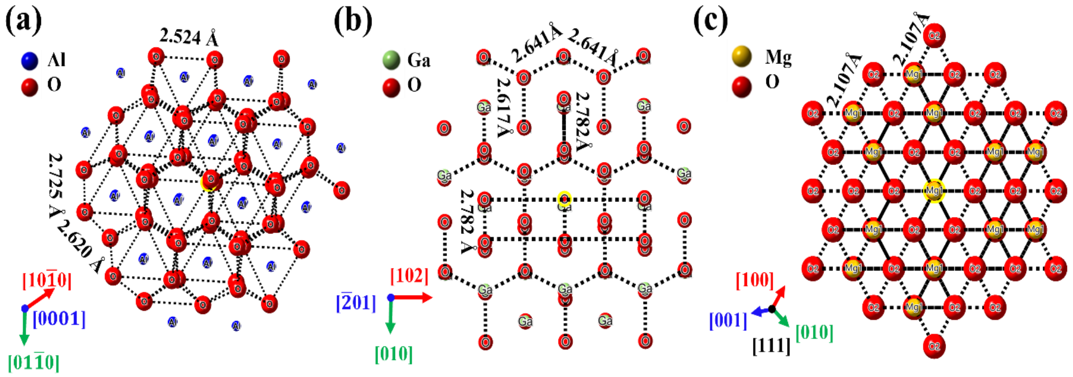

C-sapphire {0001} O-O bond

Beta phase $\{\bar{2}01\}$ O-O bond

Rocksalt {111} Mg-O bond

Figure S3.9 Schematic of atom arrangement of (a) c-sapphire {0001}, (b) beta phase Ga_2O_3 $\{\bar{2}01\}$, and (c) rocksalt MgO {111} plane.

10. XRD peak positions, FWHM, d-spacing, and lattice parameters

Table S3.1 XRD peak position, FWHM and d-spacing of MgGaO ternary films with Mg at. % ranging from 0 to 100%.

<table>
<tr><th>Sample</th><th>hkl</th><th>Pos., 2θ (°)</th><th>FWHM, 2θ (°)</th><th>($\bar{4}$02) d-spacing (Å)</th><th>Lattice constant a_β (Å)</th><th>Lattice constant b_β (Å)</th><th>Lattice constant c_β (Å)</th></tr>
<tr><td>#01 Mg 0%</td><td>($\bar{4}$02)</td><td>38.47</td><td>0.252</td><td>2.34</td><td>12.19</td><td>3.06</td><td>5.79</td></tr>
<tr><td>#02 Mg 3.86%</td><td>($\bar{4}$02)</td><td>38.41</td><td>0.272</td><td>2.34</td><td>12.21</td><td>2.99</td><td>5.80</td></tr>
<tr><td>#03 Mg 7.09%</td><td>($\bar{4}$02)</td><td>38.24</td><td>0.334</td><td>2.35</td><td>12.26</td><td>2.96</td><td>5.83</td></tr>
<tr><td>#04 Mg 10.11%</td><td>($\bar{4}$02)</td><td>38.18</td><td>0.249</td><td>2.35</td><td>12.28</td><td>2.96</td><td>5.84</td></tr>
<tr><td>#05 Mg 19.44%</td><td>($\bar{4}$02)</td><td>38.03</td><td>0.203</td><td>2.36</td><td>12.33</td><td>2.95</td><td>5.86</td></tr>
<tr><td>#06 Mg 19.81%</td><td>($\bar{4}$02)</td><td>38.03</td><td>0.190</td><td>2.36</td><td>12.33</td><td>2.96</td><td>5.86</td></tr>
<tr><td>#07 Mg 30.23%</td><td>($\bar{4}$02)</td><td>37.88</td><td>0.255</td><td>2.37</td><td>12.38</td><td>2.93</td><td>5.88</td></tr>
<tr><td>#08 Mg 37.35%</td><td>(111)
($\bar{4}$02)</td><td>37.70
38.42</td><td>0.184
0.156</td><td colspan="4" rowspan="10">Mixed phase</td></tr>
<tr><td>#09 Mg 40.80%</td><td>(111)</td><td>37.62</td><td>0.457</td></tr>
<tr><td>#10 Mg 42.89%</td><td>(111)
($\bar{4}$02)</td><td>37.59
38.43</td><td>0.519
0.173</td></tr>
<tr><td>#11 Mg 45.62%</td><td>(111)
($\bar{4}$02)</td><td>37.57
38.45</td><td>1.152
0.174</td></tr>
<tr><td>#12 Mg 48.39%</td><td>(111)
($\bar{4}$02)</td><td>37.52</td><td>0.599</td></tr>
<tr><td>#13 Mg 51.09%</td><td>(111)
($\bar{4}$02)</td><td>37.47
38.43</td><td>0.615
0.195</td></tr>
<tr><td>#14 Mg 54.71%</td><td>(111)
($\bar{4}$02)</td><td>37.36
38.44</td><td>0.440
0.187</td></tr>
<tr><td>#15 Mg 56.87%</td><td>(111)
($\bar{4}$02)</td><td>37.35
38.45</td><td>0.495
0.174</td></tr>
<tr><td>#16 Mg 61.97%</td><td>(111)
($\bar{4}$02)</td><td>37.34
38.44</td><td>0.441
0.198</td></tr>
<tr><td>#17 Mg 63.88%</td><td>(111)
($\bar{4}$02)</td><td>37.30
38.45</td><td>0.418
0.172</td></tr>
<tr><td rowspan="2">#18 Mg 72.84%</td><td rowspan="2">(111)</td><td rowspan="2">37.06</td><td rowspan="2">0.573</td><th>(111) d-spacing (Å)</th><th colspan="2">Lattice constant $a_{rocksalt}$ (Å) (θ/2θ)</th><th>Lattice constant $a_{rocksalt}$ (Å) (RSM)</th></tr>
<tr><td>2.42</td><td colspan="2">4.20</td><td>4.21</td></tr>
<tr><td>#19 Mg 78.69%</td><td>(111)</td><td>37.06</td><td>0.572</td><td>2.42</td><td colspan="2">4.20</td><td>4.21</td></tr>
<tr><td>#20 Mg 100.0%</td><td>(111)</td><td>36.91</td><td>0.268</td><td>2.43</td><td colspan="2">4.21</td><td>4.20</td></tr>
</table>

11. RHEED parameter and lattice constant

Table S3.2 RHEED pattern parameter and lattice constant.

Beta phase $\{\bar{2}01\}$ **plane**	**In-plane lattice constant (Å)** e ‖ [102]	**In-plane lattice constant (Å)** e ‖ [010]	**Lattice constant** a_β **(Å)**	**Lattice constant** b_β **(Å)**	**Lattice constant** c_β **(Å)**
#01 Mg 0%	2.98	5.06	12.62	2.98	6.00
#03 Mg 7.09%	2.88	5.11	12.75	2.88	6.06
#04 Mg 10.11%	2.84	5.17	12.89	2.84	6.13
Rocksalt phase **{111} plane**	**In-plane lattice constant (Å)** e ‖ [1$\bar{1}$0]	**Lattice constant** $a_{rocksalt}$ **(Å)**			
#19 Mg 100.0%	5.20	4.25			
#20 Mg 100.0%	5.12	4.18			

Chapter 4: Photoluminescence study of $MgGa_2O_4$ spinel oxide films grown by molecular beam epitaxy

4.1 Introduction

With the properties of transparency to visible light, transparent semiconducting oxides (TSOs) of optical bandgap larger than ~3 eV have great potential in electronic and optoelectronic applications, such as deep ultraviolet (UV) photodetectors, photodiodes, Schottky diodes, transparent thin film transistors, etc.[1,2] Among these TSO materials, ZnO,[3,4] In_2O_3,[5] SnO_2,[6,7] and Ga_2O_3[8,9] are extensively studied. Previously, we explored the possibility of Ga_2O_3 with Mg incorporation in beta phase for deep UV photodetector applications.[10,11] MgGaO ultrawide bandgap engineering with normalized Mg at.%/Ga at.% ranging from 0%/100% to 100%/0% was investigated for study of phase transition and optical properties as well.[12] Among all different element composition combinations, It is reported that the inverse spinel magnesium gallate ($MgGa_2O_4$) of normalized Mg at.%/Ga at.% at 33.33%/66.67% is applicable for solar blind photodetector applications[13–15] due to its reported large bandgap (4.7–5.36 eV) at room temperature,[14,15] good mechanical properties, high radiation hardness,[14] and high thermal chemical stability at high temperature.[16,17] Meanwhile, as a good luminescent material, the $MgGa_2O_4$ luminescence properties were studied with incorporation of Mn^{2+} for green,[18,19] Eu^{3+} for red,[19,20] and Cr^{3+}, Ni^{+} for near-infrared light emission.[21–24] Nevertheless, there are only very few room temperature photoluminescence (PL) studies of native defects in $MgGa_2O_4$ itself to illustrate the PL mechanism,[25,26] in contrast to extensive PL studies of β-Ga_2O_3 with/without Mg doped.[27–29] In addition, $MgGa_2O_4$ is mostly produced by Czochralski method[2,30] or high-temperature solid reaction methods[31–33] as bulk materials. Towards electronic and optoelectronic device applications, a few epitaxial film growth attempts are reported recently by metalorganic chemical vapor deposition (MOCVD)[13,15] or pulsed laser deposition (PLD)[14] methods. As an alternative precise growth control method, molecular beam epitaxy (MBE) has not been used for $MgGa_2O_4$ growth yet. In this chapter, $MgGa_2O_4$ epitaxial films were grown by MBE. The structural, optical and surface morphology properties were studied. In particular, comprehensive PL studies including power dependent and temperature dependent PL were carried out. PL mechanism involving optical transitions through self-trapped hole (STH), oxygen vacancy deep donor, and Mg on Ga site deep acceptor energy levels is revealed in spinel $MgGa_2O_4$, compared to a reference β-Ga_2O_3 sample.

4.2 Experimental Details

4.2.1 Film growth

$MgGa_2O_4$ films were grown on two-inch c-sapphire substrates by using an RF oxygen plasma assisted MBE system (SVT Associates, Inc.). Piranha solution (H_2O_2: H_2SO_4 = 3:5) at 200 °C was used to clean substrate for about 20 minutes, followed by deionized water rinse process. After dried by nitrogen gas, substrate was transferred to the loadlock chamber of MBE immediately. Mg (4N) and Ga shots (6N) (Alfa Aesar) high-purity elemental sources in effusion cells were used for sample growth. To achieve an atomic level surface at high of 10^{-9} torr, a pre-growth substrate annealing process was performed at 800 ˚C for 20 minutes. The Ga and Mg effusion cell temperature was fixed at 750 and 410 °C, respectively. The growth temperature for spinel samples #2 to #4 was set as 400, 500 and 600 ºC, respectively, while it was set at 600 ºC for reference beta phase Ga_2O_3 sample #1. Meanwhile, 2.0 sccm flux of oxygen under 400 W RF plasma was introduced for 5 h. Then, a post-growth annealing process without oxygen atmosphere was operated at 700 ˚C for 20 minutes. The growth conditions are listed in **Table S4.1** of Supporting Information.

4.2.2 Film characterizations

Film thickness was measured by a Veeco Dektak 8 profilometer. Mg, Ga and O compositions of all samples were measured by energy-dispersive X-ray (EDX) in a TESCAN SBH scanning electron microscope (SEM). For film phase determination, film quality, epitaxial relationship and lattice constant investigation, x-ray diffraction (XRD) theta-2theta, rocking curve, in-plane phi scan and reciprocal space mapping (RSM) of the samples were measured by using a Bruker D8 Advance X-ray diffractometer and a Rigaku SmartLab X-ray diffractometer with Cu Kα (λ = 0.15405 nm) radiation at room temperature, respectively. Absorption and transmittance spectra were measured using a high-performance UV-Vis-NIR spectrophotometer (Cary 5000, Agilent Inc.). PL spectra were measured with a home-built PL system, which is equipped with a 193-nm ArF excimer laser.

4.3 Results and Discussion

4.3.1 Film characterizations

Film thicknesses are recorded as ~364.35 nm, ~981.18 nm, ~1122.36 nm and ~1217.86 nm for samples #1-#4, respectively. **Figure 4.1(a)** shows EDX spectra of the four samples.

Similar to the reported $MgGa_2O_4$ EDX spectra,[13] the O kα, Ga Lα and Mg Kα peaks are located around 0.525, 1.098 and 1.253 keV, respectively, and Al signal from the substrate is undetected due to the large film thickness. As listed in **Table S4.1** in the Supporting Information, the Ga at.%/O at.% of sample #1 is 40.05%/59.95%, while the Mg at.%/Ga at.%/O at.% is 15.26%/27.71%/57.03%, 14.62%/27.60%/57.78%, and 14.25%/28.58%/57.17% for sample #2, #3 and #4, respectively. Element atomic ratios of all three spinel samples are close to nominal value of spinel $MgGa_2O_4$,[34] namely 14.28%/28.57%/57.15%, although Mg at.% decreases slightly with the increase of substrate temperature. Cross-sectional SEM image of sample #4 is shown in **Figure 4.1(b)**,

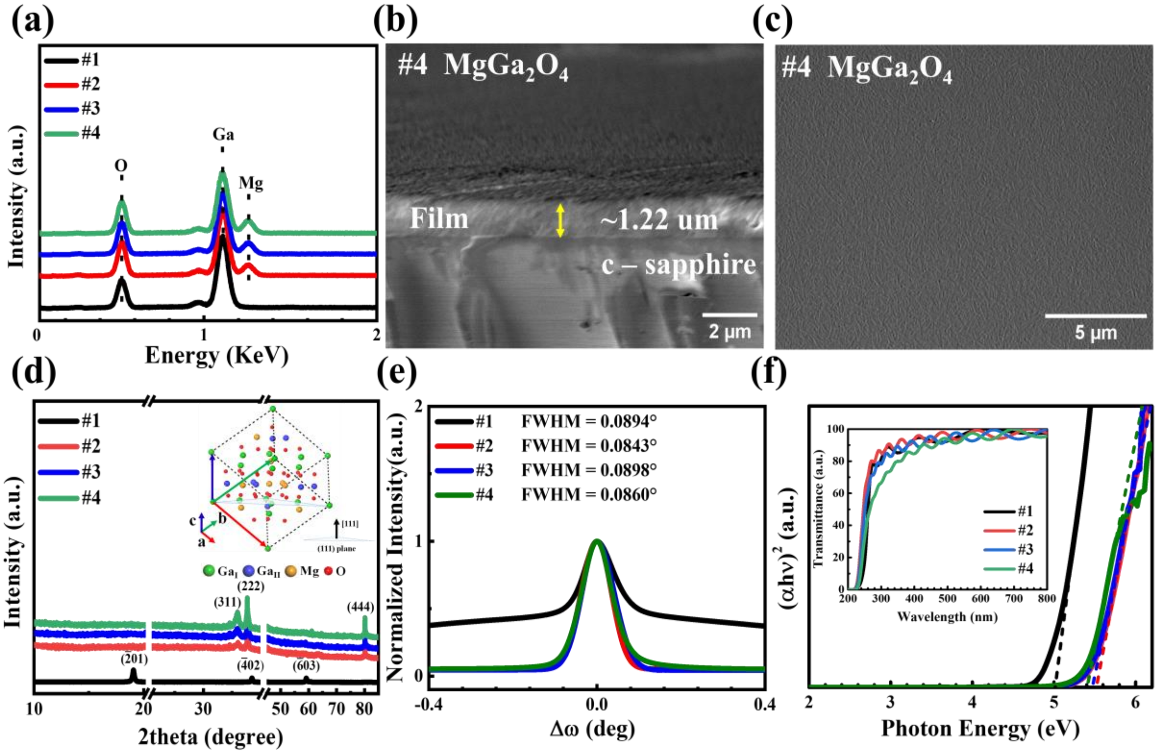

Figure 4.1 (a) EDX spectra of β-Ga_2O_3 and spinel $MgGa_2O_4$ thin films. (b) SEM cross-section and (c) surface morphology image of sample #4. (d) XRD pattern in theta-2theta scan mode (inset is the spinel structure schematic). (e) Normalized XRD rocking curves for β-Ga_2O_3 $(\bar{4}02)$ and spinel $MgGa_2O_4$ (222) peaks. (f) Tauc-plot of absorption spectra (inset is the transmittance spectra).

while the images of other samples are shown in **Figure S4.1(a)-(c)** of Supporting Information. The results indicate that the films grow epitaxially well with substrate, and the film thickness of the samples match the values measured by profilometer. SEM surface morphology of sample #4 in **Figure 4.1(c)** and sample #1 to #3 in **Figure S4.1(d)-(f)** indicate the smooth surface for all samples.

Figure 4.1(d) shows XRD pattern in θ/2θ scan mode. Compared to the clear monoclinic structure of sample #1 with three typical diffraction peaks $(\bar{2}01)$, $(\bar{4}02)$, and $(\bar{6}03)$,[10–12] which are located at ~19.12 °, 38.50 °, and 59.14 °, respectively, three diffraction peaks located at ~35.93 °, 37.59 °, and 80.24 °correspond to the spinel phases of (311), (222) and (444) in samples #2-#4, respectively.[15,33–35] According to Bragg's law, the d-spacing value of (222) plane is calculated to be ~2.390 Å, therefore, the lattice constant a_{spinel} is $2\sqrt{3}d_{(222)}$, namely 8.282 Å, which is in good agreement with the nominal value of 8.288 Å reported in $MgGa_2O_4$ PDF 00-010-0133. Inset of Figure 1(d) is a schematic of spinel $MgGa_2O_4$ structure with two kinds of Ga atoms located in both tetrahedral and octahedral sites while the Mg atom locates only in octahedral site, namely $Ga^{tet}(MgGa)^{oct}O_4$.[36] The (111) plane is marked to indicate more preferred <111> growth orientation with respect to <311> direction in the spinel sample. **Figure 4.1(e)** shows normalized XRD rocking curves for β-Ga_2O_3 $(\bar{4}02)$ and spinel $MgGa_2O_4$ (222) peaks. The full width at half maximum (FWHM) of the curves for sample #1-#4 is recorded as 0.0894°, 0.0843°, 0.0898° and 0.0860°, respectively. The small values indicate that the films have very good quality. Spinel $MgGa_2O_4$ film thickness dependent experiment was also carried out, as shown in **Table S2** and **Figure S2** in the Supporting Information, revealing single crystallinity.

Figure 4.1(f) shows absorption spectra of the samples. Both β-Ga_2O_3 and spinel $MgGa_2O_4$ are reported to be direct bandgap semiconductors,[10–12,14,15] Thus, the Tauc equation is expressed as $(\alpha h\upsilon)^2 = A(h\upsilon - E_g)$, where α is the absorption coefficient, hυ is energy, A is a proportionality constant. By extrapolating the linear segment of absorption spectra to intersect the hυ-axis with a fitting straight line, the bandgap was extracted as 5.02 eV for sample #1 β-Ga_2O_3, and 5.52 eV, 5.47 eV and 5.41 eV for spinel samples #2, #3 and #4, respectively, which is similar to the reported undoped $MgGa_2O_4$ bandgap 5.36 eV.[23] The bandgap decreases with the increase of substrate temperature due to less Mg incorporation.[35] The inset transmittance spectra in **Figure 4.1(f)** indicate that ~90% transmittance of light at visible region was observed across the spectra for all samples.

4.3.2 Room temperature PL

Figure 4.2(a) shows room temperature PL spectra at an incident power density of 12.8 mW/ cm^2 for β-Ga_2O_3 sample #1 and spinel $MgGa_2O_4$ samples #2-#4. All spectra show broad luminescence[37] with main peak at maximum intensity located at ~409.99 nm for β-Ga_2O_3, ~428.01, 431.01, and 453.99 nm for spinel samples, respectively. Room temperature PL peak deconvolution was performed to extract the optical transitions of all samples. PL deconvoluted peaks of $MgGa_2O_4$ sample #4 are shown in **Figure 4.2(b)**, which are ~3.28 eV for UV_I emission, ~4.18 eV for UV_{II} emission, ~3.09 eV for violet, ~2.67 eV for blue, and ~2.30 eV for green emissions, respectively. The PL peak deconvolutions for the other two spinel samples (sample #2 and #3) are shown in **Figure S4.3** as well. An energy level diagram of the PL mechanism of spinel $MgGa_2O_4$ films is illustrated in **Figure**

4.2(c). Self-trapped holes into polaron states are widely existed in wide bandgap oxides,[38–40] thus, UV_I emission of spinel $MgGa_2O_4$ is due to the recombination of electrons in conduction band and STHs. Assuming the polaronic STH energy level $E_{polaron}^{STH}$ is the same as that of β-Ga_2O_3, namely, it is located at ~1.1 eV above the valence band,[41] the UV_I emission can be calculated as $E_{UV_I} = E_g - E_{polaron}^{STH} - E_{STH}^{bind}$, where E_g is the bandgap and E_{STH}^{bind} is the self-trapping energy or the binding energy of STH to oxygen atom.[41] E_{STH}^{bind} is estimated to be ~1.20, 1.10 and 1.03 eV for sample #2-#4, respectively. It is noted that the reported self-trapped hole delocalization energy of 0.53 eV for β-Ga_2O_3.[41,42] This deviation indicates that β-phase Ga_2O_3 and spinel $MgGa_2O_4$ are different materials, which could be due to the different STH positions in spinel $MgGa_2O_4$ compared to pure β-Ga_2O_3, which requires further investigation. Considering the relative atomic percent of Mg to Ga in spinel samples, UV_{II} emission may be ascribed to radiative recombination of electrons in conduction band and holes occupied in antisite Mg_{Ga} deep acceptor levels.[39,40] Mg_{Ga} acceptor level in our spinel sample can be calculated as $E_{Mg_{Ga}} = E_g - E_{UV_{II}}$, where Eg is

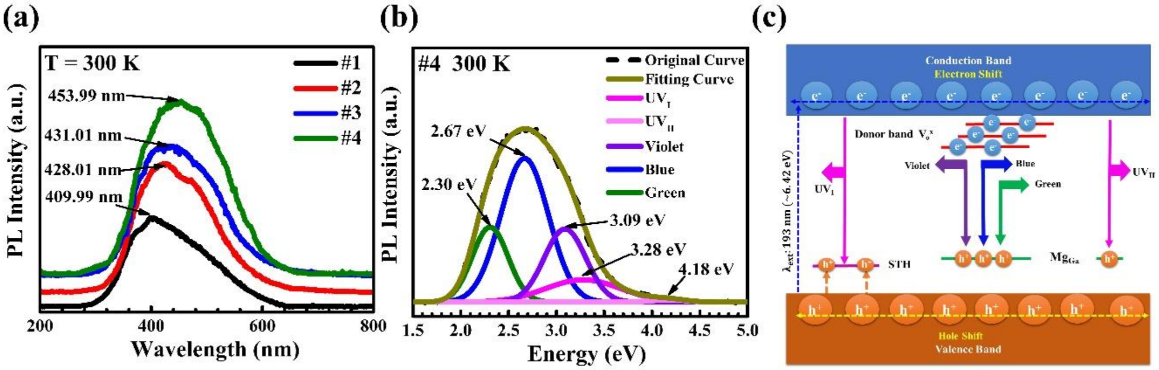

Figure 4.2 (a) Room temperature PL spectra of β-Ga_2O_3 and spinel $MgGa_2O_4$ samples. (b) PL peak deconvolution of sample #4. (c) Schematic energy level diagram illustrating optical transitions in spinel $MgGa_2O_4$.

the bandgap at room temperature of 5.41 eV, the UV_{II} emission energy $E_{UV_{II}}$ is 4.18 eV, so the $E_{Mg_{Ga}}$ was estimated as ~1.23 eV above the valence band for sample #4. The $E_{Mg_{Ga}}$ values for the other two $MgGa_2O_4$ samples 2 and 3 are also estimated as ~1.23, and 1.24 eV, respectively, which is close to theoretically calculated range of 1.0 to 1.5 eV.[29] In addition, three oxygen vacancy related donor defects levels in $MgGa_2O_4$ have been reported as that are in β-Ga_2O_3,[25,43] therefore, violet, blue and green emissions of spinel samples may be ascribed to the transition from the three oxygen vacancy donor bands to Mg_{Ga} antisite deep acceptor levels, respectively. Using similar donor-acceptor-pair (DAP) energy calculation in ZnO,[44] it leads to an estimation of three oxygen vacancy levels of 1.09, 1.51, and 1.88 eV below the conduction band minimum (CMB) edge for sample #4, respectively. For sample #2 and #3, the respective oxygen vacancy levels below the conduction band edge are 1.48, 1.76, and 2.01 eV, and 1.33, 1.55, and 1.80 eV. These values are not exactly the same but very similar to the reported oxygen vacancy levels in β-Ga_2O_3 namely 1.38, 1.56 and 1.76 eV below the CMB.[43] It should be noted that violet, blue and green emissions were previously designated from the optical transitions from oxygen vacancy donor bands to Ga or Mg vacancies acceptor levels in $MgGa_2O_4$ samples.[26,45] Nevertheless, by incorporating more Mg atoms into spinel $MgGa_2O_4$ through substrate temperature control, these excess Mg atoms with respect to the nominal value would go to Ga sites, namely, Mg_{Ga} antisites shall be the dominant acceptor states in our $MgGa_2O_4$ spinel samples, and these deep acceptors instead of Ga or Mg vacancies are assumed to have participated the observed visible transitions.

The β-Ga_2O_3 reference sample deconvoluted PL peaks are shown in **Figure S4.4(a)**, which are ~3.43 eV for UV_I emission, ~3.07 eV for violet, ~2.59 eV for blue, and ~2.35 eV for green emissions, respectively. An energy level diagram of the PL mechanism of β-Ga_2O_3 is illustrated as **Figure S4.4(b)**. The UV_I peak is ascribed to be the recombination between electrons in conduction band and holes bound to the STH energy level,[41] which is similar to the reported STH PL peak of Ga_2O_3 at 3.4 eV.[38] Thus, the E_{STH}^{bind} was calculated as ~0.49 eV.The violet, blue and green emissions are DAP transitions between oxygen vacancy donor bands and Ga vacancy/O vacancy defect complex ($V_{Ga\text{-}O}$) acceptor bands in Ga_2O_3.[43] Another UV peak (UV_{II}), which is related to $V_{Ga\text{-}O}$ defect complex, is observed at power-dependent and temperature-dependent PL in the Ga_2O_3 sample as shown later, is complementary with this designation.

4.3.3 Power dependent PL

Figure 4.3(a)-(d) show power dependent PL spectra of sample #1-#4 at 14 K with an excitation power density from 12.8 mW/cm^2 to 51.2 mW/cm^2. The PL peak position for all samples does not show obvious change as the incident power density changes. **Figure 4.3(e)-(h)** show integrated PL intensity of sample #1-#4 at 14 K against incident power density. The integrated PL intensity increases with the incident power density due to the increased numbers of pumped electrons, which exhibits similar nonlinear relationship trend.[46,47] The PL intensities increase more rapidly at lower incident power density ranges than higher power density, in other words, the power-dependent PL intensity tends to change less as the incident power increases for all samples, namely, it is becoming saturating. This reflects the fact that the dominating portions of the PL are from the visible emissions that are a result of DAP optical transitions. Since the number of these defects are fixed, thus the PL saturation effects would ultimately occur perhaps after larger excitation power is incident on the samples. It is also noted that besides the UV_I emission mentioned previously for sample #1, one UV_{II} emission located at ~282.71 nm emerges at 14 K, as shown in **Figure 4.3(a)**, and other temperatures as shown in **Figure 4.4(a)** later, which may be assigned to the recombination of electrons in conduction band and holes in defect complex acceptor level $V_{Ga\text{-}O}$ (**Figure S4.4(b)**). The estimated $V_{Ga\text{-}O}$ complex acceptor energy is ~4.39 eV below the conduction band, which is close to the reported value of ~4.42 eV below the conduction band.[43] With the $V_{Ga\text{-}O}$ energy and observed visible emission energies, the three oxygen vacancy deep donor levels are estimated as ~1.3, 1.8, and 2 eV below the conduction band edge. These numbers are in reasonable agreement with the reported values of β-Ga_2O_3.[43]

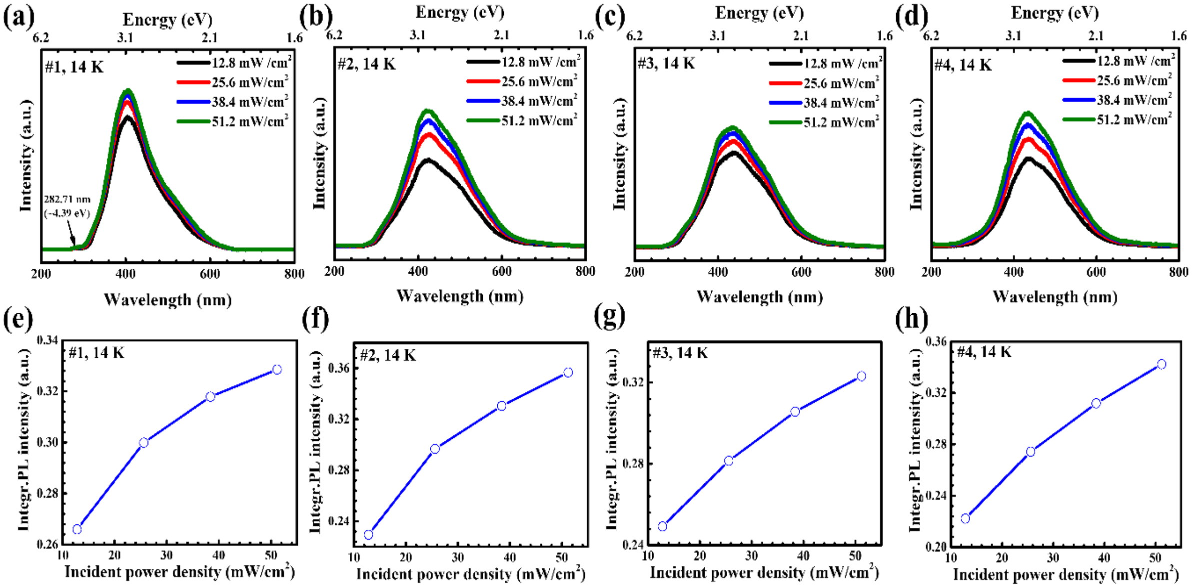

Figure 4.3 (a)-(d) Power dependent PL spectra of sample #1-#4, respectively. (e)-(h) Integrated PL intensity versus incident power density for sample #1-#4, respectively.

4.3.3 Temperature dependent PL

Figure 4.4(a)-(d) show temperature-dependent PL spectra of samples #1-#4, respectively. Temperature range is between 14 and 300 K, and incident lasing power density is 12.8 mW/cm^2. **Figure 4.4(e)-(h)** show integrated PL intensity as a function of temperature for the four samples, respectively. For sample #1, PL intensity decreases monotonically versus the temperature in both range of 14 – 40 K and 100 – 300 K , which is similar to the reported PL spectra trend of β-Ga_2O_3.[48] However, PL intensity increases with temperature in the range of 40 -100 K. Similarly, the PL intensity of three spinel $MgGa_2O_4$ samples first increases with temperature in range of 14 K to 150 K, and then decreases after 150 K until room temperature. At higher temperatures, the integrated PL intensity of all samples decreases as the increase of temperature, which is due to positive thermal quenching (PTQ) effect.[49,50] Similar phenomena were observed in other materials

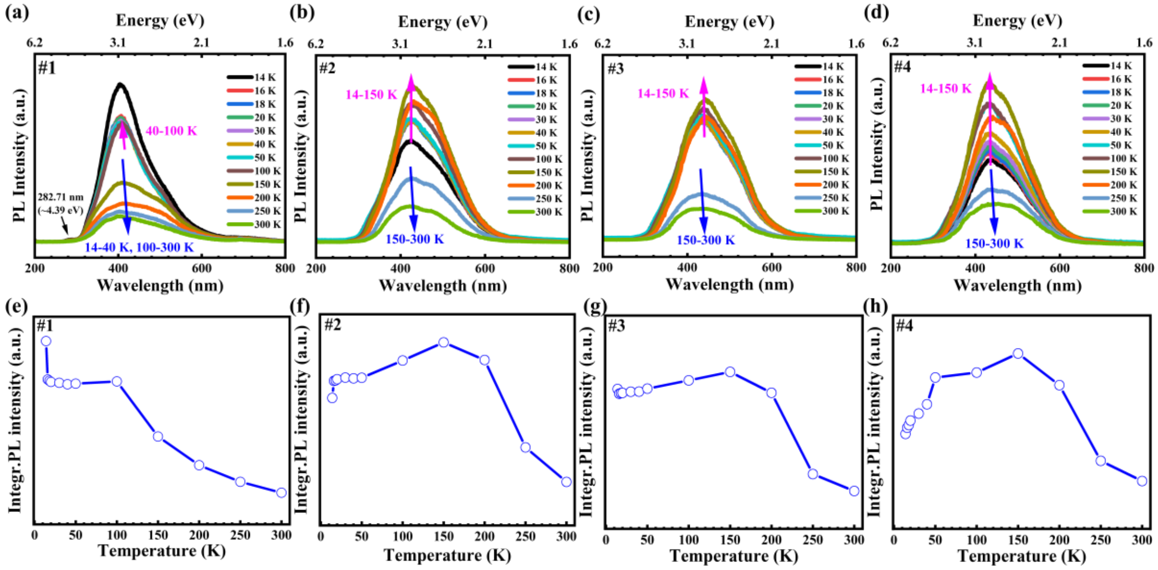

Figure 4.4 (a)-(d) Temperature dependent PL spectra of sample #1-#4, respectively. (e)-(f) Integrated PL intensity versus temperature for sample #1-#4, respectively.

including GaAs[50], ZnO nano rods[51] and GaSb[52]. At lower temperatures, the PL intensity increases with the increase of temperature in these samples, especially in spinel $MgGa_2O_4$ samples, which is due to the negative thermal quenching (NTQ) effect.[50–52] Based on the multi-level model proposed by Shibata et. al,[50,51] the relationship between PL intensity and temperature can be expressed as $I(T) = I(0)\frac{1+\sum_{q=1}^{w} D_q \exp\left(-E_q'/k_B T\right)}{1+\sum_{j=1}^{m} C_j \exp\left(-E_j/k_B T\right)}$, where k_B is the Boltzmann constant, T is the temperature, E_j (E_q') is activation energy, which plays a role in the decrease or increase of the PL intensity with temperature, respectively, and C_j (D_q) is the corresponding weight factor. In this equation, the denominator exponential item is related to the normal PTQ process, namely, as the temperature increases, the PL intensity decreases. This applies to most direct semiconductors in which there are few or none defect-related intermediate energy levels that also participate radiative recombination. On the other hand, the numerator exponential item is related to NTQ effect. The inclusion of this numerator term is related to the existence of intermediate energy levels which participate radiative recombination processes. The competition of the denominator and numerator terms leads to the above observed temperature-dependent PL. Therefore, the NTQ effect here is a direct proof of the PL mechanism in **Figure 4.2(c)**, where multiple energy levels in the forbidden gap, which are three oxygen vacancies donor bands, STH level and Mg on the Ga site Mg_{Ga} acceptor level, are involved in the PL emissions. To be more specific for both β-Ga_2O_3 and spinel $MgGa_2O_4$ samples, the electrons trapped in oxygen vacancy donor bands may be re-excited from lower energy levels to higher energy levels or the conduction band to enhance both UV and visible emissions when temperature is low. For higher temperatures, the non-radiative SRH process becomes more dominating, thus the temperature-dependent PL follows the normal PTQ trend.

4.4 Conclusion

In summary, UWBG semiconductors are essential materials for power electronics, deep-UV photonics, and other emerging applications. As one of these promising materials, epitaxial films of spinel $MgGa_2O_4$ were successfully achieved by MBE. The bandgap was determined to be approximately 5.4-5.5 eV, with high transparency (>90%) in the visible spectral range. The photoluminescence properties of $MgGa_2O_4$ were extensively studied, encompassing both power and temperature dependence analyses. The PL mechanisms were elucidated, highlighting transitions involving self-trapped holes, oxygen vacancy deep donors, and magnesium atoms on gallium site deep acceptors. On one hand, the findings underscore the feasibility of using MBE for the epitaxial growth of $MgGa_2O_4$ films, expanding the repertoire of techniques available for advancing its electronic and optoelectronic device functionalities. On the other hand, it contributes valuable insights into the optical behavior and native defects studies on $MgGa_2O_4$.

4.5 References

[1] I. Makkonen, E. Korhonen, V. Prozheeva, F. Tuomisto, *J. Phys.: Condens. Matter* **2016**, *28*, 224002.

[2] Z. Galazka, D. Klimm, K. Irmscher, R. Uecker, M. Pietsch, R. Bertram, M. Naumann, M. Albrecht, A. Kwasniewski, R. Schewski, M. Bickermann, *physica status solidi (a)* **2015**, *212*, 1455.

[3] E. Ş. Tüzemen, S. Eker, H. Kavak, R. Esen, *Applied Surface Science* **2009**, *255*, 6195.

[4] A. C. Saritha, M. R. Shijeesh, L. S. Vikas, R. R. Prabhu, M. K. Jayaraj, *J. Phys. D: Appl. Phys.* **2016**, *49*, 295105.

[5] W. Cheng, Y. He, R. Wei, L. Hu, W. Song, X. Zhu, Y. Sun, *Thin Solid Films* **2023**, *781*, 139986.

[6] J. Yang, Z. Yang, T. Meng, Y. Han, X. Wang, Q. Zhang, *physica status solidi (a)* **2016**, *213*, 1010.

[7] Z. Galazka, R. Uecker, D. Klimm, K. Irmscher, M. Pietsch, R. Schewski, M. Albrecht, A. Kwasniewski, S. Ganschow, D. Schulz, C. Guguschev, R. Bertram, M. Bickermann, R. Fornari, *physica status solidi (a)* **2014**, *211*, 66.

[8] Z. Galazka, S. Ganschow, K. Irmscher, D. Klimm, M. Albrecht, R. Schewski, M. Pietsch, T. Schulz, A. Dittmar, A. Kwasniewski, R. Grueneberg, S. B. Anooz, A. Popp, U. Juda, I. M. Hanke, T. Schroeder, M. Bickermann, *Progress in Crystal Growth and Characterization of Materials* **2021**, *67*, 100511.

[9] X. Zhao, W. Cui, Z. Wu, D. Guo, P. Li, Y. An, L. Li, W. Tang, *Journal of Elec Materi* **2017**, *46*, 2366.

[10] T. Yang, C. Shou, L. Xu, J. Tran, Y. He, Y. Li, P. Wei, J. Liu, *ACS Appl. Electron. Mater.* **2023**, *5*, 2122.

[11] C. Shou, T. Yang, A. Almujtabi, T. Yang, Y. Li, Q. S. Mahmud, M. Xu, J.-G. Zheng, J. Liu, *Applied Physics Letters* **2023**, *122*, 212101.

[12] T. Yang, C. Shou, A. Almujtabi, J. Tran, Q. Lin, Y. Li, Q. S. Mahmud, P. Wei, J. Liu, *ACS Appl. Opt. Mater.* **2023**, *1*, 1670.

[13] Q. Hou, K. Liu, X. Chen, J. Yang, Q. Ai, Z. Cheng, Y. Zhu, B. Li, L. Liu, D. Shen, *physica status solidi (RRL) – Rapid Research Letters* **2022**, *16*, 2200137.

[14] Q. Guo, J. Tetsuka, Z. Chen, M. Arita, K. Saito, T. Tanaka, *Optical Materials* **2023**, *143*, 114267.

[15] Q. Hou, K. Liu, D. Han, Y. Zhu, X. Chen, B. Li, L. Liu, D. Shen, *Applied Physics Letters* **2022**, *120*, 011101.

[16] B. Thielert, C. Janowitz, Z. Galazka, M. Mulazzi, *Phys. Rev. B* **2018**, *97*, 235309.

[17] C. Hirschle, J. Schreuer, Z. Galazka, *Journal of Applied Physics* **2018**, *124*, 065111.

[18] S. Choi, K. Kim, Y.-M. Moon, B.-Y. Park, H.-K. Jung, *Materials Research Bulletin* **2010**, *45*, 979.

[19] A. Luchechko, O. Kravets, L. Kostyk, O. Tsvetkova, *Radiation Measurements* **2016**, *90*, 47.

[20] B.-S. Tsai, Y.-H. Chang, Y.-C. Chen, *Journal of Materials Research* **2004**, *19*, 1504.

[21] A. Mondal, J. Manam, *ECS J. Solid State Sci. Technol.* **2017**, *6*, R88.

[22] Simultaneous NIR photoluminescence and mechanoluminescence from Cr^{3+} activated $MgGa_2O_4$ phosphors with multifunctions for optical sensing - Journal of Materials Chemistry C (RSC Publishing) DOI:10.1039/D4TC00059E, https://pubs.rsc.org/en/content/articlehtml/2024/tc/d4tc00059e, accessed: Feb., 2024.

[23] A. Mondal, S. Das, J. Manam, *RSC Adv.* **2016**, *6*, 82484.

[24] G. Zhang, A. Goldstein, Y. Wu, *J Adv Ceram* **2022**, *11*, 470.

[25] D. V. Mlotswa, L. L. Noto, S. J. Mofokeng, K. O. Obodo, V. R. Orante-Barrón, B. M. Mothudi, *Optical Materials* **2020**, *109*, 110134.

[26] Z. Liu, P. Hu, X. Jing, L. Wang, *J. Electrochem. Soc.* **2008**, *156*, H43.

[27] R. Jangir, S. Porwal, P. Tiwari, P. Mondal, S. K. Rai, A. K. Srivastava, I. Bhaumik, T. Ganguli, *AIP Advances* **2016**, *6*, 035120.

[28] K. Zhang, Z. Xu, S. Zhang, H. Wang, H. Cheng, J. Hao, J. Wu, F. Fang, *Physica B: Condensed Matter* **2021**, *600*, 412624.

[29] K. Zhang, Z. Xu, J. Zhao, H. Wang, J. Hao, S. Zhang, H. Cheng, B. Dong, *Journal of Alloys and Compounds* **2021**, *881*, 160665.

[30] B. A. Scott, K. H. Nichols, R. M. Potemski, J. M. Woodall, *Applied Physics Letters* **1972**, *21*, 121.

[31] X. Yu, X. Yang, J. Huan, J. Tong, Y. Qiao, J. Xing, Z. Zhang, J. Zhao, **2024**, DOI: 10.2139/ssrn.4714049.

[32] G. Katz, R. Roy, *Journal of Crystal Growth* **1970**, *6*, 221.

[33] A. Luchechko, O. Kravets, *physica status solidi c* **2017**, *14*, 1600146.

[34] T. Suzuki, M. Hughes, Y. Ohishi, *Journal of Luminescence* **2010**, *130*, 121.

[35] M. A. Hamid, B. Samuels, S. Karmakar, M. A. Halim, I. H. Emu, P. K. Sarkar, M. F. N. Taufique, A. Haque, R. Droopad, *Journal of Alloys and Compounds* **2024**, *972*, 172807.

[36] G. Pilania, V. Kocevski, J. A. Valdez, C. R. Kreller, B. P. Uberuaga, *Commun Mater* **2020**, *1*, 1.

[37] Y. K. Frodason, K. M. Johansen, L. Vines, J. B. Varley, *Journal of Applied Physics* **2020**, *127*, 075701.

[38] S. Marcinkevičius, J. S. Speck, *Applied Physics Letters* **2020**, *116*, 132101.

[39] T. Gake, Y. Kumagai, F. Oba, *Phys. Rev. Mater.* **2019**, *3*, 044603.

[40] J. L. Lyons, A. Janotti, C. G. Van de Walle, *Journal of Applied Physics* **2014**, *115*, 012014.

[41] Y. Wang, P. T. Dickens, J. B. Varley, X. Ni, E. Lotubai, S. Sprawls, F. Liu, V. Lordi, S. Krishnamoorthy, S. Blair, K. G. Lynn, M. Scarpulla, B. Sensale-Rodriguez, *Sci Rep* **2018**, *8*, 18075.

[42] J. B. Varley, A. Janotti, C. Franchini, C. G. Van de Walle, *Phys. Rev. B* **2012**, *85*, 081109.

[43] X. Zhu, Y.-W. Zhang, S.-N. Zhang, X.-Q. Huo, X.-H. Zhang, Z.-Q. Li, *Journal of Luminescence* **2022**, *246*, 118801.

[44] F. X. Xiu, Z. Yang, L. J. Mandalapu, D. T. Zhao, J. L. Liu, W. P. Beyermann, *Applied Physics Letters* **2005**, *87*, 152101.

[45] B. Jiang, F. Chi, X. Wei, Y. Chen, M. Yin, *Journal of Applied Physics* **2018**, *124*, 063101.

[46] A. Sabbar, S. Madhusoodhanan, S. Al-Kabi, B. Dong, J. Wang, S. Atcitty, R. Kaplar, D. Ding, A. Mantooth, S.-Q. Yu, Z. Chen, *Sci Rep* **2019**, *9*, 16758.

[47] J. B. Cui, M. A. Thomas, *Journal of Applied Physics* **2009**, *106*, 033518.

[48] D. Hu, S. Zhuang, Z. Ma, X. Dong, G. Du, B. Zhang, Y. Zhang, J. Yin, *J Mater Sci: Mater Electron* **2017**, *28*, 10997.

[49] V. A. Fonoberov, K. A. Alim, A. A. Balandin, F. Xiu, J. Liu, *Phys. Rev. B* **2006**, *73*, 165317.

[50] H. Shibata, *Jpn. J. Appl. Phys.* **1998**, *37*, 550.

[51] Y. Wu, J. Li, H. Ding, Z. Gao, Y. Wu, N. Pan, X. Wang, *Phys. Chem. Chem. Phys.* **2015**, *17*, 5360.

[52] J. H. Park, T. K. Lee, Y. K. Noh, M. D. Kim, E. Oh, *Journal of Applied Physics* **2009**, *105*, 043516.

Supporting Information

1. Reference sample and substrate temperature dependent spinel sample growth conditions, and characterization parameters

Table S4.1 Growth condition of β-Ga_2O_3 and spinel $MgGa_2O_4$ films with different substrate temperatures.

Sample Index	**Growth conditions**						**Film thickness (nm)**	**Atomic percent by EDX (%)**			**Bandgap (eV)**
	Mg (°C)	**Ga (°C)**	**O_2 (sccm)**	**Growth temperature (°C)**	**Growth time (h)**	**RF (w)**		**Mg**	**Ga**	**O**	
#1	-	750	2.0	600	5	400	364.35	-	40.05	59.95	5.02
#2	410	750	2.0	400	5	400	981.18	15.26	27.71	57.03	5.52
#3	410	750	2.0	500	5	400	1122.36	14.62	27.60	57.78	5.47
#4	410	750	2.0	600	5	400	1217.86	14.25	28.58	57.17	5.41

2. SEM cross-section and surface morphology

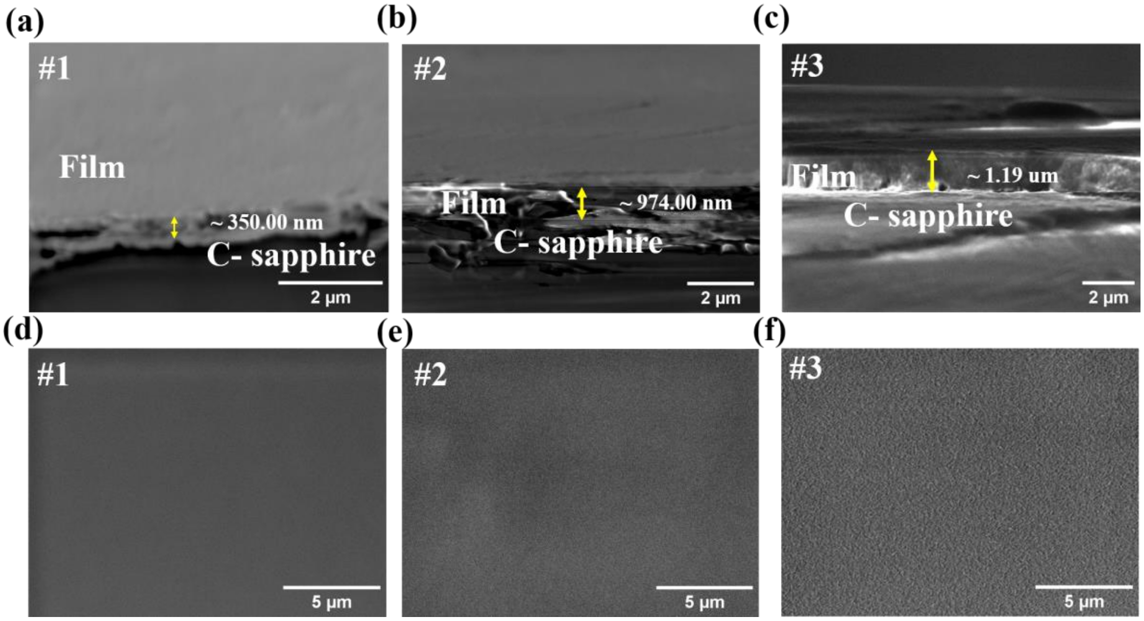

Figure S4.1 (a)-(c) SEM cross-section image of β-Ga_2O_3, and spinel $MgGa_2O_4$ grown at 400ºC and 500ºC, respectively. (d)-(f) SEM surface morphology image of β-Ga_2O_3, and spinel $MgGa_2O_4$ grown at 400ºC and 500ºC, respectively.

3. Thickness dependent growth conditions of sample #04 and structure properties characterization

Table S4.2 Growth condition of $MgGa_2O_4$ films with different thickness for sample #4.

Sample Index	Growth conditions						Film thickness (nm)
	Mg (°C)	Ga (°C)	O_2 (sccm)	Growth temperature (°C)	RF (w)	Growth time (h)	
#4	410	750	2.0	600	400	5	1217.86
#4’	410	750	2.0	600	400	30 min	44.00
#4”	410	750	2.0	600	400	9 min	13.20

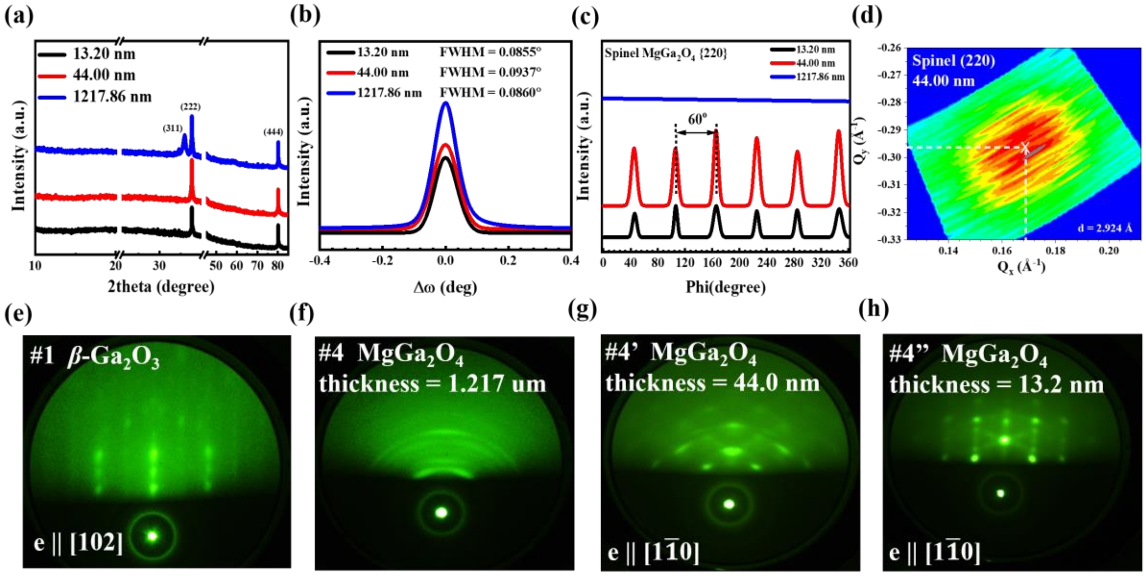

Figure S4.2 (a) XRD patterns in theta-2theta scan mode. (b) Rocking curves. (c) XRD phi scan patterns of spinel $MgGa_2O_4$ {220} planes grown with thickness of 13.20, 44.00 and 1217.86 nm. (d) In-plane reciprocal space mapping of spinel (220) for sample with thickness of 44.00 nm. RHEED images of (e) sample #1, (f) sample #4, (g) sample #4’, (h) sample #4”.

To further investigate the crystallinity of spinel $MgGa_2O_4$ thin films on c-sapphire substrate, film thickness dependent growth for sample #4 was performed. As listed in **Table S2**, reducing growth time from 5 h of sample 4 to 30 min and 9 min led to sample #4’ of 44.00 nm and sample #4” of 13.20 nm, respectively. **Figure S2(a)** shows XRD pattern in $\theta/2\theta$ scan mode, compared to (311), (222) and (444) diffraction peak of sample #4, only (222) and (444) peak emerge for the two thinner films, indicating that the film changes from single crystal to polycrystal nature with increasing film thickness, which may be ascribed to strain relaxation resulted from film thickness increase.[1,2] **Figure S2(b)** shows normalized XRD rocking curves for spinel $MgGa_2O_4$ (222) peak. The FWHM of sample #4’ and #4” are recorded as 0.0937˚ and 0.0860˚, respectively. To confirm the change from single crystal to polycrystal as a result of film thickness increase, XRD φ-scans were measured. **Figure S2(c)** shows φ-scan patterns of spinel {220} of all three samples at a position of the detector 2theta_chi = 30.506° (PDF 00-010-0133). Both sample #4’ and #4” reveal the six-fold rotational symmetry,[3] while sample #4 doesn’t show any peak due to its polycrystal nature. To further extract the lattice constant, **Figure S2(d)** shows in-plane RSM of (220) plane for sample #4’. The extracted d-spacing value of (220) plane is ~2.926 Å, so the spinel phase lattice constant a_{spinel} is $2\sqrt{2}d_{(220)}$, which is ~8.270 Å. As an alternative and viable way to confirm the crystallinity and extract lattice constant of films, reflection high energy electron diffraction (RHEED) characterizations were performed. **Figure S2(e)** shows the streaky-like patterns of β-phase $\{\bar{2}01\}$ plane along [102] azimuth of sample #1, indicating high crystallinity of the films, which are similar to previous RHEED patterns obtained from β-Ga_2O_3.[4,5] **Figure S2(f)** shows RHEED pattern of sample #4. The Debye ring indicates its polycrystal nature. With decreasing film thickness, the streaky-like patterns of $MgGa_2O_4$ spinel {111} plane along $[1\bar{1}0]$ azimuth become clearer, which is shown in **Figure S2(g)-(h)**, confirming single crystallinity of thinner $MgGa_2O_4$ films. The extracted in-plane lattice constant $a_{||[1\bar{1}0]}$ was calculated as 6.75 Å, so the lattice constant a_{spinel} was calculated as $a_{||[1\bar{1}0]}$ / ($\sqrt{3/2}$), which is ~8.270 Å. Therefore, all lattice constants extracted from XRD θ/2θ scan, in-plane RSM and RHEED confirm the spinel structure of $MgGa_2O_4$ samples.

4. RT Peak deconvolution of sample #2 and #3

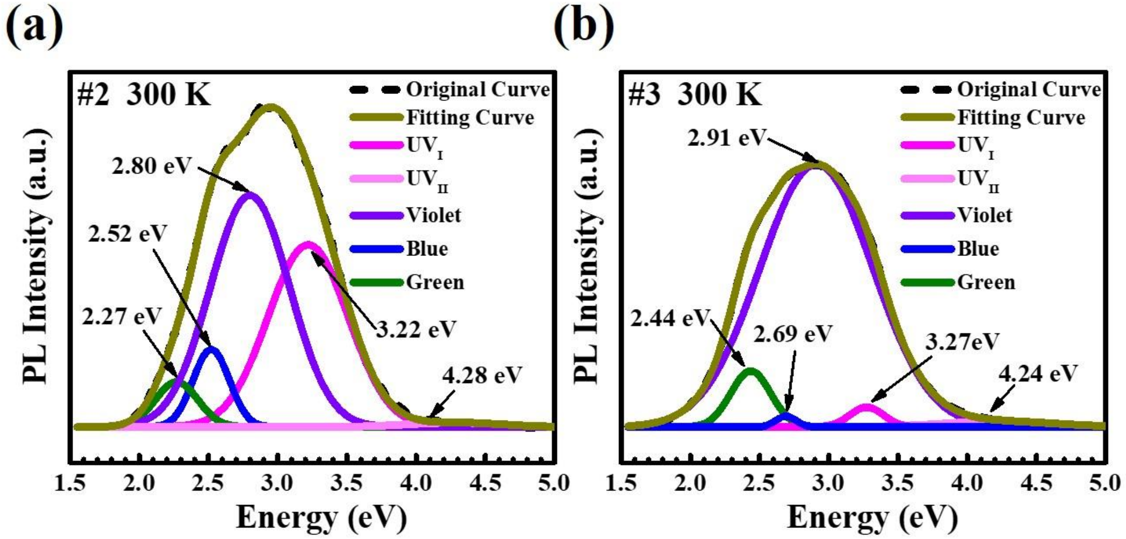

Figure S4.3 (a) –(b) Room temperature PL peak deconvolution of sample #2 and #3, respectively.

5. PL mechanism schematic of β-Ga_2O_3

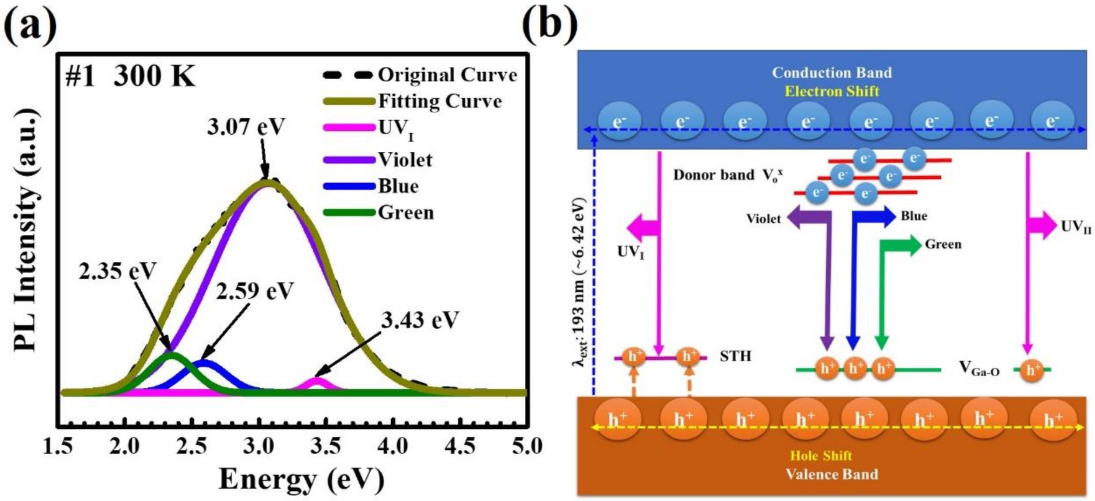

Figure S4.4 (a) Room temperature PL peak deconvolution of β-Ga_2O_3 sample #1. (b) Energy level diagram of the PL mechanism of β-Ga_2O_3.

6. References

[1] D. J. Dunstan, **n.d.**

[2] T. L. Meyer, L. Jiang, S. Park, T. Egami, H. N. Lee, *APL Materials* **2015**, *3*, 126102.

[3] M. A. Hamid, B. Samuels, S. Karmakar, M. A. Halim, I. H. Emu, P. K. Sarkar, M. F. N. Taufique, A. Haque, R. Droopad, *Journal of Alloys and Compounds* **2024**, *972*, 172807.

[4] T. Yang, C. Shou, L. Xu, J. Tran, Y. He, Y. Li, P. Wei, J. Liu, *ACS Appl. Electron. Mater.* **2023**, *5*, 2122.

[5] T. Yang, C. Shou, A. Almujtabi, J. Tran, Q. Lin, Y. Li, Q. S. Mahmud, P. Wei, J. Liu, *ACS Appl. Opt. Mater.* **2023**, *1*, 1670.

Chapter 5: Beta to spinel phase transition of magnesium gallium oxide thin films and their photoluminescence properties

5.1 Introduction

As one of the most promising ultra-wide bandgap (UWBG) semiconductor materials, β-Ga_2O_3 has gained significant popularity in high-performance power electronic and optoelectronic devices.[1–3] The critical electric field of ~8 MV/cm allows for its applications in high-power diodes and field-effect transistors.[4–6] Additionally, its large bandgap energy enables deep ultraviolet (UV) optoelectronic device applications.[7,8] To extend the applications of Ga_2O_3-based devices beyond the beta phase structure, bandgap engineering through Mg incorporation is highly desirable.[9–13] Both amorphous MgGaO[9,10] and β-MgGaO[11,13] have been reported for deep UV photodetector applications. Previously, we confirmed that the MgGaO lattice structure transforms from beta phase to beta and rocksalt mixed phase, and finally to rocksalt phase as the normalized cations Mg at.%/Ga at.% change from 0%/100% to 100%/0%. [12] However, the interval of Mg and Ga composition change in the above study was a bit too big, normalized cations Mg at.%/Ga at.% were not tuned to be around 33.33%/66.67%, which could lead to the spinel $MgGa_2O_4$ phase, a promising transparent semiconducting [14,15] for optoelectronic and power electronic applications.[16] In addition, careful tuning Mg compositions within 33.33% in MgGaO may lead to a transition between β phase and spinel phase, which was not explored in the previous study [12] and remains unknown. Furthermore, there is a lack of comprehensive photoluminescence (PL) studies of β-MgGaO and spinel $MgGa_2O_4$ thin films, although several room temperature [17–20] and a few temperature-dependent[21] PL studies of Mg-doped β-Ga_2O_3 were conducted, and preliminary room temperature PL studies of $MgGa_2O_4$ were reported.[22,23]

To refine the phase transition conditions from β-MgGaO to spinel $MgGa_2O_4$ and to investigate the PL mechanism of MgGaO films with varying Mg atomic percentages, this study involves the growth of nine MgGaO thin film samples with Mg atomic percentages ranging from 0 to 15.26% (normalized across all Mg, Ga, and O elements in the alloys) using plasma-assisted molecular beam epitaxy (MBE). The structural transformation, film quality, lattice parameters, optical bandgap, and transmittance properties were examined. Additionally, comprehensive PL studies of these MgGaO thin films including power and temperature-dependent PL measurements were carried out.

5.2 Experimental Details

5.2.1 Film growth

An SVT Associates MBE system with a base pressure of 10^{-9} torr was used to grow MgGaO samples. 2-inch c-plane sapphire wafers were used as substrates. The substrate was cleaned by using a piranha solution (H_2O_2: H_2SO_4 = 3:5) at 200 °C for approximately 20 minutes. Subsequently, the substrate was rinsed in deionized water, blown-dry with a nitrogen gun, and transferred to the MBE load-lock chamber. After the pressure of the load-lock chamber was reduced better than approximately 10^{-6} torr, the substrate was finally transferred to the substrate holder in the main chamber. The substrate temperature was raised by a heater placed behind the substrate and a pre-growth substrate annealing process was conducted at 800 °C for 20 minutes. The substrate temperature was then reduced to

600 °C for sample growth. During the growth, oxygen was introduced at a rate of 2.0 sccm using an RF plasma at 400 W. Elemental high-purity Ga (6N) effusion cell temperature was maintained at 750 °C and Mg (4N) effusion cell temperature was varied from 390 to 423 °C, resulting in the growth of nine MgGaO thin film samples with different Mg atomic percentages. The growth for each sample lasted 5 hours. Following growth, a post-annealing process was conducted at 700 °C for 20 minutes without an oxygen atmosphere.

5.2.2 Film characterizations

The film thickness of the samples, as listed in **Table 5.1** of the supporting information, was measured using a Veeco Dektak 8 profilometer. The relative atomic ratios of Mg, Ga, and O in all samples were determined by energy-dispersive X-ray (EDX) analysis using a TESCAN Vega3 SBH scanning electron microscope (SEM). The film structure, quality, and lattice parameters were characterized by x-ray diffraction (XRD) techniques, including theta/2theta scans, rocking curves, in-plane phi scans, and reciprocal space mapping (RSM), using a Bruker D8 Advance X-ray diffractometer and a Rigaku SmartLab X-ray diffractometer with Cu Kα radiation ($\lambda = 1.5405$ Å) at room temperature. Absorption and transmittance spectra were measured at room temperature with a high-performance UV-Vis-NIR spectrophotometer (Cary 5000, Agilent Inc.). Power and temperature-dependent PL spectra were obtained using a custom-built PL system equipped with a 193-nm ArF excimer laser (Coherent Inc.) and a helium compressor (SHI-APD Cryogenics Inc.). The laser, operating in constant energy mode, allowed for varying incident power densities by adjusting the energy values of the beam through a constant beam area defined by the beam slit. Temperature control of PL from 14 to 300 K was used.

5.3 Results and Discussion

5.3.1 Film growth and characterizations

Table 5.2 Characterized parameters of 9 MgGaO thin films with Mg at.% from 0% to 15.26%.

Sample index	Film thickness (nm)	Relative atomic percent (EDX)			Chemical formula	Phase identification	Bandgap (eV)
		Mg%	Ga%	O%			
#1	364.35	0	40.05	59.95	Ga_2O_3	*β*-phase	5.02
#2	379.97	2.89	37.28	59.83	$(Mg_{0.07}Ga_{0.93})_2O_3$		5.08
#3	397.01	4.05	35.84	60.10	$(Mg_{0.1}Ga_{0.9})_2O_3$		5.11
#4	665.70	6.71	33.93	59.36	$Mg_{0.067}Ga_{0.339}O_{0.594}$	Mixed phase	4.86
#5	744.52	7.42	33.45	59.13	$Mg_{0.074}Ga_{0.335}O_{0.591}$		4.88
#6	1319.69	12.04	30.24	57.72	$Mg_{0.12}Ga_{0.30}O_{0.58}$		5.35
#7	1137.10	13.31	28.91	57.78	$Mg_{0.92}Ga_{2.00}O_4$	Spinel phase	5.38
#8	1224.85	14.04	28.44	57.52	$Mg_{0.97}Ga_{1.98}O_4$		5.43
#9	1203.95	15.26	27.71	57.03	$Mg_{1.07}Ga_{1.94}O_4$		5.45

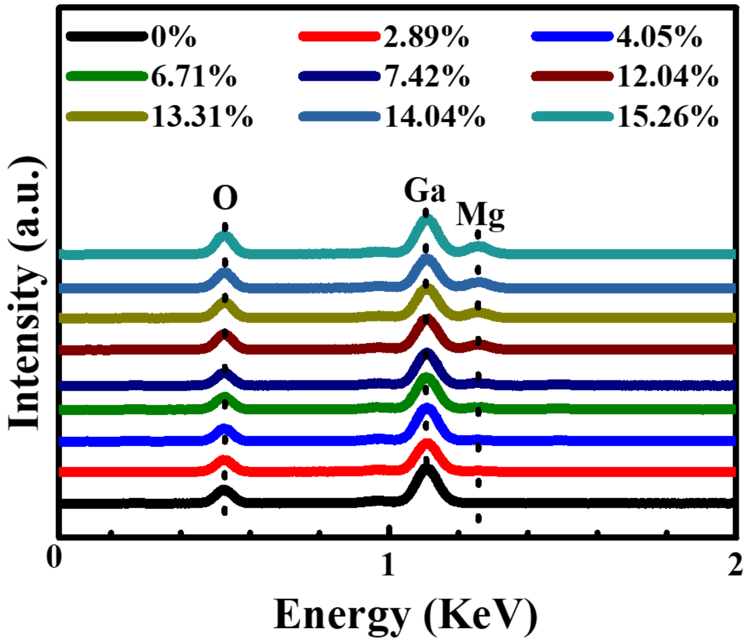

Figure 5.1 EDX spectra of MgGaO thin films of different Mg atomic percent.

Figure 5.1 shows EDX spectra of all MgGaO thin films. The O kα, Ga Lα and Mg Kα peaks are located at approximately 0.525, 1.098 and 1.253 keV,[12,13,15] respectively. Due to the substantial film thickness, the Al signal from the substrate is undetectable. Based on the integrated area of the peaks, the elemental compositions are obtained as listed in **Table S5.1** in the supporting information. The Mg at.% increases monotonically from 0% to 15.26% across samples #1 to #9.

Figure 5.2(a) depicts the schematics of lattice structures of β-MgGaO and spinel $MgGa_2O_4$ grown on c-sapphire substrate, where the β phase {$\bar{2}$01} planes and spinel phase {111} planes epitaxially align along c-sapphire [0001] orientation. **Figure 5.2(b)** shows XRD pattern of all MgGaO samples obtained through theta/2theta scanning. Samples #1-#3, with Mg atomic percentages ranging from 0 to 4.05%, exhibit pure β phase. According

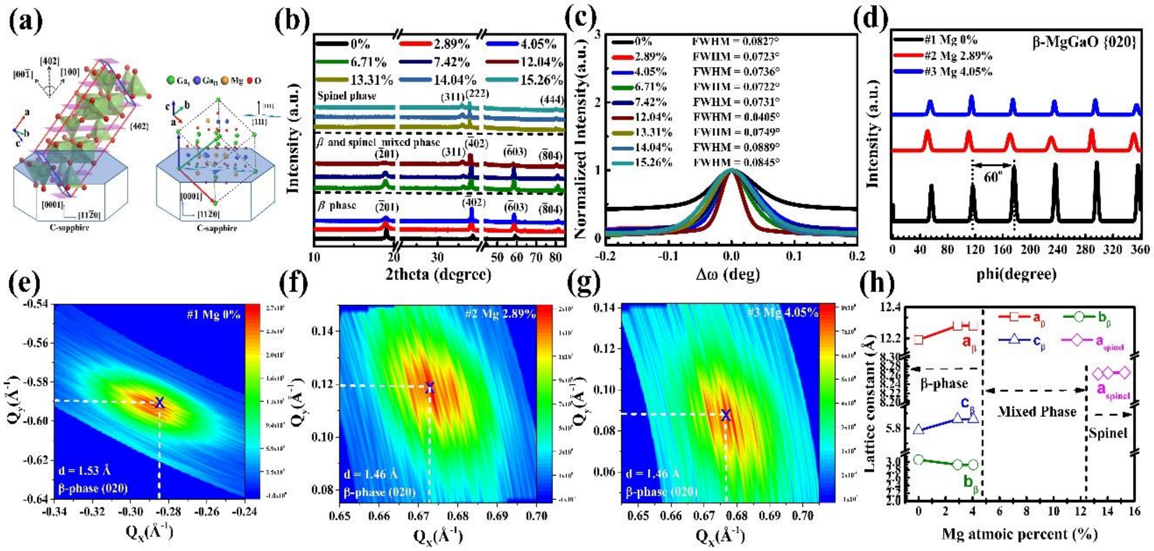

Figure 5.2 (a) Schematic of lattice structures of MgGaO films in both β and spinel phases grown on c-sapphire. (b) XRD patterns of MgGaO films with various Mg atomic percentages in theta-2theta scans. (c) Normalized XRD rocking curves. (d) φ-scan patterns of β-MgGaO {020} plane. (e)-(g) In-plane RSM of samples #1-#3 of the β phase (020). (h) β phase lattice constant $a_β$, $b_β$, $c_β$ and spinel phase lattice constant a_{spinel} versus Mg atomic percentage.

to Ga_2O_3 PDF 01-087-1901, four distinct diffraction peaks are observed at approximately 19.12 °, 38.50 °, 59.14 ° and 82.37°, corresponding to the β-phase $(\bar{2}01)$, $(\bar{4}02)$, $(\bar{6}03)$, and $(\bar{8}04)$,[24–26] respectively, indicating a clear monoclinic structure. The chemical formula for films in β phase can be expressed as $(Mg_xGa_{1-x})_2O_3$ (**Table 5.1**). Taking sample #2 as an example, its formula can be expressed as $(Mg_{0.07}Ga_{0.93})_2O_3$. On the other hand, according to $MgGa_2O_4$ PDF 00-010-0133, samples #7-#9, with Mg atomic percentages between 13.31 and 15.26%, displays a pure spinel phase with diffraction peaks at approximately 35.93 °, 37.59 °, and 80.24 °, corresponding to the spinel-phase (311), (222) and (444),[27,28] respectively. The existence of (222) and (444) but lack of (111) and (333) diffraction peaks is due to the XRD selection rule for face-centered cubic (fcc) nature of the spinel structure, which consists of 8 fcc units in each unit cell. The chemical formula for films in spinel phase can be expressed as $Mg_xGa_yO_4$, where x and y is close to 1 and 2, respectively (**Table 5.1**). For example, chemical formula of sample #9 can be expressed as $\sim Mg_{1.07}Ga_{1.94}O_4$. Samples #4-#6, with Mg atomic percentages from 6.71 to 12.04 %, exhibit a mixed phase of β and spinel, as evidenced by the presence of both β phase $(\bar{2}01)$, $(\bar{4}02)$, $(\bar{6}03)$ and $(\bar{8}04)$ peaks and the spinel phase (311) peak in the XRD pattern. The chemical formula in this region can be expressed as $Mg_xGa_yO_z$ (**Table 5.1**). For example, chemical formula of sample #6 can be written as $Mg_{0.12}Ga_{0.30}O_{0.58}$. Furthermore, as the Mg composition increases, the diffraction angles decrease due to the larger ionic radius of Mg (0.72 Å) compared to Ga (0.62 Å) in both β and mixed phases.[12,13,29] The 2theta positions of $(\bar{4}02)$ peak for the β phase and mixed phase, as well as (222) peak for the spinel phase, are summarized in **Table S5.1** in the supporting information. **Figure 5.2(c)** shows normalized

XRD rocking curves of $(\bar{4}02)$ and (222) peaks for β-phase and β/spinel mixed phase, and spinel phase samples, respectively. The full width at half maximum (FWHM) values for β phase samples #1-#3 are 0.0827°, 0.0732°, and 0.0736°; for mixed phase samples #4-#6, they are 0.0722°, 0.0731°, and 0.0405°; and for spinel samples #7-#9, they are 0.0749°, 0.0889°, and 0.0845°, respectively. These low FWHM values indicate the high quality of our films.[12,13] Given the single-phase nature of β phase films, **Figure 5.2(d)** shows β-MgGaO {020} φ-scan patterns for samples #1-#3 at a 2theta_chi detector position of 60.961° (PDF 01-087-1901). Consistent with previously reported β-Ga_2O_3[30,31] and β-MgGaO[12] {020} φ-scan patterns, all three films exhibit a six-fold rotational symmetry.

Lattice constants a_β and c_β of β-phase samples can be obtained from the XRD pattern in theta/2thta scan mode in **Figure 5.2(b)**, while b_β of these β phase samples were obtained by in-plane reciprocal space mapping (RSM) of the β phase (020) plane, which are shown

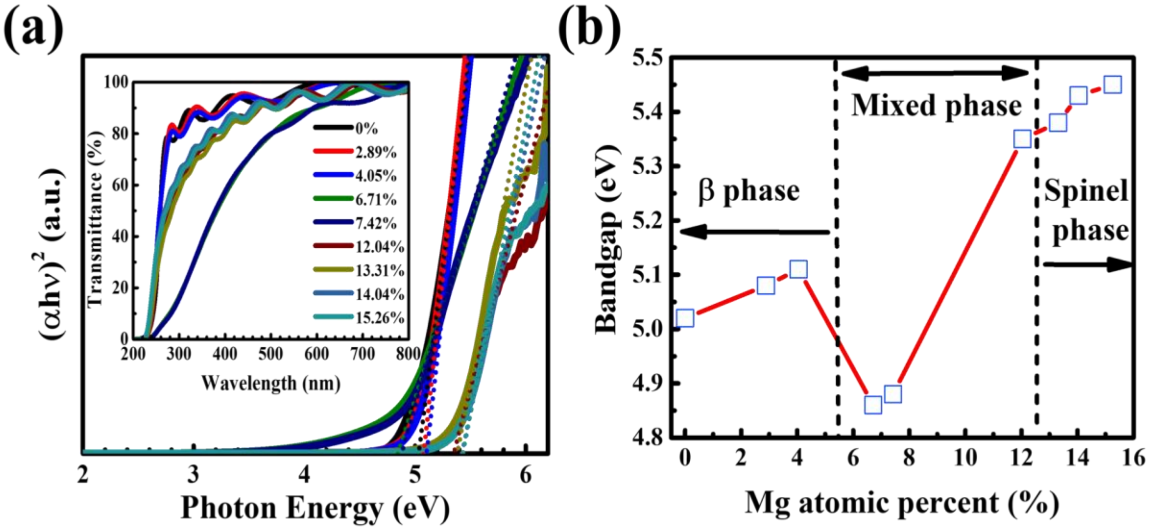

Figure 5.3 (a) Tauc plot absorption spectra, with an inset showing the corresponding transmittance spectra. (b) The relationship between the bandgap and Mg atomic percentage across various MgGaO samples.

in **Figures 5.2(e)-(g)**, respectively. Specifically, we derived the interplanar distance $d_{(\bar{4}02)}$ of the β-phase samples by applying Bragg's law. Then, we utilized established equations from prior studies[12] to calculate the lattice constants a_β and c_β. From RSM results in **Figures 5.2(e)-(g)**, the interplanar distance $d_{(020)}$ is obtained, from which the lattice constant b_β of β-phase samples is calculated as twice $d_{(020)}$. Similarly, we obtained the interplanar distance $d_{(222)}$ for the pure spinel samples from XRD theta/2theta scan patterns, enabling the calculation of the lattice constant a_{spinel} as $2\sqrt{3}d_{(222)}$. These lattice constant values are listed in **Table S5.1** in the supporting information. **Figure 5.2(h)** shows the lattice constants as a function of Mg atomic percentage. In β-phase MgGaO samples, both a_β and c_β increase, while b_β decreases with increasing Mg at.%, compared to the reference values of β-Ga_2O_3, which are approximately 12.20 Å, 5.799 Å, and 3.04 Å, respectively (β-Ga_2O_3 PDF 01-087-1901). In spinel-phase $MgGa_2O_4$ samples, the lattice constant a_{spinel} shows a slight increase with the increase of the Mg atomic percentage, compared with a reference value of approximately 8.288 Å ($MgGa_2O_4$ PDF 00-010-0133).

Figure 5.3(a) shows absorption spectra of all samples in Tauc plot. Both β-MgGaO[11–13,32,33] and spinel $MgGa_2O_4$[14,15,34] were acknowledged as direct bandgap semiconductors. Implicit in this analysis is the assumption that their ternary alloy, the mixed phase MgGaO, likewise conforms to this intrinsic property. Employing the Tauc equation $(\alpha h\upsilon)^2 = A(h\upsilon - E_g)$, wherein hυ signifies energy, α denotes the absorption coefficient, and A represents a constant, the bandgap $E_g\, is$ discerned. This determination involved extrapolating the linear portion of the absorption spectra to intersect the hν-axis through linear regression, as documented in **Table 1**. The inset of **Figure 5.3(a)** shows transmittance spectra, manifesting a discernible reduction in light transmittance from approximately 90% in the beta phase to a range of 60%-80% in the mixed phase, followed by an ascent to approximately 80% in the spinel phase, spanning the visible spectrum. **Figure 5.3(b)** shows a graphical representation of the bandgap modulation with varying

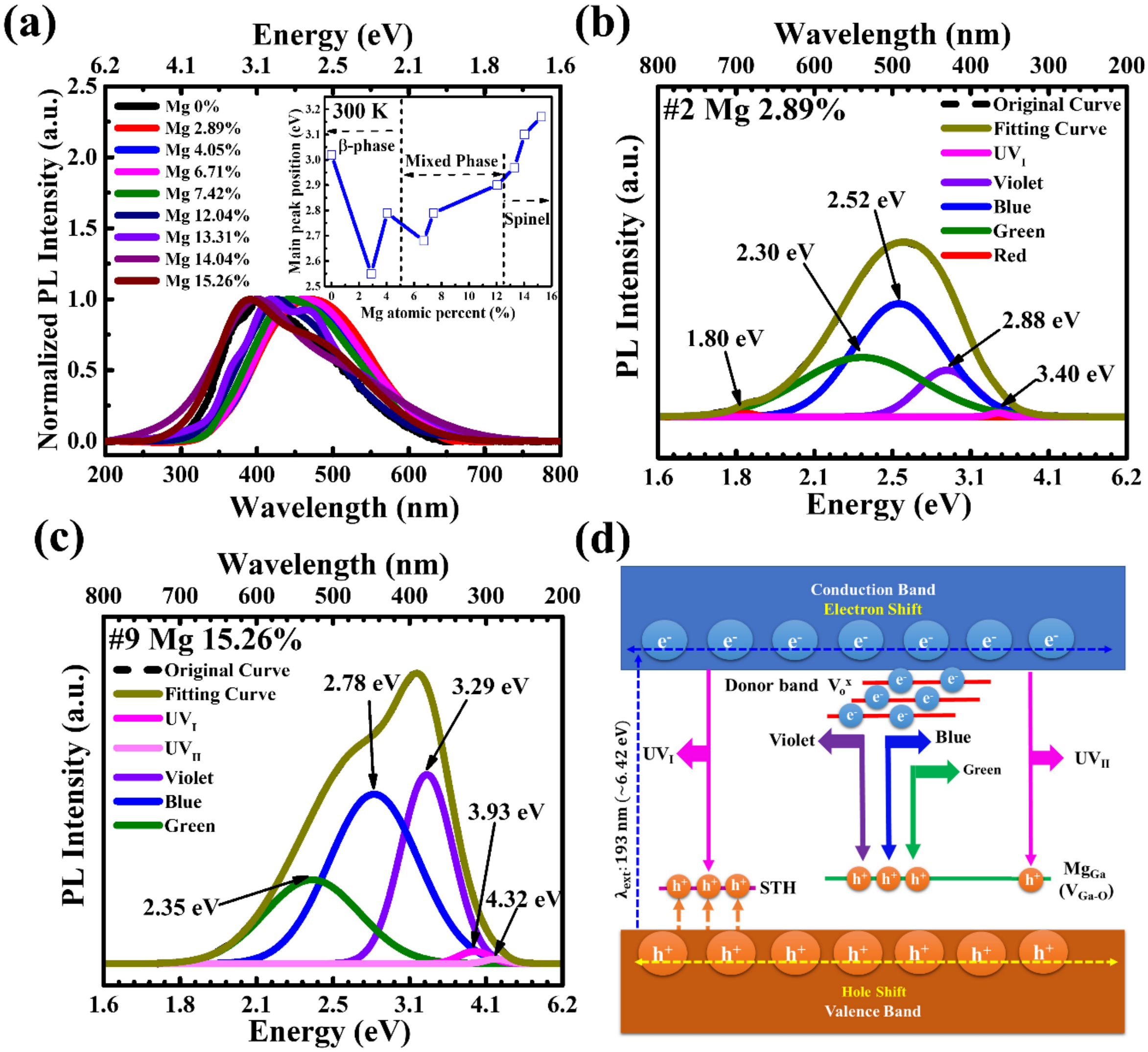

Figure 5.4 (a) Normalized PL spectra of all samples at room temperature (inset is the PL main peak position versus Mg atomic percent). (b)-(c) PL deconvolution for sample #2 in beta phase and #9 in spinel phase, respectively. (d) Schematic energy level diagram illustrating optical transitions in both beta and spinel MgGaO.

Mg composition in MgGaO films. It is noted that the bandgap exhibits a consistent augmentation with escalating Mg atomic percentages in both the beta phase and the transition from mixed to spinel phases. Nevertheless, a conspicuous decline in bandgap transpires from the beta to the mixed phase, ostensibly attributed to the abrupt emergence of the spinel phase characterized by a diminished bandgap. This decline, from 5.11 eV to 4.86 eV, underscores the discernible influence of the spinel phase in attenuating the comparatively larger bandgap intrinsic to the beta phase.

5.3.2 Room temperature PL

Figure 5.4(a) shows normalized room temperature (RT) PL spectra of all samples, which were acquired at an incident power density of 12.8 mW/cm². Analogous to RT PL spectra observed in Mg-doped β-Ga_2O_3,[18,20,21,35] the spectra display broad luminescence, with the primary peak reaching maximum intensity within the 300 – 600 nm range. The main PL peak positions are cataloged in **Table 5.2**. Correspondingly, the inset in **Figure 5.4(a)** shows the main PL peak positions as a function of Mg atomic percentage. The main PL peak position of sample #1 is located at ~3.02 eV (~409.99 nm), which is in good agreement with the reported main PL peak position of bulk β-Ga_2O_3 at ~ 3.10 eV (~400 nm)[36–39]. After incorporating Mg, the main PL peak position of the beta phase MgGaO films decreases below 3.0 eV. Similar phenomenon was observed with the main PL peak of Mg-doped β-Ga_2O_3 single crystal at ~2.75 eV (~450 nm) with respect to ~2.95 (~420 nm) of its undoped β-Ga_2O_3.[40] In addition, all main PL peaks manifest a blue shift among MgGaO thin films as Mg composition increases, which is consistent with the escalating optical bandgap observed in β-MgGaO, mixed phase, and spinel phase regions, respectively. RT PL peak deconvolution was conducted to discern the optical transitions within all samples. As illustrated by sample #2 in the beta phase and sample #9 in the spinel phase here.

Table 5.2 Main PL peak position and the spatial distribution of defect levels in undoped β-Ga_2O_3, β-MgGaO, β and spinel mixed phase and spinel MgGaO at room temperature. Specifically, these values are referenced to the energy (in eV) below the conduction band minimum (CBM) for oxygen vacancies associated with donor bands, and above the valence band maximum (VBM) for self-trapped holes (STHs), and $V_{Ga\text{-}O}$ and Mg_{Ga} acceptors. Corresponding experimental and density functional theory (DFT) calculated values of β-Ga_2O_3, and Mg-doped Ga_2O_3 from literature are included for comparison.

MgGaO Sample	**Main PL peak position at RT** (eV)	V_{O_I} (eV)	$V_{O_{II}}$ (eV)	$V_{O_{III}}$ (eV)	E_{STH}^{bind} (eV)	Mg_{Ga} (V_{Ga-O}) (eV)
#1 Mg 0%	3.02	1.32	2.04	1.8	0.49	(0.63)
#2 Mg 2.89%	2.55	1.51	2.09	1.87	0.58	(0.69)
#3 Mg 4.05%	2.79	-	-	-	0.51	-
#4 Mg 6.71%	2.68	-	-	-	0.40	-
#5 Mg 7.42%	2.79	-	-	-	0.42	-
#6 Mg 12.04%	2.90	-	-	-	0.78	-
#7 Mg 13.31%	2.97	0.68	1.17	1.05	0.89	1.69
#8 Mg 14.04%	3.10	1.02	2.05	1.57	0.61	1.21
#9 Mg 15.26%	3.17	1.03	1.97	1.54	0.42	1.13
β-Ga_2O_3[41,42]	2.5 -3.0	1.38	1.76	1.56	0.53	(0.27)
Mg:Ga_2O_3[21,41,43]	1.5 -2.5	1.44	1.77	1.61	-	1.0 - 1.5 (0.35)
DFT[18]	-	1.6	2.0	1.7	-	1.05

Figure 5.4(b) shows the deconvoluted PL peaks for sample #2, encompassing emissions at approximately 3.40 eV for UV_I emission, 430.19 nm 2.88 eV for violet, 2.52 eV for blue, 2.30 eV for green, and 1.80 eV for red. Meanwhile, **Figure 5.4(c)** shows the deconvoluted PL peaks for sample #9, revealing emissions at around 3.93 eV for UV_I, 4.32 eV for UV_{II}, 3.29 eV for violet, 2.78 eV for blue, and 2.35 eV for green. PL deconvolution for all remaining samples is shown in **Figure S5.1** in the supporting information.

The energy level diagram outlining the PL mechanism in both β-MgGaO and spinel $MgGa_2O_4$ films is depicted in **Figure 5.4(d)**. Similar to the energy levels predicted or observed in β-Ga_2O_3, Mg-doped Ga_2O_3 and spinel $MgGa_2O_4$ thin films,[18,21,23] three oxygen-vacancy related donor levels, polaronic self-trapped hole (STH) states, and Mg on Ga site (Mg_{Ga}) acceptor level or Ga and O vacancy defect complex acceptor level ($V_{Ga\text{-}O}$) are included in addition to the conduction and valence bands. The UV_I emission observed in all films is attributed to the optical transition between electrons in the conduction bandand STHs. Its energy E_{UV_I} can be calculated based on the equation: $E_{UV_I} = E_g - E_{polaron}^{STH} - E_{STH}^{bind}$, where E_g is the bandgap, $E_{polaron}^{STH}$ is the polaronic STH energy level of ~1.1 eV above the valence band, which is assumed to be the same as in β-Ga_2O_3,[18] and E_{STH}^{bind} is the binding energy of STHs to oxygen atom.[42] E_{STH}^{bind} for all samples were calculated and summarized in **Table 5.2**. For example, E_{STH}^{bind} of pure β-phase sample #2 and pure spinel sample #9 is estimated to be ~0.58 and 0.42 eV, respectively, which is close to ~0.53 eV of β-Ga_2O_3.[42] The second UV peak (UV_{II}), which is attributed to an optical transition between conduction band and Mg_{Ga} antisite acceptors in MgGaO thin films or $V_{Ga\text{-}O}$ defect complex acceptors in Ga_2O_3 reference sample, can be extracted

[41],[44,45]. The difference is that this peak can be observed at room temperature for pure spinel $MgGa_2O_4$ samples, as shown in **Figure 5.4(c)**, while it can only be revealed at low temperature for Ga_2O_3 and low-Mg composition β-MgGaO thin films, as shown later. The acceptor ionization energies E_A (either $E_{Mg_{Ga}}$ or $E_{V_{Ga-O}}$) of these samples can be calculated as $E_A = E_g - E_{UV_{II}}$ and are listed in **Table 5.2**. As shown in the table, the acceptor ionization energy for β-Ga_2O_3 and β-MgGaO sample 2 is 0.63 and 0.69 eV, respectively. The high similarity of these values suggests that the acceptor responsible for the UV_{II} optical transition in β-MgGaO sample 2 could still be dominated by V_{Ga-O} instead of Mg_{Ga} antisite acceptors even if almost 2.9 at.% Mg is incorporated in the alloy. Nevertheless, these values are larger than reported V_{Ga-O} acceptor ionization energies in β-Ga_2O_3 and Mg-doped Ga_2O_3 samples, which may be due to smaller band gaps of their samples. On the other hand, the acceptor ionization energy is ~1.69, 1.21 and 1.18 eV for pure spinel $MgGa_2O_4$ samples 7-9, respectively. It is noted that the acceptor ionization energy decreases with increasing Mg atomic percent, namely, it shifts towards the valence band maximum (VBM) as the Mg composition increases in these spinel samples. In comparison, the Mg_{Ga} deep acceptor energy level of Mg doped β-Ga_2O_3 was determined experimentally at ~1.79 eV above the valence band edge,[21] while calculated Mg_{Ga} energy levels are appropriately situated in the range of 1-1.5 eV above the VBM.[21] Since the acceptor ionization energies are similar to these reported values, it can be inferred that Mg_{Ga} antisite species are the dominating deep acceptors in $MgGa_2O_4$ spinel samples.

Besides the above UV emissions, violet, blue and green visible emissions were observed for all films, which originate from donor-acceptor pair (DAP) transitions between three oxygen vacancy donor bands and $V_{Ga\text{-}O}$ acceptor bands or Mg_{Ga} antisite acceptor levels, as shown in **Figure 5.4(d)**. Using these visible emission peak energies, with a knowledge of the acceptor energy level, the three oxygen vacancy level positions can be calculated, or

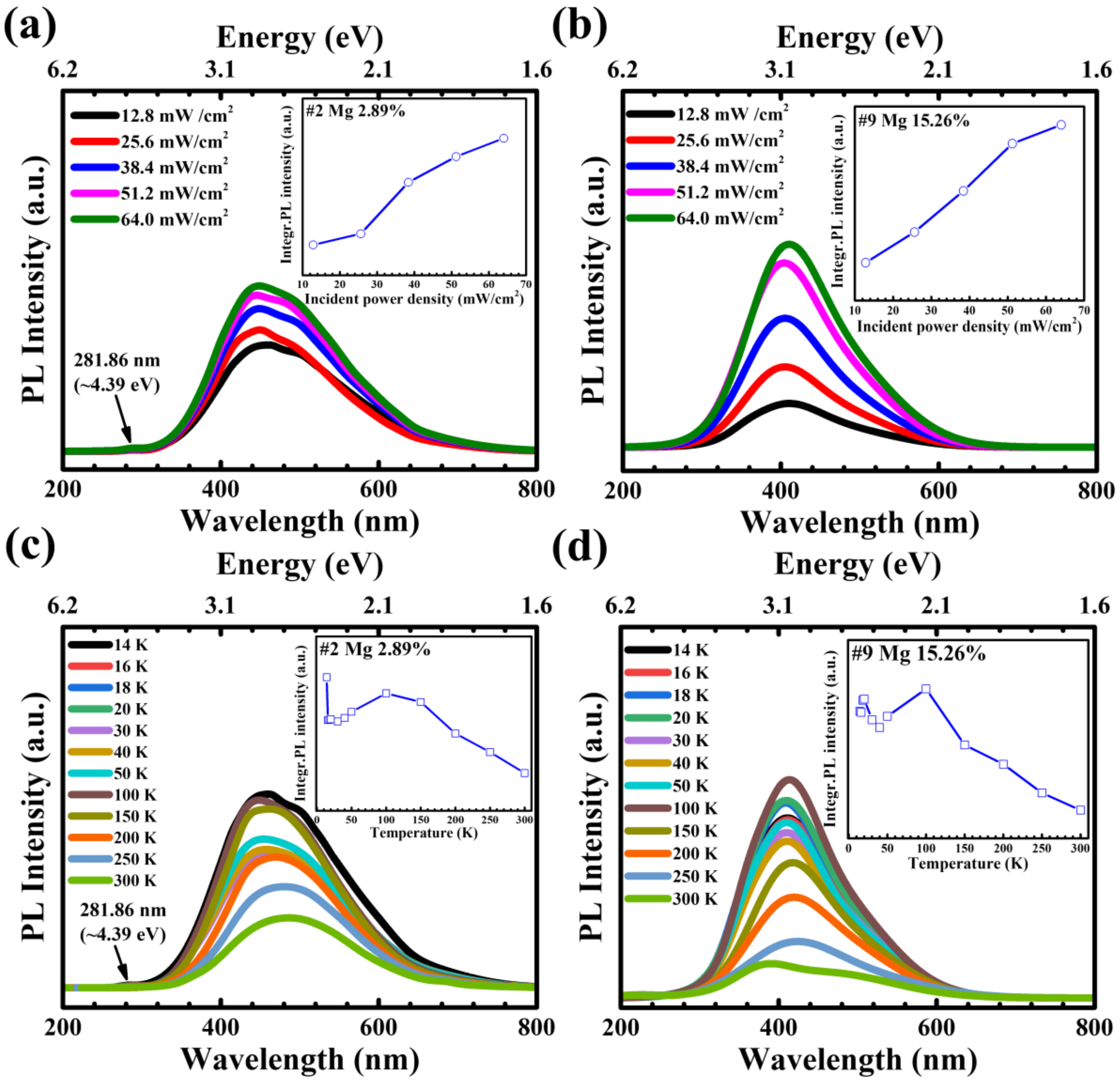

Figure 5.5 (a)-(b) Power dependent PL spectra at 14 K for sample #2 and #9, and insets are the integrated PL intensity versus incident power density, respectively. (c)-(d) Temperature dependent PL spectra at 12.8 mW/cm^2 for sample #2 and #9, insets are the integrated PL intensity versus temperature, respectively.

vice versa. **Table 5.2** lists these values that can be extracted. For example, the three oxygen vacancy levels for Ga_2O_3 sample #1 are estimated at 1.32, 1.8 and 2.04 eV below the conduction band edge, which is in good agreement with DFT calculation results of 1.6, 1.7 and 2.0 eV,[18] respectively. For β-phase MgGaO sample #2, the oxygen vacancy energy levels are estimated at 1.51, 1.87 and 2.09 eV below the conduction band edge, respectively. The estimated energy levels of the three oxygen vacancies of spinel sample #9 are 0.98, 1.49, and 1.92 eV below the conduction band edge, respectively. Since there were no UV_{II} peaks detected in sample #3 and mixed-phased samples, the oxygen vacancy energy levels cannot be calculated. Finally, a very weak red emission located at ~ 680 nm was observed for MgGaO samples #2-#6 in the beta and mixed phases, which is similar to the reported ~690 nm red emission in Mg-doped β-Ga_2O_3.[21] The origin of the red emission remains unclear, although it was suggested to be a transition between valance band and Mg_{Ga} antisite deep acceptor energy levels. [21]

5.3.3 Power and temperature dependent PL

Figure 5.5(a)-(b) show power-dependent PL spectra of β-MgGaO sample #2 and spinel $MgGa_2O_4$ sample #9 at 14 K, with excitation power densities ranging from 12.8 mW/cm² to 64.0 mW/cm², respectively, and the insets are the integrated PL intensity versus power density accordingly. The corresponding results for the remaining samples are provided in **Figures S5.2(a)-(g)** in the supporting information. For each sample, the PL peak position remains stable despite variations in incident power density. In addition, the increase in integrated PL intensity with increasing incident power density is attributed to the increased number of pumped electrons, following a similar nonlinear trend.[46,47] This behavior is indicative of the interplay among Shockley-Read-Hall (SRH) recombination, spontaneous emission, and Auger recombination processes.[47] It should also be noted that a UV peak, which is designated as UV_{II} emission emerges at approximately 4.39 eV at 14 K for both β-Ga_2O_3 sample #1 (**Figure S5.2(a)**) and β-MgGaO sample #2 (**Figure 5.5(a)**). This UV_{II} emission is attributed to the recombination of electrons in the conduction band and holes in the $V_{Ga\text{-}O}$ defect complex acceptor level in Ga_2O_3 and/or Mg_{Ga} antisite acceptor level in MgGaO, as discussed earlier.

Figures 5.5(c)-(d) show temperature-dependent PL spectra of samples #2 and #9, recorded over a temperature range between 14 and 300 K with an incident lasing power density of 12.8 mW/cm², respectively. The inset is the integrated PL intensity versus the temperature accordingly. The corresponding results for the remaining samples are shown in **Figures S5.3(a)-(g)** in the supporting information. Across all samples, the PL exhibits negative thermal quenching (NTQ) effects for the temperature below ~100 K, while positive thermal quenching (PTQ) effects dominate with the temperature above ~100 K. The PTQ is primarily due to the fact that thermal energy promotes non-radiative recombination pathways such as Shockley-Read-Hall (SRH) recombination.[48,49] On the other hand, the existence of NTQ suggests the presence of multiple intermediate energy levels within the bandgap that participate in radiative recombination processes, [48–50] which is the case in our samples.

5.4 Conclusion

In this chapter, we conducted the growth of nine MgGaO thin films via MBE, with varying Mg atomic percentages spanning from 0 to 15.26%. Our primary focus was to elucidate the phase transition phenomena from the β-phase to spinel phase and PL properties of these films. Through systematic investigation, we established distinct phase boundaries: when the Mg atomic percentage ranges from 0 to 4.05%, the material predominantly exhibits pure β phase; within the Mg atomic percentage range of 6.71% to 12.04%, a mixture of β-phase and spinel phase is observed; while at Mg atomic percentages between 13.31% and 15.26%, the material transitions entirely into pure spinel phase. Comprehensive PL studies were carried out, unraveling the PL mechanisms associated with both β-MgGaO and spinel $MgGa_2O_4$ thin films. Our investigation contributes to a deeper understanding of the intricate phase transitions and sheds light on the defect energy levels intrinsic to Ga_2O_3-based MgGaO alloys. This elucidation holds promise for optimizing the performance of UWBG semiconductor electronic and optoelectronic devices through informed design strategies based on a thorough comprehension of crystal structure and defect characteristics.

5.5 References

[1] J. Y. Tsao, S. Chowdhury, M. A. Hollis, D. Jena, N. M. Johnson, K. A. Jones, R. J. Kaplar, S. Rajan, C. G. Van de Walle, E. Bellotti, C. L. Chua, R. Collazo, M. E. Coltrin, J. A. Cooper, K. R. Evans, S. Graham, T. A. Grotjohn, E. R. Heller, M. Higashiwaki, M. S. Islam, P. W. Juodawlkis, M. A. Khan, A. D. Koehler, J. H. Leach, U. K. Mishra, R. J. Nemanich, R. C. N. Pilawa-Podgurski, J. B. Shealy, Z. Sitar, M. J. Tadjer, A. F. Witulski, M. Wraback, J. A. Simmons, *Advanced Electronic Materials* **2018**, *4*, 1600501.

[2] C. Xie, X.-T. Lu, X.-W. Tong, Z.-X. Zhang, F.-X. Liang, L. Liang, L.-B. Luo, Y.-C. Wu, *Advanced Functional Materials* **2019**, *29*, 1806006.

[3] M. Kim, J.-H. Seo, U. Singisetti, Z. Ma, *Journal of Materials Chemistry C* **2017**, *5*, 8338.

[4] S. J. Pearton, J. Yang, P. H. Cary, F. Ren, J. Kim, M. J. Tadjer, M. A. Mastro, *Applied Physics Reviews* **2018**, *5*, 011301.
[5] S. Sharma, K. Zeng, S. Saha, U. Singisetti, *IEEE Electron Device Letters* **2020**, *41*, 836.

[6] K. Zeng, A. Vaidya, U. Singisetti, *IEEE Electron Device Letters* **2018**, *39*, 1385.
[7] S. Oh, C.-K. Kim, J. Kim, *ACS Photonics* **2018**, *5*, 1123.

[8] X. Chen, F. Ren, S. Gu, J. Ye, *Photon. Res., PRJ* **2019**, *7*, 381.

[9] C. Xu, Z. Du, Y. Huang, M. Dong, R. Lin, Y. Li, B. Wang, W. Zheng, F. Huang, *ACS Appl. Mater. Interfaces* **2018**, *10*, 42681.

[10] M. Dong, W. Zheng, C. Xu, R. Lin, D. Zhang, Z. Zhang, F. Huang, *Advanced Optical Materials* **2019**, *7*, 1801272.

[11] C. Shou, T. Yang, A. Almujtabi, T. Yang, Y. Li, Q. S. Mahmud, M. Xu, J.-G. Zheng, J. Liu, *Applied Physics Letters* **2023**, *122*, 212101.

[12] T. Yang, C. Shou, A. Almujtabi, J. Tran, Q. Lin, Y. Li, Q. S. Mahmud, P. Wei, J. Liu, *ACS Appl. Opt. Mater.* **2023**, *1*, 1670.

[13] T. Yang, C. Shou, L. Xu, J. Tran, Y. He, Y. Li, P. Wei, J. Liu, *ACS Appl. Electron. Mater.* **2023**, *5*, 2122.

[14] Q. Hou, K. Liu, D. Han, Y. Zhu, X. Chen, B. Li, L. Liu, D. Shen, *Applied Physics Letters* **2022**, *120*, 011101.

[15] Q. Guo, J. Tetsuka, Z. Chen, M. Arita, K. Saito, T. Tanaka, *Optical Materials* **2023**, *143*, 114267.

[16] Q. Hou, K. Liu, X. Chen, J. Yang, Q. Ai, Z. Cheng, Y. Zhu, B. Li, L. Liu, D. Shen, *physica status solidi (RRL) – Rapid Research Letters* **2022**, *16*, 2200137.

[17] T. Onuma, S. Fujioka, T. Yamaguchi, M. Higashiwaki, K. Sasaki, T. Masui, T. Honda, *Applied Physics Letters* **2013**, *103*, 041910.

[18] Y. Wang, P. T. Dickens, J. B. Varley, X. Ni, E. Lotubai, S. Sprawls, F. Liu, V. Lordi, S. Krishnamoorthy, S. Blair, K. G. Lynn, M. Scarpulla, B. Sensale-Rodriguez, *Sci Rep* **2018**, *8*, 18075.

[19] M. M. Islam, D. Rana, A. Hernandez, M. Haseman, F. A. Selim, *Journal of Applied Physics* **2019**, *125*, 055701.

[20] K. Zhang, Z. Xu, S. Zhang, H. Wang, H. Cheng, J. Hao, J. Wu, F. Fang, *Physica B: Condensed Matter* **2021**, *600*, 412624.

[21] K. Zhang, Z. Xu, J. Zhao, H. Wang, J. Hao, S. Zhang, H. Cheng, B. Dong, *Journal of Alloys and Compounds* **2021**, *881*, 160665.

[22] Z. Liu, P. Hu, X. Jing, L. Wang, *J. Electrochem. Soc.* **2008**, *156*, H43.

[23] D. V. Mlotswa, L. L. Noto, S. J. Mofokeng, K. O. Obodo, V. R. Orante-Barrón, B. M. Mothudi, *Optical Materials* **2020**, *109*, 110134.

[24] *Vacuum* **2016**, *123*, 8.

[25] S. Ghose, S. Rahman, L. Hong, J. S. Rojas-Ramirez, H. Jin, K. Park, R. Klie, R. Droopad, *Journal of Applied Physics* **2017**, *122*, 095302.

[26] K. Ema, K. Sasaki, A. Kuramata, H. Murakami, *Journal of Crystal Growth* **2021**, *564*, 126129.

[27] A. Luchechko, O. Kravets, *physica status solidi c* **2017**, *14*, 1600146.

[28] T. Suzuki, M. Hughes, Y. Ohishi, *Journal of Luminescence* **2010**, *130*, 121.

[29] X. Bi, Z. Wu, Y. Huang, W. Tang, *AIP Advances* **2018**, *8*, 025008.

[30] J. Wei, K. Kim, F. Liu, P. Wang, X. Zheng, Z. Chen, D. Wang, A. Imran, X. Rong, X. Yang, F. Xu, J. Yang, B. Shen, X. Wang, *J. Semicond.* **2019**, *40*, 012802.

[31] Q. C. Bui, L. Largeau, M. Morassi, N. Jegenyes, O. Mauguin, L. Travers, X. Lafosse, C. Dupuis, J.-C. Harmand, M. Tchernycheva, N. Gogneau, *Applied Sciences* **2019**, *9*, 3528.

[32] T. Oshima, T. Okuno, S. Fujita, *Jpn. J. Appl. Phys.* **2007**, *46*, 7217.

[33] Z. Chen, K. Ge, D. Meng, X. Chen, *Materials Letters* **2022**, *320*, 132385.

[34] Y. Tang, M. Deng, Z. Zhou, X. Xu, J. Wang, Q. Liu, *Ceramics International* **2022**, *48*, 19141.

[35] Y. K. Frodason, K. M. Johansen, L. Vines, J. B. Varley, *Journal of Applied Physics* **2020**, *127*, 075701.

[36] J. Cooke, P. Ranga, J. Jesenovec, J. S. McCloy, S. Krishnamoorthy, M. A. Scarpulla, B. Sensale-Rodriguez, *Sci Rep* **2022**, *12*, 3243.

[37] L. Ghadbeigi, J. Cooke, G. T. Dang, T. Kawaharamura, T. Yasuoka, R. Sun, P. Ranga, S. Krishnamoorthy, M. A. Scarpulla, B. Sensale-Rodriguez, *J. Electron. Mater.* **2021**, *50*, 2990.

[38] X. Wang, H. Qiao, T. Liu, F. Song, Z. An, Y. Xu, L. Zhang, F. Shi, *J Mater Sci: Mater Electron* **2022**, *33*, 13040.

[39] R. Jangir, S. Porwal, P. Tiwari, S. K. Rai, P. Mondal, T. Ganguli, S. M. Oak, S. K. Deb, *AIP Conference Proceedings* **2013**, *1512*, 212.

[40] V. Vasyltsiv, L. Kostyk, O. Tsvetkova, R. Lys, M. Kushlyk, B. Pavlyk, A. Luchechko, *Acta Physica Polonica: A* **2022**, *141*.

[41] X. Zhu, Y.-W. Zhang, S.-N. Zhang, X.-Q. Huo, X.-H. Zhang, Z.-Q. Li, *Journal of Luminescence* **2022**, *246*, 118801.

[42] J. B. Varley, A. Janotti, C. Franchini, C. G. Van de Walle, *Phys. Rev. B* **2012**, *85*, 081109.

[43] Q. D. Ho, T. Frauenheim, P. Deák, *Phys. Rev. B* **2018**, *97*, 115163.

[44] T. Gake, Y. Kumagai, F. Oba, *Phys. Rev. Mater.* **2019**, *3*, 044603.

[45] J. L. Lyons, A. Janotti, C. G. Van de Walle, *Journal of Applied Physics* **2014**, *115*, 012014.

[46] J. B. Cui, M. A. Thomas, *Journal of Applied Physics* **2009**, *106*, 033518.

[47] A. Sabbar, S. Madhusoodhanan, S. Al-Kabi, B. Dong, J. Wang, S. Atcitty, R. Kaplar, D. Ding, A. Mantooth, S.-Q. Yu, Z. Chen, *Sci Rep* **2019**, *9*, 16758.

[48] V. A. Fonoberov, K. A. Alim, A. A. Balandin, F. Xiu, J. Liu, *Phys. Rev. B* **2006**, *73*, 165317.

[49] H. Shibata, *Jpn. J. Appl. Phys.* **1998**, *37*, 550.

[50] Y. Wu, J. Li, H. Ding, Z. Gao, Y. Wu, N. Pan, X. Wang, *Physical Chemistry Chemical Physics* **2015**, *17*, 5360.

Supporting Information

1. XRD peak position, d spacing and lattice constant parameters

Table S5.1 XRD peak position, d-spacing, and lattice constant of MgGaO thin films in beta, mixed and spinel phase.

Sample	**hkl**	**Position 2θ (°)**	**d-spacing (Å)**	**Lattice constant (Å)**
#1 Mg 0%	$(\bar{4}02)$	38.47	2.338	$\mathbf{a}_{\beta}$ =12.19; $\mathbf{b}_{\beta}$ =3.06; $\mathbf{c}_{\beta}$ =5.79
#2 Mg 2.89%	$(\bar{4}02)$	38.15	2.356	$\mathbf{a}_{\beta}$ =12.28; $\mathbf{b}_{\beta}$ =2.93; $\mathbf{c}_{\beta}$ =5.84
#3 Mg 4.05%	$(\bar{4}02)$	38.15	2.356	$\mathbf{a}_{\beta}$ =12.28; $\mathbf{b}_{\beta}$ =2.93; $\mathbf{c}_{\beta}$ =5.84
#4 Mg 6.71%	$(\bar{4}02)$	38.11	2.359	$\mathbf{a}_{\beta}$ =12.30; $\mathbf{b}_{\beta}$ =N/A; $\mathbf{c}_{\beta}$ =5.84
#5 Mg 7.42%	$(\bar{4}02)$	38.08	2.361	$\mathbf{a}_{\beta}$ =12.31; $\mathbf{b}_{\beta}$ =N/A; $\mathbf{c}_{\beta}$ =5.85
#6 Mg 12.04%	$(\bar{4}02)$	37.80	2.377	$\mathbf{a}_{\beta}$ =12.40; $\mathbf{b}_{\beta}$ =N/A; $\mathbf{c}_{\beta}$ =5.89
#7 Mg 13.31%	(222)	37.67	2.385	a_{spinel}=8.26
#8 Mg 14.04%	(222)	37.67	2.385	a_{spinel}=8.26
#9 Mg 15.26%	(222)	37.66	2.386	a_{spinel}=8.27

2. Room temperature PL deconvolution

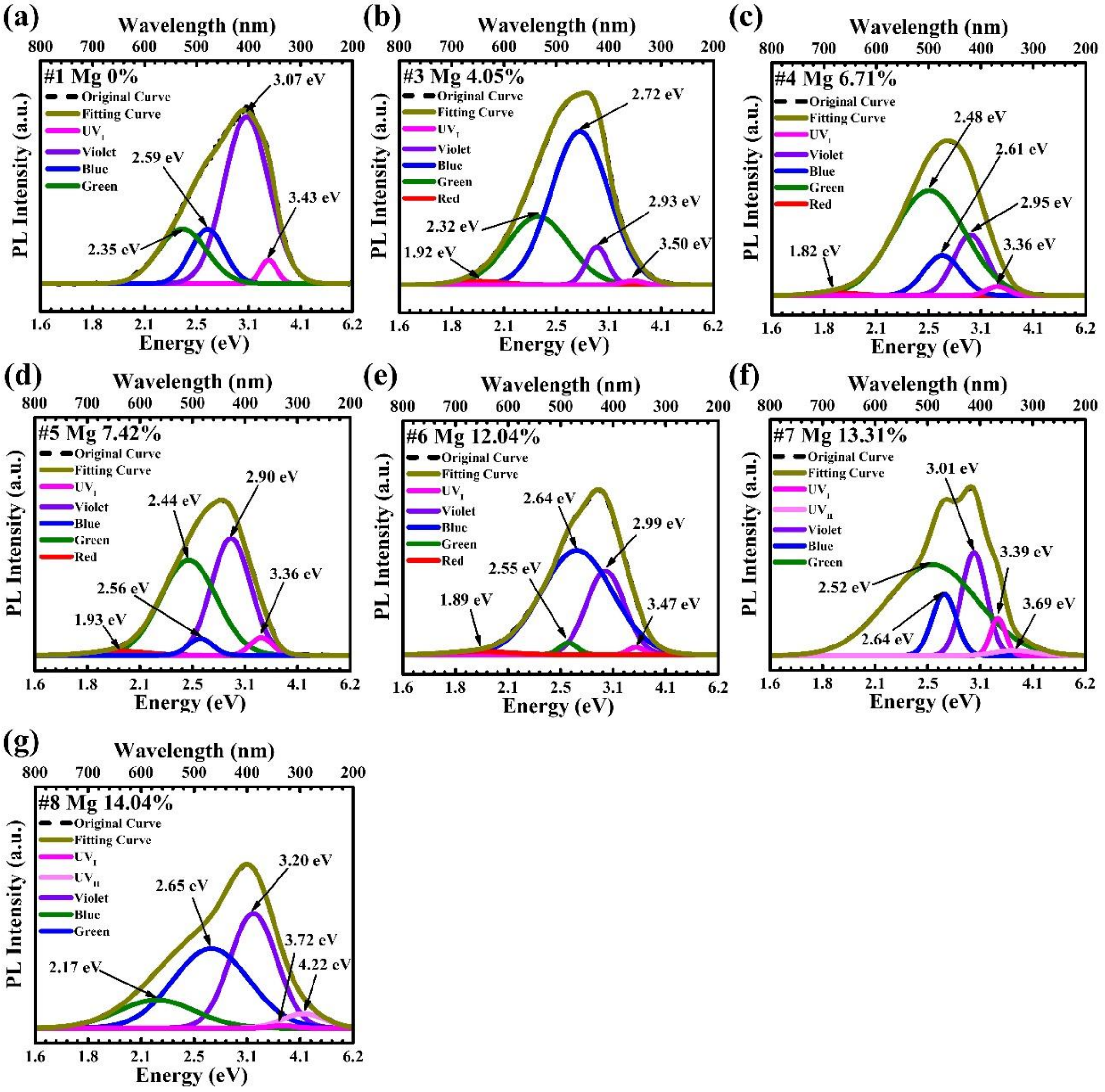

Figure S5.1 Room temperature PL deconvolution for (a) sample #1 and (b) sample #3 in beta phase, (c)-(e) sample #4-#6 in mixed phase, and (e) sample #7 and (f) sample #8 in spinel phase.

3. Power dependent PL and integrated PL intensity versus incident power density

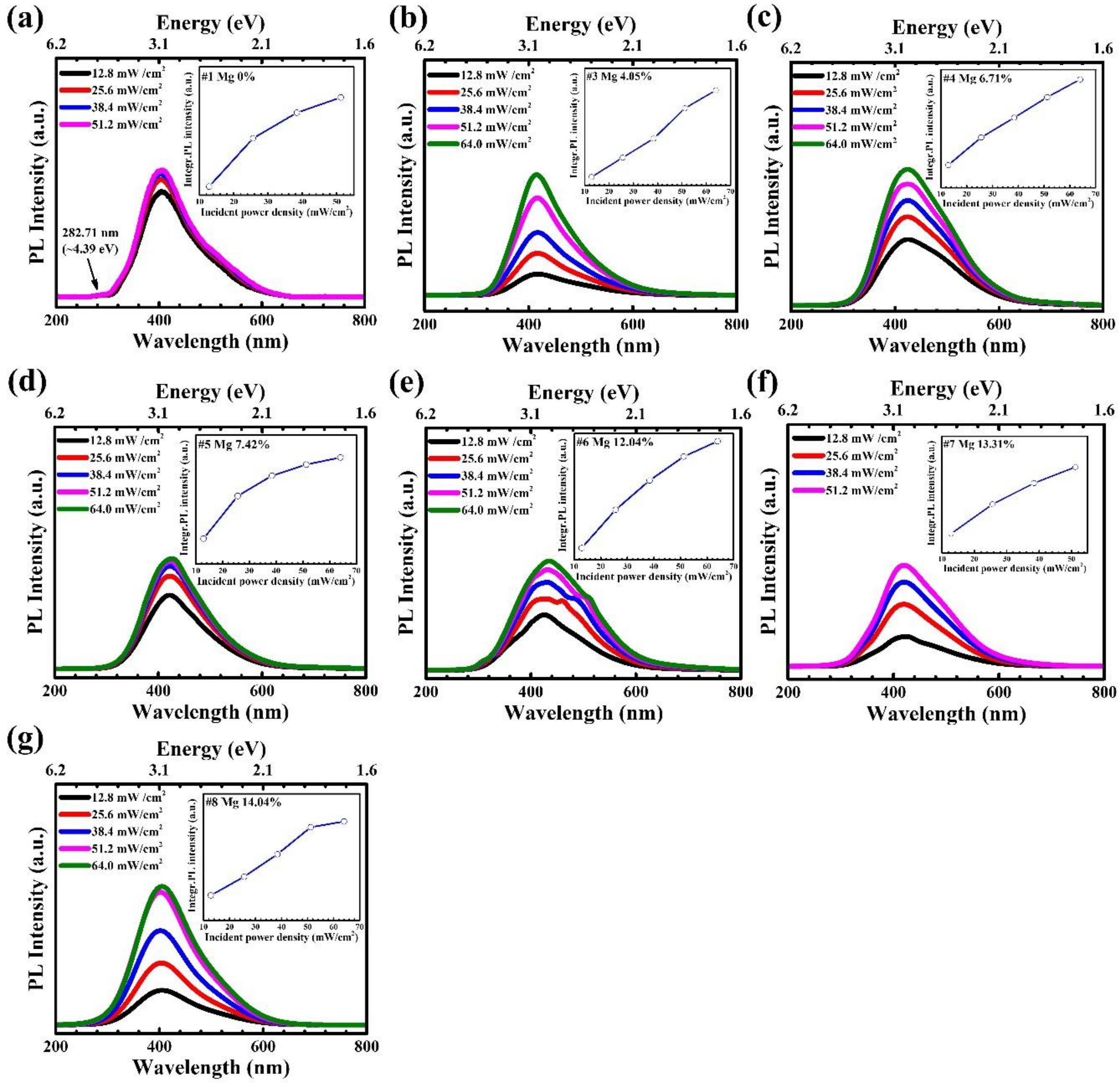

Figure S5.2 Power dependent PL spectra of (a) sample #1 and (b) sample #3 in beta phase, (c)-(e) sample #4-#6 in mixed phase, and (e) sample #7 and (f) sample #8 in spinel phase. Inset is the integrated PL intensity versus incident power density, respectively.

4. Temperature dependent PL and integrated PL intensity

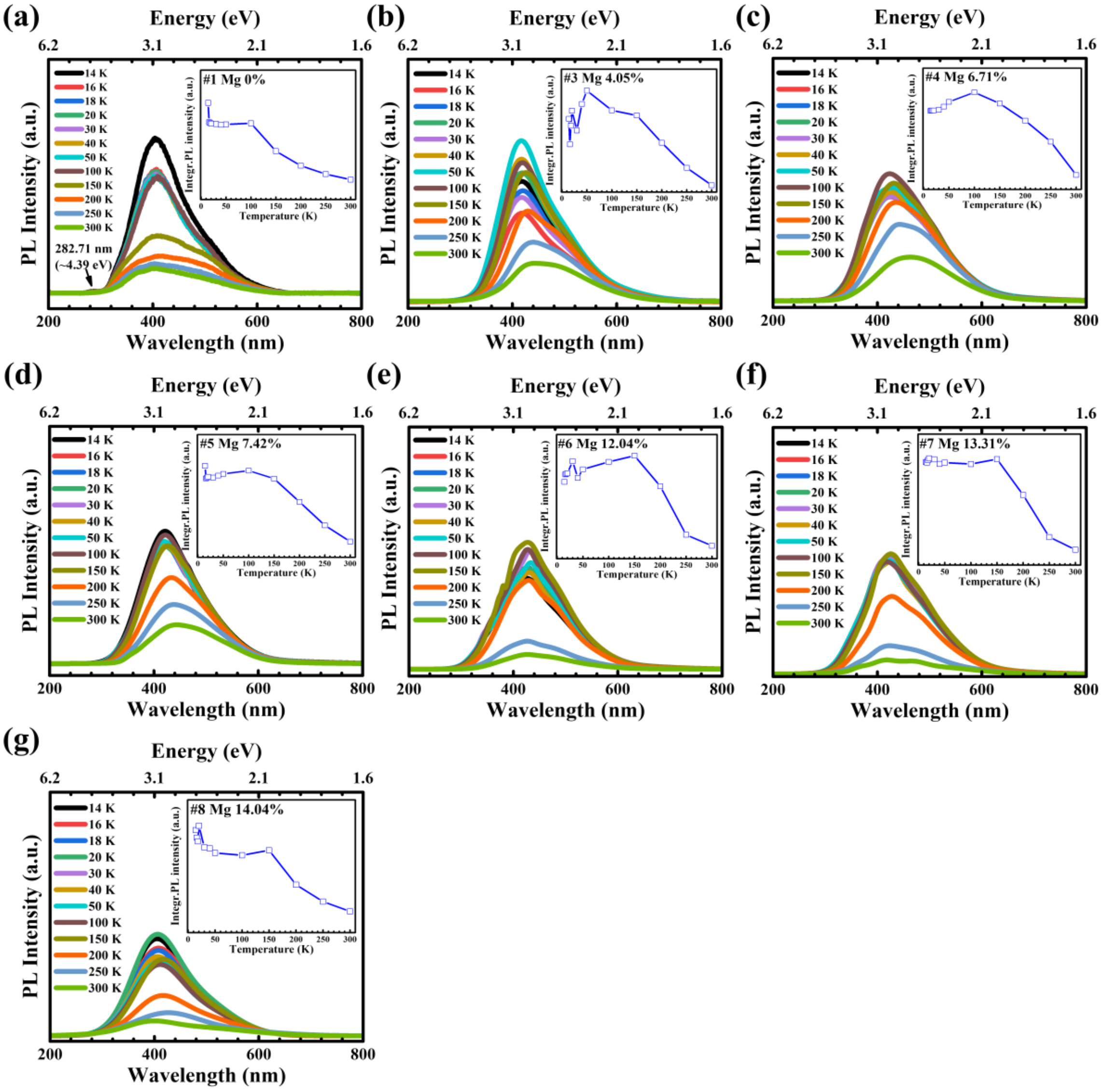

Figure S5.3 Temperature dependent PL spectra of (a) sample #1 and (b) sample #3 in beta phase, (c)-(e) sample #4-#6 in mixed phase, and (e) sample #7 and (f) sample #8 in spinel phase. Inset is the integrated PL intensity versus temperature, respectively.

Chapter 6: Summary

This dissertation systematically investigates MgGaO thin films, focusing on their growth via molecular beam epitaxy (MBE), phase transitions, film characterization, and photoluminescence (PL) properties.

Chapter 2 explores the MBE growth conditions of β-MgGaO single crystalline thin films, aiming to engineer their bandgaps (5.03 to 5.22 eV) by adjusting Mg^{2+} atomic percentages. Metal-semiconductor-metal (MSM) photodetectors were fabricated from these films, highlighting their potential for deep-UV photodetection.

Chapter 3 extends this study by synthesizing MgGaO thin film samples with varying Mg/Ga atomic ratios (0 at.%/100 at.% to 100 at.%/0 at.%) using MBE. It investigates phase transformations, film quality, lattice parameters, surface morphology, optical bandgaps, and epitaxial relationships with c-sapphire substrates.

Chapter 4 focuses on the epitaxial growth of spinel $MgGa_2O_4$ films using MBE, examining structural, optical, and surface morphology properties. Detailed PL studies explore the mechanisms associated with native defects in $MgGa_2O_4$.

Chapter 5 continues with the growth of MgGaO thin films, specifically examining nine samples with Mg atomic percentages ranging up to 15.26% to refine the phase transition from beta phase to spinel phase. It investigates structural transformations, film quality, lattice parameters, optical bandgap, transmittance properties, and PL characteristics for MgGaO thin films.

Appendix: Publications

1. Yang, Tianchen, Chengyun Shou, Long Xu, Jason Tran, Yanwei He, Yuan Li, Peng Wei, and Jianlin Liu. "Metal–Semiconductor–Metal Photodetectors Based on β-MgGaO Thin Films." ACS Applied Electronic Materials 5, no. 4 (2023): 2122-2130. https://doi.org/10.1021/acsaelm.3c00035.

2. Yang, Tianchen, Chengyun Shou, Abdullah Almujtabi, Jason Tran, Qiyin Lin, Yuan Li, Quazi Sanjid Mahmud, Peng Wei, and Jianlin Liu. "Investigation of Phase Transition and Ultrawide Band Gap Engineering in MgGaO Semiconductor Thin Films." ACS Applied Optical Materials 1, no. 10 (2023): 1670-1678. https://doi.org/10.1021/acsaom.3c00237.

3. Yang, Tianchen, Chengyun Shou, Jason Tran, Abdullah Almujtabi, Quazi Sanjid Mahmud, Edward Zhu, Yuan Li, Peng Wei, and Jianlin Liu. "Photoluminescence study of $MgGa_2O_4$ spinel oxide films grown by molecular beam epitaxy." *Applied Physics Letters* 125, no. 7 (2024). https://doi.org/10.1063/5.0218242.

4. Yang, Tianchen, Chengyun Shou, Abdullah Almujtabi, Quazi Sanjid Mahmud, Edward Zhu, Yuan Li, and Jianlin Liu. " Beta to spinel phase transition of magnesium gallium oxide thin films and their photoluminescence properties." ACS Applied Electronic Materials (2024). https://doi.org/10.1021/acsaelm.4c01079.

5. Shou, Chengyun, Tianchen Yang, Theodore Yang, Abdullah Almujtabi, Yuan Li, Quazi Sanjid Mahmud, and Jianlin Liu. "Phase Transition and Bandgap Engineering of MgSnO Thin Films for Solar-Blind Ultraviolet Photodetector Applications." ACS Applied Electronic Materials 6, no. 3 (2024): 1912-1920. https://doi.org/10.1021/acsaelm.3c01804.

6. Shou, Chengyun, Tianchen Yang, Abdullah Almujtabi, Theodore Yang, Yuan Li, Quazi Sanjid Mahmud, Mingjie Xu, Jian-Guo Zheng, and Jianlin Liu. "Improving crystal quality of β-phase MgGaO thin films by using low-temperature homo-buffer layer." Applied Physics Letters 122, no. 21 (2023). https://doi.org/10.1063/5.0147948.

7. Li, Yuan, Zhenjun Cui, Yanwei He, Hao Tian, Tianchen Yang, Chengyun Shou, and Jianlin Liu. "Resistive switching properties of monolayer h-BN atomristors with different electrodes." Applied Physics Letters 120, no. 17 (2022). https://doi.org/10.1063/5.0087717.

8. Li, Yuan, Hector Gomez, Jason Tran, Yanwei He, Chengyun Shou, Tianchen Yang, Peng Wei, Roger K. Lake, and Jianlin Liu. "The role of oxygen incorporation in Ni (111) substrates on the growth of hexagonal boron nitride

monolayers." Nanotechnology 34, no. 50 (2023): 505602. https://doi.org/10.1088/1361-6528/acfaa8.

9. He, Y., Li, Y., Isarraraz, M., Pena, P., Tran, J., Xu, L., Tian, H., Yang, T., Wei, P., Ozkan, C.S. and Ozkan, M., 2021. Robust nanocapacitors based on wafer-scale single-crystal hexagonal boron nitride monolayer films. ACS Applied Nano Materials, 4(6), pp.5685-5695. https://doi.org/10.1021/acsanm.1c00298.

10. He, Y., Tian, H., Das, P., Cui, Z., Pena, P., Chiang, I., Shi, W., Xu, L., Li, Y., Yang, T. and Isarraraz, M., 2020. Growth of high-quality hexagonal boron nitride single-layer films on carburized Ni substrates for metal–insulator–metal tunneling devices. ACS applied materials & interfaces, 12(31), pp.35318-35327. https://doi.org/10.1021/acsami.0c07201.